Quantification and Management of Uncertainties in Radiation Therapy

Jan Hofmaier

München 2022

Aus der
Klinik und Poliklinik für Strahlentherapie und Radioonkologie
der
Ludwig–Maximilians–Universität München
Direktor: Prof. Dr. med. Claus Belka

Quantification and Management of Uncertainties in Radiation Therapy

Dissertation
zum Erwerb des Doktorgrades der Naturwissenschaften
an der Medizinischen Fakultät
der Ludwig–Maximilians–Universität
München

vorgelegt von
Jan Hofmaier
aus Herrenberg

München 2022

Gedruckt mit Genehmigung der Medizinischen Fakultät
der Ludwig–Maximilians–Universität München

Erstgutachter: **Prof. Dr. rer. nat. Katia Parodi**
Zweitgutachter: **Prof. Dr. rer. nat. Olaf Dietrich**
Dekan: **Prof. Dr. med. Thomas Gudermann**
Tag der mündlichen Prüfung: **30. Januar 2023**

Affidavit

Eidesstattliche Versicherung

Ich, Jan Hofmaier, erkläre hiermit an Eides statt, dass ich die vorliegende Dissertation mit dem Thema

Quantification and Management of Uncertainties in Radiation Therapy

selbstständig verfasst, mich außer der angegebenen keiner weiteren Hilfsmittlel bedient und alle Erkenntnisse, die aus dem Schrifttum ganz oder annähernd übernommen sind, als solche kenntlich gemacht und nach ihrer Herkunft unter Bezeichnung der Fundstelle einzeln nachgewiesen habe.

Ich erkläre des Weiteren, dass die hier vorgelegte Dissertation nicht in gleicher oder in ähnlicher Form bei einer anderen Stelle zur Erlangung eines akademischen Grades eingereicht wurde.

München, 16.02.2022	Jan Hofmaier
Ort, Datum	Unterschrift Doktorand

Table of contents

Acknowledgments

First, I would like to thank my thesis advisor Prof. Dr. Katia Parodi for taking the time to advise me and giving me the opportunity to write this thesis under her supervision. I am also extremely grateful to Dr. Florian Kamp who spent countless hours advising me and proofreading my work for his never ending support and encouragement. This thesis could not have been done without him. Furthermore, I would like to thank the head of Medical Physics at LMU Munich, Dr. Michael Reiner, the vice chair of the Department of Radiation Oncology, Prof. Dr. Maximilian Niyazi and the chair of the Department of Radiation Oncology, Prof. Dr. Claus Belka, for their support of my work. Moreover, I would like to thank Prof. Dr. Guillaume Landry and Dr. Christopher Kurz for their helpful advice and fruitful discussions. In addition, I thank Dr. Matthias Söhn and Prof. Dr. Markus Alber for help with the research TPS Hyperion. I also would like to express my gratitude to all my current and former colleagues at the LMU Munich who contributed to this thesis one way or the other, in particular Dr. Cornelius Maihöfer, Dr. Lars Schüttrumpf, Dr. Raphael Bodensohn, Dr. Sylvia Garny, Dr. Indrawati Hadi, Dr. Daniel Fleischmann, Michael Eder, Yavuz Dinc, Dr. Stefanie Corradini, Dr. Franziska Walter, Dr. Maya Rottler, Dr. Rieke von Bestenbostel Dr. Philipp Freislederer and Larissa Ermoschkin. And I also would like to thank Dr. George Dedes of the Department of Medical Physics at LMU Munich for providing Monte Carlo simulated data which has been used in this project. In addition, I would like to thank our collaboration partners at the Fraunhofer Institute for Industrial Mathematics: Dr. Jonas Haehnle, Dr. Philipp Süss, Dr. Katrin Teichert and Prof. Dr. Karl-Heinz Küfer; and at the Fraunhofer Institute for Medical Image Computing: Nadine Spahr, Christoph Brachmann and Dr. Florian Weiler; and Prof. David J. Carlson at the Yale School of Medicine. I am also grateful to the German Research Foundation (DFG) who supported parts of this work in the context of the DFG grant KA 4346/1-1 and the DFG Cluster of Excellence Munich Center for Advanced Photonics (MAP). On a more personal note, I would like to thank my family for their continuous support and encouragement. Last but not least, I want to thank Patricia, for being in my life, for motivating me in times of doubt and for her patience.

Summary

For the therapeutic success of radiotherapy treatment it is crucial that the actual dose distribution delivered to a patient coincides as precisely as possible with the planned distribution, since deviations might lead to unexpected treatment toxicities or tumor recurrences. In this cumulative dissertation, an approach for patient positioning to manage the impact of anatomical changes in photon therapy is evaluated, and a framework for quantitative analyses of various types of uncertainty in proton therapy is developed. In the first project, an existing algorithm for scatter correction of cone beam computed tomography (CBCT) images is used to enable a dose recalculation on the changed patient anatomy. This is combined with a software tool for multi-criterial optimization of the patient position based on dosimetric parameters. The feasibility of the approach is shown for two clinical datasets of head and neck cancer patients, and potential benefits in comparison with the clinical standard - a rigid registration of the CBCT to the planning images - are evaluated. It is concluded that the approach offers increased control over target coverage and organ-at-risk (OAR) doses, since in many cases target coverage or OAR dose could be improved compared to the rigid image registration approach. However, for pronounced anatomical changes, both approaches were unable to restore an acceptable target coverage. In the second project of this thesis, a framework for variance-based sensitivity analysis of uncertainties in proton therapy was developed. With a fast, GPU-based pencil beam algorithm, a large number of error scenarios for a proton therapy treatment plan can be calculated. In these scenarios, patient position, proton range and relative biological effectiveness (RBE) model parameters are varied simultaneously and independently within their assumed uncertainty distributions. With this Monte Carlo approach, also interactions between multiple types of uncertainty are taken into account. For the dose distribution and dosimetric parameters such as dose volume histogram (DVH) quantiles for target structures and OARs the overall uncertainty as well as sensitivity indices are calculated. These indices allow for a ranking of the individual input uncertainties with respect to their impact on the overall uncertainty. The feasibility and the capabilities of the framework are shown with two clinical patient datasets. In a further step, the framework is extended to include inter observer variability (IOV) in target definition. In a study with ten patients and 10 observers, the impact of IOV in comparison with setup and range uncertainty on clinical target volume (CTV) coverage is evaluated. For two out of ten patients, a relevant impact of IOV was found. In future studies, this framework might help to determine which types of uncertainty are driving the overall uncertainty of clinically relevant dosimetric parameters

and might help to prioritize research attempts aiming at the reduction of uncertainty.

Zusammenfassung

Für den Therapieerfolg in der Strahlentherapie ist es von essentieller Bedeutung, dass die applizierte Dosisverteilung möglichst genau mit der geplanten übereinstimmt, da Abweichungen zu unerwarteten Nebenwirkungen oder Rezidiven führen können. Die vorliegende kumulative Arbeit befasst sich mit einem Konzept zur Positionierungkorrektur in der Photonentherapie zur Minimierung des dosimetrischen Einflusses von anatomischen Veränderungen in der Photonentherapie und mit der quantitativen Analyse des Zusammenspiels verschiedener Quellen von dosimetrischer Unsicherheit in der Protonentherapie. In ersterem Projekt wird ein bestehender Algorithmus zur Streuungskorrektur von CBCT-Bildern dazu verwendet, eine Dosisneuberechnung auf der aktuellen Patientenanatomie durchzuführen. Dies wird kombiniert mit einem Softwaretool zur multikriteriellen Optimierung der Patientenposition basierend auf dosimetrischen Parametern. Die Machbarkeit des Ansatzes wird für Patienten mit Kopf-Hals-Tumoren gezeigt, und potentielle Vorteile gegenüber dem klinischen Standard für die Positionskorrektur - einer rigiden Registrierung des CBCT auf die Planungsbildgebung - werden anhand von klinischen Bilddaten untersucht. Es wurde gezeigt, dass der Ansatz machbar ist und verbesserte Kontrolle über Dosis im Zielvolumen und Risikoorganen bietet. Meist konnte Zielvolumenabdeckung oder Dosis in Risikoorganen gegenüber der rigiden Bilderegistrierung verbessert werden, jedoch konnte für beide Methoden im Falle zu ausgeprägter anatomischer Veränderungen keine ausreichende Zielvolumenabdeckung mehr hergestellt werden. Im zweiten Teil der Arbeit wurde ein Framework zur Anwendung der statistischen Methode der varianzbasierten Sensitivitätsanalyse auf dosimetrische Unsicherheiten in der Protonentherapie entwickelt. Dieses ermöglicht mit Hilfe eines GPU-basierten Pencil-Beam-Algorithmus die schnelle Berechnung einer großen Zahl an Fehlerszenarien für einen bestehenden Bestrahlungsplan. Während der Berechnung werden Patientenposition, Protonenreichweite und Parameter der Modelle zur Berechnung der relativen biologischen Wirksamkeit der Strahlung gleichzeitig und unabhängig voneinander innerhalb der für sie angenommenen Unsicherheiten variiert. In diesem Monte-Carlo-Ansatz können durch die gleichzeitige Variation aller Parameter auch Wechselwirkungen zwischen verschiedenen Quellen von Unsicherheit berücksichtigt werden. Für die Dosisverteilung und relevante dosimetrische Parameter (DVH-Quantile für Zielvolumina und Risikoorgane) können sowohl die Gesamtunsicherheit als auch Sensitivitätsindizes bestimmt werden. Diese Indizes ermöglichen eine Quantifizierung des Einflusses der einzelnen Eingangsunsicherheiten auf die Gesamtunsicherheit. Die Machbarkeit und die Möglichkeiten des Frameworks werden anhand von zwei klinischen Datensätzen gezeigt. Schließlich wird das Framework

erweitert, um zusätzlich noch Inter-Observer-Variabilität in der Definition der Zielvolumina berücksichtigen zu können. In einer Studie mit zehn Patienten und vier Observern wird der Einfluss der Inter-Observer-Variabilität im Vergleich mit Reichweiten- und Setupunsicherheit auf die Abdeckung des klinischen Zielvolumens untersucht. Für zwei von zehn Patienten ergab sich hierbei ein relevanter Einfluss der Inter-Observer-Variabilität. Zukünftige Studien mit dem Framework könnten Aufschluss darüber geben, für welche Parameter eine Reduktion der Unsicherheit den größten Einfluss auf die Gesamtunsicherheit klinisch relevanter Parameter hat und dadurch helfen, entsprechende Forschungsvorhaben zu priorisieren.

Own Contributions

1. **Paper 1: Multi-criterial patient positioning based on dose recalculation on scatter-corrected CBCT images** The first author (=author of this thesis) implemented a scripted calculation of sample isocenter positions based on a command-line version of the Monte Carlo dose engine used in the research TPS hyperion, contributed to the implementation and evaluation of the scatter correction pipeline, performed the data analysis, literature review and drafted the manuscript.

2. **Paper 2: Variance-based sensitivity analysis for uncertainties in proton therapy: A framework to assess the effect of simultaneous uncertainties in range, positioning, and RBE model predictions on RBE-weighted dose distributions** The first author (=author of this thesis) developed the GPU-based pencil beam dose calculation and implemented the sensitivity analysis framework, performed the data analysis, literature review and drafted the manuscript.

List of Figures

List of Abbrevations

3D-CRT three-dimensional conformal radiotherapy

ART adaptive radiotherapy

CBCT cone beam computed tomography

CPE charged particle equilibrium

CT computed tomography

CTV clinical target volume

DCAT dynamic conformal arc therapy

DNA deoxyribonucleic acid

DSB double strand break

DVH dose volume histogram

EBT external beam therapy

FLUKA fluktuierende Kaskade

Geant4 Geometry and Tracking 4

GPU graphics processing unit

GTV gross tumor volume

IGRT image guided radiotherapy

IMPT intensity modulated proton therapy

IMRT intensity modulated radiotherapy

IOV inter observer variability

KERMA kinetic energy released per unit mass

keV kiloelectronvolt

LEM local effect model

LET linear energy transfer

LINAC linear accelerator

MC Monte Carlo

MCDS Monte Carlo damage simulation

MeV megaelectronvolt

MKM microdosimetric-kinetic model

MLC multi leaf collimator

MRI magnetic resonance imaging

OAR organ-at-risk

PET positron emission tomography

PSPT passively scattered proton therapy

PTV planning target volume

RBE relative biological effectiveness

RF radio frequency

RMF repair-misrepair-fixation

RMW rotating modulation wheel

SA sensitivity analysis

SFUD single field uniform dose

SOBP spread-out Bragg peak

SSPT spot scanning proton therapy

TCPE transient charged particle equilibrium

TERMA total energy released per unit mass

UA uncertainty analysis

VMAT volumetric modulated arc therapy

XVMC X-ray voxel Monte Carlo

Chapter 1

Introduction

Cancer remains an important global medical challenge. For 2020, the Global Cancer Observatory estimated a total number of 19.3 million new cancer cases and 10 million cancer deaths. The most frequent types are breast cancer (11.7 %), lung cancer (11.4 %) and prostate cancer (7.3 %) (Sung et al., 2021). Therapeutic options for cancer include surgery, radiation therapy and systemic therapies such as chemotherapy and immunotherapy. In many cases, patients are treated with a combination of two or more of these approaches. It is estimated that about 50 % of cancer patients have an indication for radiation therapy at least once during their course of illness (Borras et al., 2015). Radiation therapy is a highly individualized treatment. Modern treatment techniques such as intensity modulated radiotherapy (IMRT) and intensity modulated proton therapy (IMPT) are able to deliver highly conformal dose distributions to target volumes while sparing adjacent healthy organs. Treatment decisions are based on three-dimensional dose calculation, however, these calculations are subject to uncertainties and might differ from the actual dose delivered to the patient for a variety of reasons. In particular, these include (Baumann et al., 2016):

- *setup uncertainty:* imperfect alignment of the patient to the treatment machine
- *motion:* anatomical changes of the patient geometry
- *observer variability:* variations in target delineation
- *range uncertainty:* imperfect prediction of proton range in the patient
- *biological uncertainty:* uncertainty in the prediction of relative biological effectiveness (RBE) of proton beams

Some uncertainties can be reduced through technological solutions, such as image guidance using cone beam computed tomography (CBCT). Before the treatment, CBCT images are acquired. Although these images are not suited for patient dose calculation due to a high scatter contribution, potential setup errors can be detected and corrected by registering them to the patient images used for treatment planning (Oldham et al., 2005). However, in case of non-rigid changes to the patient geometry, e.g. due to tumor shrinkage or patient

weight loss, the resulting dose distribution might differ from the planned one. To take these changes into account, an alternative approach for patient positioning is investigated in this thesis: a scatter-correction approach is used to enable dose calculation on CBCTs and combined with a multi-criterial optimization of the patient position to enable patient positioning based on dosimetric parameters instead of rigid image registration.

Typically residual uncertainties are managed through margin concepts and robust planning approaches (Unkelbach et al., 2018). However, these strategies usually do not take observer variability or biological uncertainty into account. If at all, linear energy transfer (LET) is taken into account as a surrogate for biological effect (Unkelbach et al., 2016; Bai et al., 2019). To quantify the impact of these uncertainties on proton therapy plans, a framework for variance-based sensitivity analysis of uncertainties in proton therapy has been developed in this work. A fast, GPU-based pencil beam algorithm has been implemented to enable a large number of dose calculations while simultaneously sampling from the uncertainty parameters patient position, proton range and RBE model parameter or observers. Since parameters are varied simultaneously, a comprehensive assessment of the combined uncertainty is performed which also takes into account interaction between multiple types of uncertainty. Through statistical evaluation, sensitivity indices, which rank the individual types of uncertainty according to their impact on the overall uncertainty of dosimetric parameters, are calculated.

The structure of this cumulative dissertation is as follows: In chapter 2, an overview over basic physics and basic technological aspects of radiation therapy is given. In chapter 3, methods for uncertainty and sensitivity analysis are briefly discussed, and the numerical method of variance-based sensitivity analysis is described. Chapter 4 contains the studies conducted in the scope of this thesis. In section 4.1, the feasibility and potential benefits of an approach based on dose recalculation on the daily patient anatomy and multi-criterial optimization of the patient position for management of anatomical changes in head and neck cancer is investigated. A study presenting a framework for variance-based sensitivity analysis of setup, range and RBE uncertainty is shown in section 4.2. The framework is later extended to include target delineation variability, which is presented in a technical note in the appendix to this dissertation (see A.1). Finally, in chapter 5, the results are summarized and an outlook on possible future applications of the tools developed in this thesis is given.

Chapter 2

Physics of radiation therapy

In radiotherapy, ionizing radiation is used to destroy or sterilize tumor cells. When the cellular deoxyribonucleic acid (DNA), which carries the genetic information of the cell, is exposed to ionizing radiation, different patterns of damage can occur, among which double strand breaks (DSBs) are the most effective. If the damage to the DNA is sufficient, inactivation or cell death will occur. Different sources and types of radiation are employed in radiotherapy.

In the following two sections, two types of radiation used in external beam therapy (EBT) are briefly discussed: photon beams generated from linear accelerators (LINACs) and proton beams generated from circular accelerators. For the sake of completeness, the following further EBT techniques are mentioned, but not discussed further in this thesis: photon beams for EBT from the radioactive isotope Cobalt-60, and EBT with heavier charged particles such as helium and carbon ions. Brachytherapy, a radiotherapy technique where radioactive sources are introduced into the patient's body, is also not covered in this work.

2.1 LINAC based photon beams

This section gives a short overview of the production of photon beams in LINACs and the interactions of photons with matter.

2.1.1 Linear accelerators

In medical LINACs, electrons are accelerated to energies of several megaelectronvolt (MeV). High energy photons are produced through bremsstrahlung, when these electrons hit a target consisting of a material with high atomic number. Figure 2.1 shows an overview over the individual components of a medical LINAC. In the following, the different components are briefly described. This section was based on Krieger, 2013 and Podgorsak et al., 2005, more detailed information can be found there.

Electron gun

In the electron gun, free electrons are emitted from a heated cathode. These electrons are accelerated by an electric field produced by a static electric potential of typically 15 to 50 kiloelectronvolt (keV) and injected into the waveguide.

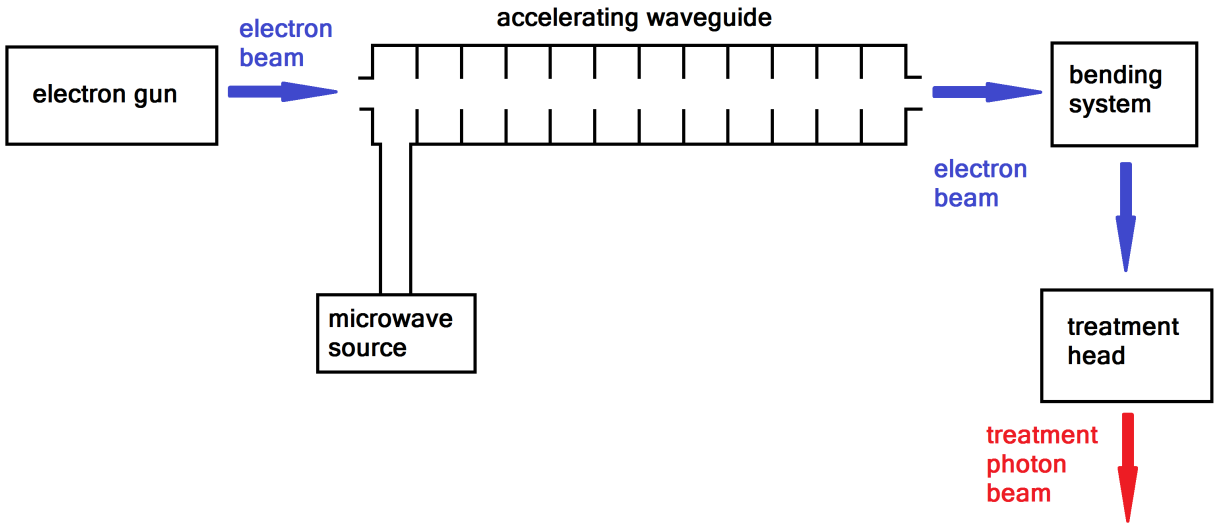

Figure 2.1: Schematic overview of the components of a medical LINAC. Electrons are emitted with energies of several keV from the electron gun, gain energy from the microwave radiation on their way through the accelerating waveguide and enter the treatment head after passing a magnetic steering system. In the treatment head (see also figure 2.4), high energy photons are produced through bremsstrahlung.

Microwave source

The microwave radiation used in a medical LINAC is either produced in a magnetron or a klystron and fed into the waveguide.

Waveguide

In the waveguide, energy is transferred from the electromagnetic field to the electrons. It is a hollow pipe that typically consists of several cavities of copper and transports the microwaves. Two different types of waveguides are common in medical LINACs: In the *traveling waveguide*, electrons continuously gain energy in the field of the electromagnetic wave. The traveling waveguide is illustrated in figure 2.2. In the *standing waveguide*, the microwave gets reflected on the opposite side, which results in the development of a standing wave in the waveguide. Electrons are accelerated when the electric field of the standing wave reaches its maximum value and drift through the waveguide while the standing wave crosses zero. Since the standing waveguide can be designed in a way such

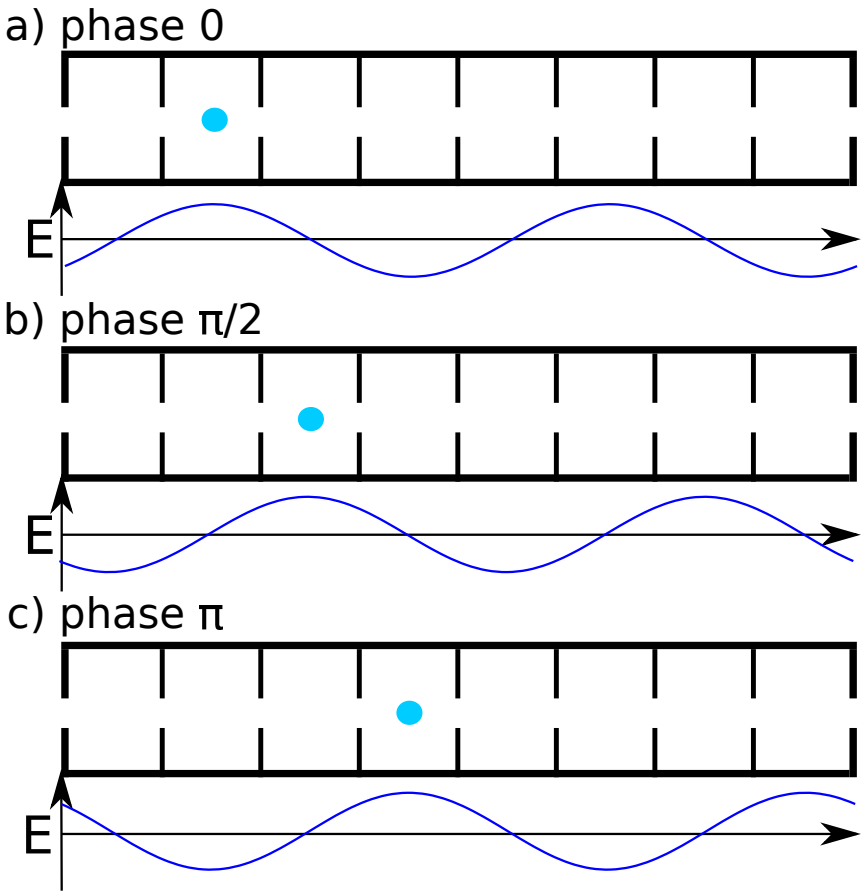

Figure 2.2: Schematic view of a traveling waveguide. As they travel through the waveguide, the electrons continuously gain energy from the electromagnetic field. The electric field is illustrated as a sine wave for simplicity, the actual shape of the wave in a real wave guide is different.

that the nodes of the standing wave, which do not contribute to electron acceleration, are not in the electron beam path, a more compact design is possible for this type of waveguide. The standing waveguide is illustrated in figure 2.3.

Treatment head

A schematic overview of the treatment head of a medical LINAC is shown in figure 2.4. When the electrons leave the waveguide with energies of several MeV, they are bent towards the patient by a magnetic steering system. Since a polyenergetic electron beam would diverge after passing through a single 90° magnet, typically either a combination of three 90° magnets to bend the beam by 270° or a combination of two opposing 45° magnets followed by a 112° magnet ("slalom" design) are used. The beam is directed towards a target that consists of a material of high atomic number, typically tungsten. The electrons lose their energy through bremsstrahlung, which is at these high energies mostly emitted

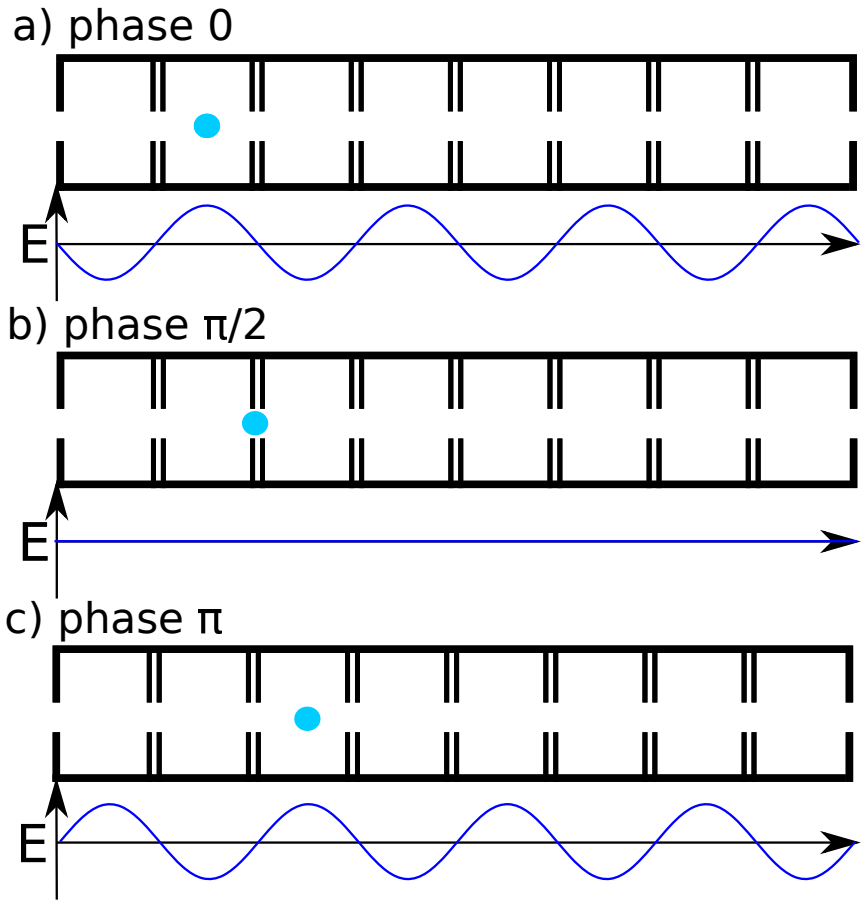

Figure 2.3: Schematic view of a standing waveguide. The nodes of the standing wave, which do not contribute to electron acceleration, are illustrated as shortened cavities here. At phase 0, the electrons indicated by the blue dot experience an accelerating electric field (a). At phase $\pi/2$, the standing wave has zero amplitude. The electrons drift to the next cavity (b). At phase π, the standing wave has changed signs. The electrons experience an accelerating potential again (c). The electric field is illustrated as a sine wave for simplicity, the actual shape of the wave in a real wave guide is different.

in forward direction. The static primary collimator right below the target restricts the radiation field to its maximum size to prevent leakage. Due to the preferred emission of bremsstrahlung in forward direction, the photon fluence emitted from the target is higher on the central beam axis than off-axis. To achieve a homogeneous, flat dose profile special compensators (*flattening filters*) are introduced into the beamline. These have a conical shape to reduce the fluence on the central beam axis. Since lower energy photons are attenuated more strongly than high energy photons (see also section 2.1.3), the flattening filter also leads to a higher mean photon energy in the treatment beam (*beam hardening*). The dose rate, as well as beam symmetry and flatness, are monitored by ion chambers. The final field shape is defined by two or four secondary collimators (*jaws*) in combination

with a multi leaf collimator (MLC). An MLC consists of two opposing banks of tungsten leaves which can move independently to collimate the beam to irregular field shapes.

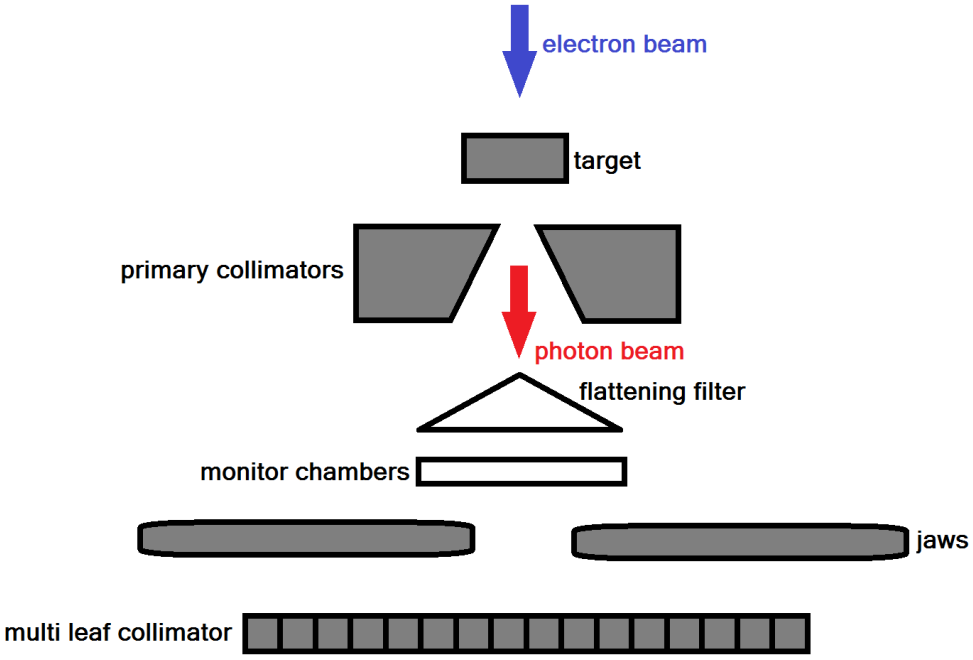

Figure 2.4: Schematic view of a LINAC treatment head. The incident electron beam hits the target, where photons are emitted. Primary collimators restrict the radiation field to its maximum size. The photon beam passes through a flattening filter to achieve a homogeneous fluence profile. The beam is monitored by ion chambers. Jaws and MLC restrict the treatment field to its final, patient-specific shape.

2.1.2 Description of photon beams

Clinical photon beams are typically described in terms of *fluence*

$$\Phi = \frac{dN}{dA}\,, \tag{2.1}$$

where dN is the number of photons passing through a cross-sectional area dA. Another important definition is that of *energy fluence*

$$\Psi = \frac{dE}{dA}\,, \tag{2.2}$$

where dE is the energy passing through dA. The *energy fluence rate* or *intensity* I is defined as (Kahn and Gibbons, 2014):

$$I = \frac{d\Psi}{dt}\,. \tag{2.3}$$

2.1.3 Photon beam attenuation

When a monoenergetic photon beam passes through a medium, the reduction of the number of photons dN that have not undergone any interaction in the medium (*primary photons*) is proportional to the number of incident photons N and the thickness of the medium dx (Kahn and Gibbons, 2014):

$$dN = -\mu N dx\,, \tag{2.4}$$

with the attenuation coefficient μ [cm^{-1}]. This can also be written in terms of the beam intensity I:

$$\frac{dI}{I} = -\mu dx\,. \tag{2.5}$$

This differential equation is solved by the following exponential function:

$$I(x) = I_0 e^{-\mu x}\,. \tag{2.6}$$

In general, μ depends on the density and the atomic composition of the medium as well as the photon energy. For realistic beams with polyenergetic spectra, equation 2.6 has to be integrated over the energy spectrum.

2.1.4 Interactions of photons with matter

Photon beam attenuation is caused by six underlying interactions of photons with matter. One of these interactions is photodisintegration of the atomic nucleus, which, due to the large binding energies of the nucleus, is only relevant for very high photon energies (>10 MeV). The total attenuation coefficient in the therapeutic regime of up to a few MeV μ can therefore be written as the sum of the individual coefficients of the five remaining processes (Kahn and Gibbons, 2014; Hubbell, 1999):

$$\mu = \sigma_{\text{coh}} + \tau + \sigma_{\text{c}} + \pi_{\text{pair}} + \pi_{\text{triplet}}\,, \tag{2.7}$$

where σ_{coh}, τ, σ_{c}, π_{pair} and π_{triplet} denote the coefficients for coherent scattering, photo effect, Compton effect, pair production and triplet production, respectively. In the following, these processes are briefly discussed. More detailed information can be found in Krieger, 2012 and Kahn and Gibbons, 2014.

Coherent scattering

In coherent scattering, the incident photon induces oscillations in the electron hull. The energy of these oscillations is then emitted with the outgoing photon. In this elastic process, incident and outgoing photon have the same energy, but a different direction. No electrons are released from the electron hull. The process is illustrated in figure 2.5. This process does not lead to energy absorption in the medium. For energies above 10 keV, its attenuation coefficient scales approximately as

$$\sigma_{\text{coh}} \propto \rho \frac{Z^{2.5}}{A \cdot E_\gamma^2}\,, \tag{2.8}$$

with the density ρ, the atomic number Z, the mass number A and the photon energy E_γ (Krieger, 2012).

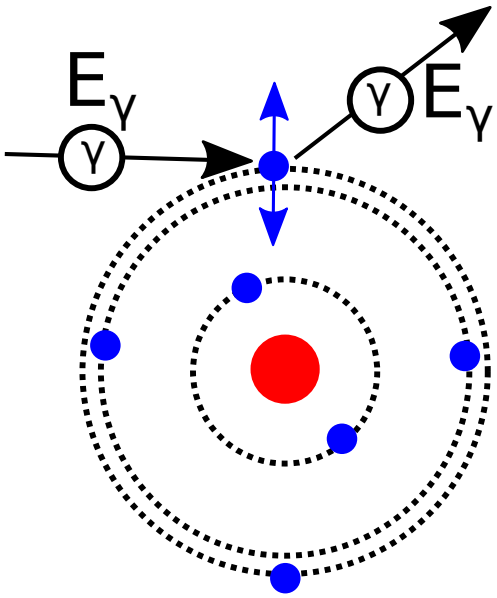

Figure 2.5: Illustration of coherent scattering. The incident photon induces oscillations in the electron hull. A photon of the same energy is emitted.

Photo effect

Through the photo effect, the incident photon is absorbed by the atom. An electron is released from the atom with a kinetic energy equal to the energy of the incident photon E_γ minus the electron binding energy E_B. Consequently, the process can only take place, if the photon energy E_γ is larger than the binding energy E_B. The missing inner electron is replaced by one of the outer electrons. The excess hull energy can either result in the emission of a photon which has the energy of the difference ΔE between the electron energy levels, as shown in figure 2.6, or release hull electrons from the atom (*Auger* emissions). The attenuation coefficient for this process is varies approximately as

$$\tau \propto \rho \frac{Z^n}{A \cdot E_\gamma^3} \quad \text{for } E_\gamma \ll 511\mathrm{keV} \quad \text{and} \tag{2.9}$$

$$\tau \propto \rho \frac{Z^n}{A \cdot E_\gamma} \quad \text{for } E_\gamma \gg 511\mathrm{keV}\,, \tag{2.10}$$

where the exponent $n \approx 4 - 4.5$. The photo effect plays an important role for X-ray imaging, where typically photon energies of up to 150 keV are used. Due to the decrease of τ with increasing photon energies, the photo effect does not play a major role for primary photons in therapeutic beams with energies in the MeV regime. Secondary and tertiary photons that are produced in the patient, however, are of lower energy and also contribute

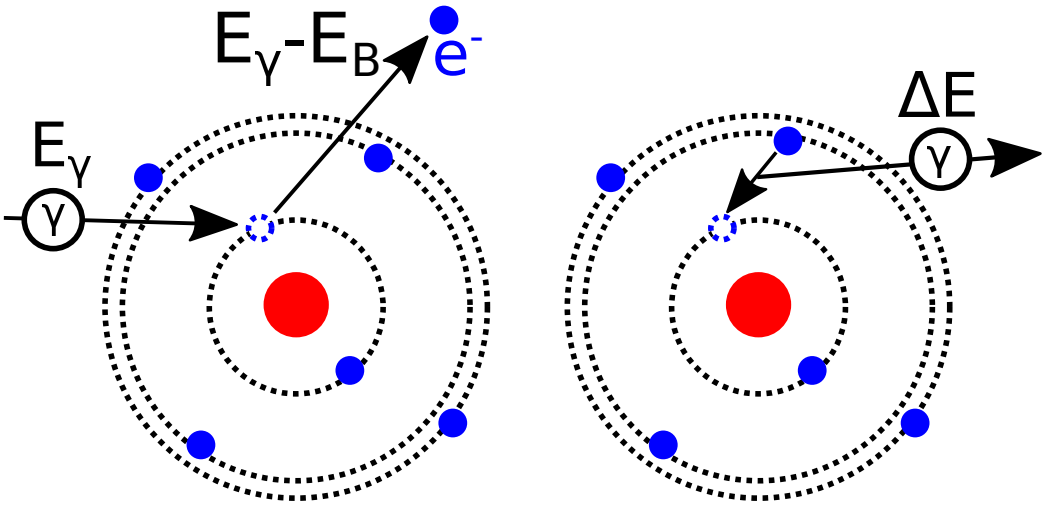

Figure 2.6: Illustration of the photo effect. The incident photon transfers its energy to an electron and liberates it from the hull. When electrons from higher energy levels replace the missing electron, a photon is emitted.

to patient dose. For this reason the photo effect cannot be neglected during radiotherapy dose calculation.

Compton effect

The Compton effect is the interaction of an incident photon with a weakly bound electron of an outer shell. The photon is scattered and parts of its energy are transferred to the electron, which is released from the atom. The energy of the outgoing photon $E_{\gamma'}$ is

$$E_{\gamma'} = \frac{E_\gamma}{1 + \frac{E_\gamma}{m_0 c^2} \cdot (1 - \cos\phi)}\,, \tag{2.11}$$

where E_γ is the energy of the incident photon and ϕ is the scattering angle. For therapeutic photon energies in the MeV regime, the angular distribution of both outgoing photon and electron is strongly peaked in forward direction. The process is illustrated in figure 2.7. The coefficient of the Compton effect σ_c varies approximately as

$$\sigma_\mathrm{c} \propto \rho \frac{Z}{A} E_\gamma^{-n}\,, \tag{2.12}$$

where $n \approx 0.5 - 1$. The Compton effect is the dominant contribution to the total attenuation coefficient for photon beams in the therapeutic energy range.

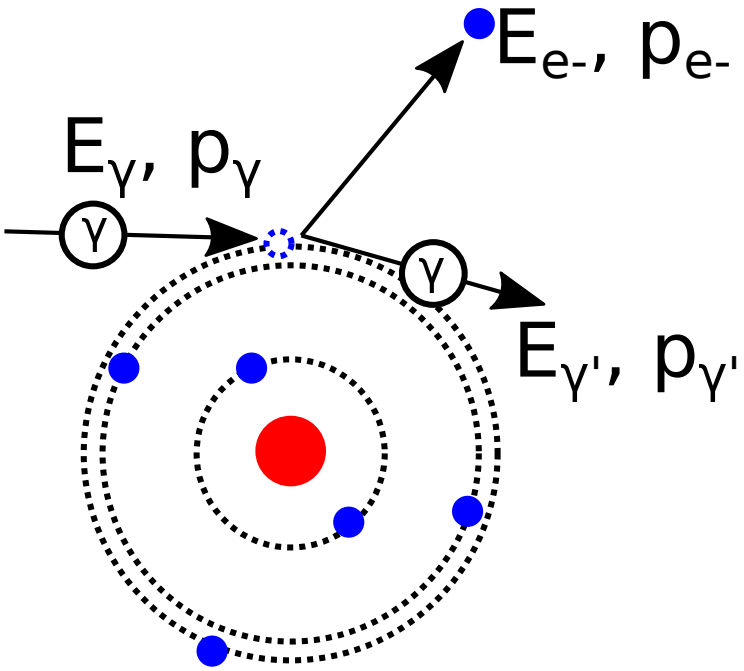

Figure 2.7: Compton effect. The incident photon is scattered and transfers parts of its energy to a hull electron.

Pair and triplet production

In the electric field of an atomic nucleus, a photon can spontaneously produce an electron-positron pair. Since the mass energy of both the electron and the positron are 511 keV, the process cannot take place below the threshold of 1022 keV. The coefficient for pair production above the threshold scales approximately as

$$\pi_{\text{pair}} \propto \frac{Z^2}{A} \cdot \rho \log E_\gamma \,. \tag{2.13}$$

The process can rarely also take place with an electron as interaction partner, due to the three resulting particles, this is called triplet production. Due to reasons of conservation of energy and momentum, the threshold for triplet production is 2044 keV. Above this threshold, the coefficient for triplet production is approximately (Hubbell, 1999):

$$\pi_{\text{triplet}} \approx \frac{\pi_{\text{pair}}}{Z} \,. \tag{2.14}$$

Both pair and triplet production are illustrated in figure 2.8.

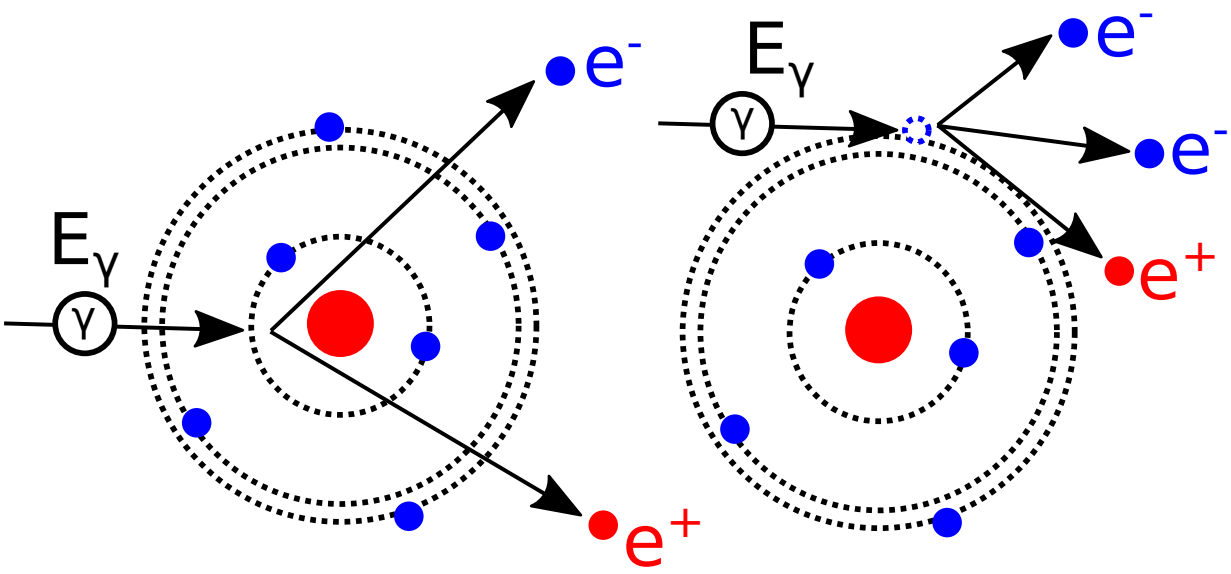

Figure 2.8: Pair and triplet production. The photon energy is converted to an electron-positron pair. The process can take place in the field of an atomic nucleus (pair production, left) or with an electron as interaction partner (triplet production, right).

2.1.5 Absorbed dose

Absorbed dose is defined as the mean energy $d\bar{\epsilon}$ imparted by ionizing radiation to a medium with the mass dm:

$$d = \frac{d\bar{\epsilon}}{dm}\,. \tag{2.15}$$

It has the unit gray (Gy), which is defined as joule per kilogram. Absorbed dose is a surrogate measure for the biological effects of ionizing radiation on tumor cells and healthy tissue. In photon treatment planning, the distribution of absorbed dose in the patient is evaluated to estimate the probability of tumor control and side effects. In proton therapy, the physical dose distribution as the sole measure of biological effect has limitations, as will be discussed later.

Energy transfer coefficient

When a photon interacts with matter via one of the processes discussed above, this can lead to conversion of parts or almost all of its energy to kinetic energy of secondary charged particles. To describe which fraction of the energy is actually converted to kinetic energy, the energy transfer coefficient is defined as

$$\mu_{\mathrm{tr}} = \frac{\bar{E}_{\mathrm{tr}}}{E_\gamma} \cdot \mu\,, \tag{2.16}$$

where $\bar{E}_{\mathrm{tr}}$ is the mean energy transferred to kinetic energy of charged particles per interaction (Kahn and Gibbons, 2014).

Energy absorption coefficient

Secondary charged particles will either lose their energy by locally ionizing or exciting atoms of the medium or lose their energy through bremsstrahlung via Coulomb interaction with the atomic nuclei (and to a lesser extent with hull electrons). In the case of positrons, also in-flight annihilation contributes to radiative losses. To take into account that these radiative energy losses do not contribute to local energy deposition, the energy absorption coefficient is defined as

$$\mu_{\mathrm{en}} = \mu_{\mathrm{tr}}(1-g)\,, \tag{2.17}$$

where g is fraction by which the kinetic energy of secondary charged particles is reduced through radiative losses (Kahn and Gibbons, 2014).

2.1.6 KERMA

Kinetic energy released per unit mass (KERMA) K is the kinetic energy transferred to secondary charged particles per unit mass. It is only defined for indirectly ionizing radiation such as photons and is related to the energy transfer coefficient via

$$K = \frac{dE_{\mathrm{tr}}}{dm} = \Psi\left(\frac{\mu_{\mathrm{tr}}}{\rho}\right)\,, \tag{2.18}$$

where Ψ is the energy fluence of the beam (Kahn and Gibbons, 2014). KERMA can be disentangled to distinguish the kinetic energy of secondary charged particles leading to ionization and excitation (collision KERMA K_{col}) from the energy lost via bremsstrahlung or in-flight annihilation (radiative KERMA K_{rad}):

$$K = K_{\mathrm{col}} + K_{\mathrm{rad}}\,, \tag{2.19}$$

where

$$K_{\mathrm{col}} = \Psi\left(\tfrac{\mu_{\mathrm{en}}}{\rho}\right) = \Psi\left(\frac{\mu_{\mathrm{tr}}}{\rho}\right)(1-g) \quad \text{and} \tag{2.20}$$

$$K_{\mathrm{rad}} = \Psi\left(\frac{\mu_{\mathrm{tr}}}{\rho}\right) g\,. \tag{2.21}$$

Since for low photon energies and in low Z materials g is negligible ($K_{\mathrm{col}} \approx K$) and secondary charged particles have negligible range, KERMA is equal to absorbed dose in this case. For therapeutic photon energies in the MeV regime, secondary charged particles have kinetic energies high enough to travel a certain distance though the medium, therefore collisional KERMA is equal to absorbed dose only under charged particle equilibrium (CPE) conditions. CPE holds if the kinetic energy of secondary charged particles leaving a volume is on average equal to the energy of secondary charged particles entering the volume. Since secondary charged particles are released preferably in forward direction for clinical photon energies, this leads to a build-up region where CPE is not yet reached (see figure 2.9).

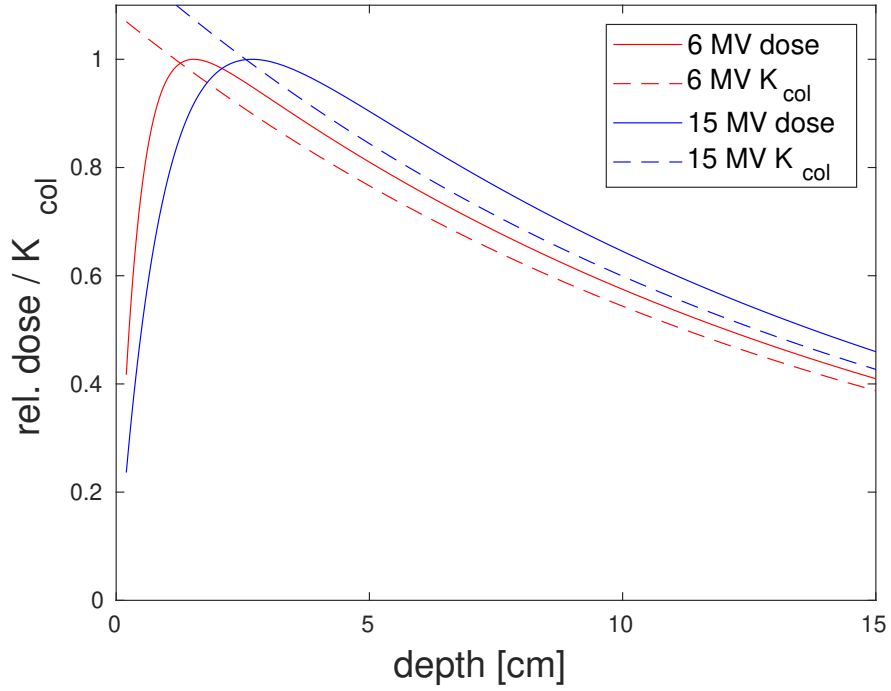

Figure 2.9: Schematic view of collisional KERMA and dose for two therapeutic photon beam energies in water. With increasing depth, there is an exponential decay of collisional KERMA. Since the released secondary charged particles travel a certain distance before losing their energy, the dose increases from the surface ("build up") until reaching the maximum depth, which increases with the beam energy. At this maximum depth collisional KERMA and absorbed dose coincide. After the maximum depth, dose is larger than K_{col} ($\beta > 1$) and both decrease exponentially due to the photon beam attenuation in the medium.

This is advantageous for treating deep seated tumors, since it allows to spare the radiosensitive skin. After the build-up region, at maximum depth, CPE is fulfilled and $K_{\mathrm{col}} = d$. Due to attenuation of the primary photon beam, CPE is no longer present at depths larger than the maximum depth. In this region of transient charged particle equilibrium (TCPE), absorbed dose is greater than collisional KERMA since the dose is deposited by secondary charged particles originating upstream. In this case, dose is proportional to collisional KERMA:

$$d \overset{\mathrm{TCPE}}{=} \beta \cdot K_{\mathrm{col}} \tag{2.22}$$

with factor $\beta > 1$.

2.1.7 TERMA

The total energy released per unit mass (TERMA) T has a similar definition as KERMA. It includes all energy lost by the primary beam in the medium, including also energy transferred to scattered photons:

$$T = \frac{dE}{dm} = \Psi \left(\frac{\mu}{\rho} \right) . \tag{2.23}$$

It is mostly used for analytical photon dose calculation with dose kernels which describe the energy transport of the secondary charged particles and photons from the primary photon interaction point (Schlegel, Karger, and Jäkel, 2018, see section 2.4.2).

2.1.8 Radiological distance

To take into account tissue heterogeneities, density scaling can be applied. The radiological distance z_{rad} between two points r_0 and r_1 is defined as the distance between the two points scaled with the electron density relative to water

$$z_{\mathrm{rad}}(\mathbf{r_0}, \mathbf{r_1}) = \int_{\mathbf{r_0}}^{\mathbf{r_1}} \frac{\rho_e(\mathbf{r})}{\rho_{e,W}} d\mathbf{r} \, , \tag{2.24}$$

where $\rho_e(\mathbf{r})$ denotes the electron density in the point $\mathbf{r}$, $\rho_{e,W}$ denotes the electron density of water and the integral is performed along the line connecting the two points $\mathbf{r_0}$ and $\mathbf{r_1}$ (Kahn and Gibbons, 2014). This quantity is particularly useful for dose calculation, where the integral is performed along the central beam axis (*ray tracing*).

2.2 Proton beams

This section gives a short overview over the production of proton beams in circular accelerators, their physical interactions with matter and their radiobiological effect.

2.2.1 Circular accelerators

Unlike in linear accelerators, where particles pass through the acceleration section only once, in circular accelerators particles are passing the acceleration section multiple times while successively gaining energy during each cycle. In proton therapy both cyclotrons and synchrotrons are used as proton accelerators (Amaldi et al., 2010). They are briefly discussed in the following sections.

Classical cyclotron

When a charged particle moves on a circular path in a stationary and homogeneous magnetic field perpendicular to the orbital plane, the cycling frequency ω is

$$\omega = \frac{q}{\gamma m_0} B \,, \tag{2.25}$$

where q is the charge of the particle, m_0 is its rest mass, B is the magnetic field strength and γ is the Lorentz factor (Hinterberger, 2008). The basic idea of a cyclotron is to keep ω constant and accelerate the protons by an alternating electric field of the same frequency. In the non-relativistic case ($\gamma \approx 1$), ω is constant for a constant magnetic field. Momentum p and radius r are related via

$$p = qBr \,. \tag{2.26}$$

Figure 2.10 shows a schematic view of a cyclotron. To accelerate the protons each time they pass through the gap, an alternating electric field is applied with the cyclotron frequency for non-relativistic particles (Hinterberger, 2008):

$$\nu_{\mathrm{cyc}} = \frac{1}{2\pi} \frac{q}{m_0} B \,. \tag{2.27}$$

As the protons gain energy, the radius increases according to equation 2.26. They spiral outward and are extracted. The energy the protons gain when they pass through the gap with phase shift φ is

$$\Delta E = q U_0 \cos\varphi \,, \tag{2.28}$$

where U_0 is the acceleration voltage. For $\varphi = 0$ the acceleration reaches its maximum, while for values above 90°, the proton is decelerated. Once the proton approaches energies which make the non-relativistic approximation break down, equation 2.27 no longer holds and the cycling frequency decreases. This lets the protons eventually lose synchronicity with the accelerating voltage and limits the proton energies which can be achieved with classical cyclotrons to 10-20 MeV, rendering these devices insufficient for proton therapy, where energies of up to 250 MeV are needed.

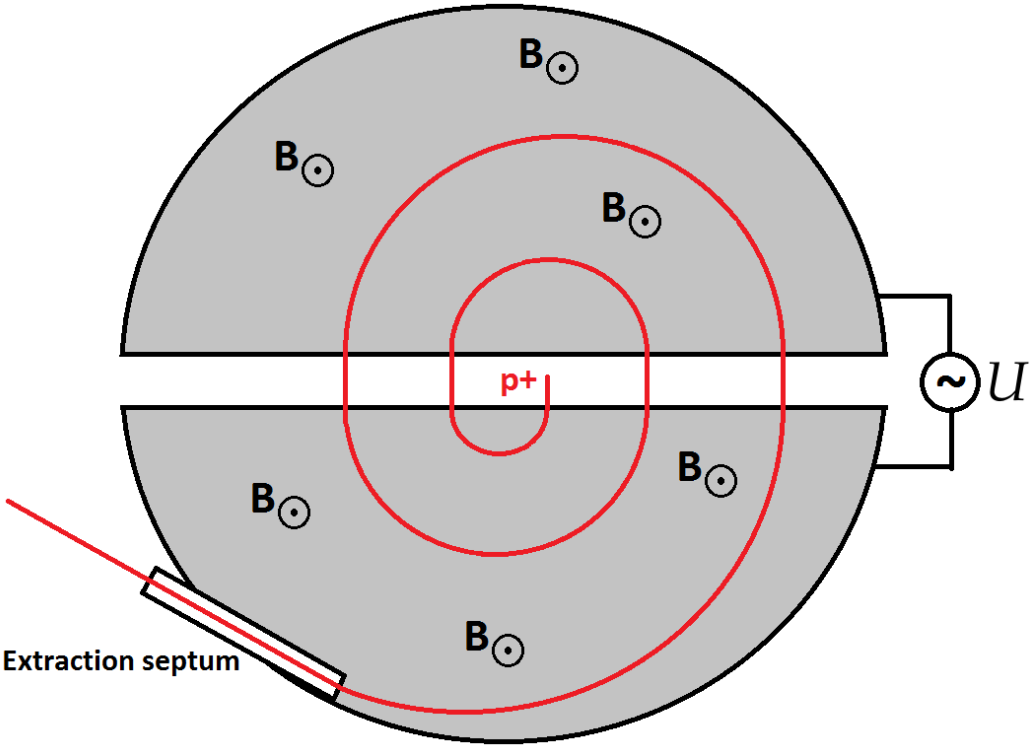

Figure 2.10: Schematic view of a cyclotron. The protons are accelerated by an alternating voltage as they pass through the gap between the two half cylinders. The protons are forced on a spiral trajectory by a magnetic field B (out of plane in this image). As the protons gain energy, the radius increases. Once the extraction energy is reached, the protons leave the cyclotron through the extraction septum.

Synchrocyclotron

To overcome the energy limitation of the classical cyclotron, the synchrocyclotron was developed. In this approach, the frequency of the accelerating electric field is modulated to compensate for the relativistic decrease in proton cycling frequency:

$$\omega(r) = \frac{q}{\gamma(r) m_0} B \,. \tag{2.29}$$

Since synchronicity is only achieved for one bunch of protons per modulation cycle, this leads to a pulsed beam with the modulation frequency, and, in consequence, to a relatively low ion current. Proton energies of up to about 800 MeV can be achieved (Hinterberger, 2008). The first proton treatment was delivered in Berkeley in the 1950s using a synchrocyclotron whose acceleration chamber had a diameter of 184 inch ($\approx$ 4.7 meters) (Tobias et al., 1958). Later, much more compact designs were achieved by using superconducting magnets with higher magnetic field strengths. These are particularly suited for single-room proton therapy facilities. In the past few years, compact superconducting synchrocyclotrons for

proton therapy became commercially available and have been introduced into the clinic (Contreras et al., 2017; Forsthoefel et al., 2020).

Isochronous cyclotron

The isochronous cyclotron uses another approach to overcome the limitations of the classical cyclotron. Instead of modulating the frequency of the accelerating electric field, the cycling frequency of the proton is kept constant by using a magnetic field which increases with the beam radius:

$$\omega = \frac{q}{\gamma m_0} B(r) = const. \tag{2.30}$$

Since this field has an axially de-focusing effect, additional measures are necessary to compensate this. By employing the principle of *strong focusing*, the protons can be axially focused by azimuthal variations of the magnetic field. Proton energies of up to about 600 MeV can be achieved, with sharp energy spectra (Hinterberger, 2008).

Synchrotron

Another type of circular accelerator used for proton therapy is the synchrotron. In the synchrotron, the protons are accelerated while cycling a circular tube and repeatedly passing through a radio frequency (RF) cavity. The magnetic field guiding the protons is restricted to the ring, where dipole magnets are used to bend and quadrupole magnets are used to focus the beam. In this type of accelerator, a constant proton radius is required. Therefore the magnetic field strength needs to be increased in synchrony with the energy gain of the protons. Since this synchronization cannot be started at zero kinetic energy, the protons need to be injected into the synchroton after pre-accelerating them, which is typically done using a LINAC (Krieger, 2013).

2.2.2 Interactions of protons with matter

When charged particles interact with a medium, they interact with the atoms of the medium via Coulomb interactions. The average energy loss dE per path length dx is described by the total stopping power

$$S_{\mathrm{tot}} = \left(\frac{dE}{dx}\right)_{\mathrm{tot}} . \tag{2.31}$$

The total stopping power is the sum of energy losses due to electronic collisions S_{col}, radiative losses due to bremsstrahlung S_{rad} and losses through elastic Coulomb scattering with the atomic nuclei (nuclear stopping power, S_{nuc}):

$$S_{\mathrm{tot}} = S_{\mathrm{col}} + S_{\mathrm{rad}} + S_{\mathrm{nuc}} . \tag{2.32}$$

S_{nuc} is relevant only at very low proton energies below ~10 keV. Above 1 MeV, it contributes less than 0.1% to the total stopping power (Paganetti, 2012a). For protons, S_{rad} scales as

$$S_{\text{rad}} \propto \rho \left(\frac{e}{m}\right)^2 \cdot \frac{Z^2}{A} \cdot E\,, \tag{2.33}$$

where m denotes the proton mass (Krieger, 2012). While for electrons radiative losses are important, for heavier particles such as protons in the therapeutic energy range (up to about 250 MeV), S_{rad} can be neglected due to the dependence on m^{-2}. The total stopping power can therefore be approximated as:

$$S_{\text{tot}} \approx S_{\text{col}} = \left(\frac{dE}{dx}\right)_{\text{col}}\,. \tag{2.34}$$

For proton energies above approximately 1 MeV, the collision stopping power can be calculated with the Bethe-Bloch equation

$$\left(\frac{dE}{dx}\right)_{col} = k \cdot \rho \cdot \frac{Z}{A} \cdot \frac{z^2}{\beta^2} \cdot L(\beta)\,, \tag{2.35}$$

where $k \approx 0.307$ MeV $\cdot\, {}^{\text{cm}^2}/_{\text{g}}$, the atomic number of the medium Z, the mass number of the medium A, the charge of the particle z (for protons: $z = 1$) and the velocity of the particle $\beta = {}^{v}/_{c}$ (Schlegel, Karger, and Jäkel, 2018). $L(\beta)$ is a complex function and contains weaker dependencies on velocity and material properties:

$$L(\beta) = \frac{1}{2} \ln\left(\frac{2m_{\text{e}}c^2\beta^2}{I(1-\beta^2)}\right) - \beta^2\,, \tag{2.36}$$

where m_{e} is the electron mass and I is the mean excitation potential of the medium (Krieger, 2012). As a consequence of the inverse dependence on β^2 in equation 2.35, the stopping power increases with decreasing particle velocity. For this reason, protons and heavier charged particles tend to lose their energy at the end of their path, a phenomenon known as the *Bragg peak*. Since protons do not lose their energy continuously, but in a finite number of stochastic interaction events, protons with the same initial energy do not stop at the exact same depth. For water, the proton range is approximately normal distributed with a standard deviation of 1.2% of the mean range (Paganetti, 2012a). This *range straggling* reduces the sharpness of the Bragg peak with increasing depth. Proton depth-dose curves for various proton energies are shown in figure 2.11. To achieve a homogeneous coverage of a tumor, the superposition of multiple Bragg peaks (that is, multiple initial proton energies) is required to achieve a spread-out Bragg peak (SOBP). The dosimetric characteristics of protons have the advantage of delivering a lower integral dose to the patient, but have also the disadvantage that additional uncertainty is introduced into the dose calculation by imperfect proton range prediction (see also section 2.6.2).

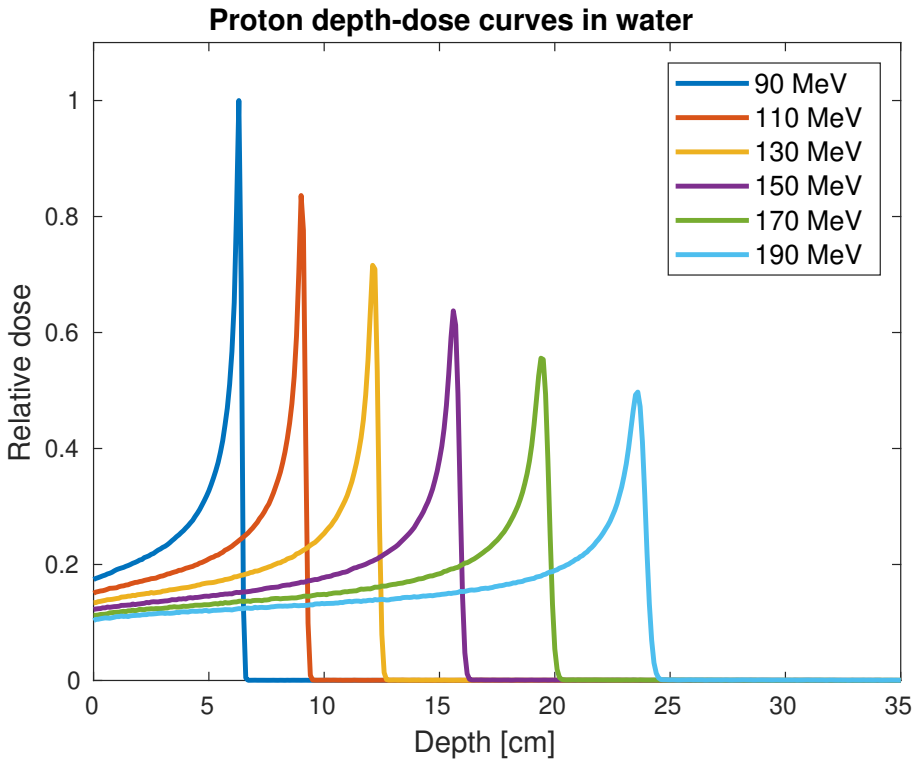

Figure 2.11: Depth-dose curves in water for various clinically relevant proton energies simulated using the Monte Carlo code Geometry and Tracking 4 (Geant4)[1]. Most of the proton energy is transferred to the tissue near the end of the proton path, at the *Bragg peak*. The depth of the Bragg peaks depends on the incident proton energy. To achieve a homogeneous coverage of a tumor, the superposition of multiple proton energies is required to achieve a *spread out Bragg peak (SOBP)*.

[1] Courtesy of George Dedes, Faculty of Physics, Department of Medical Physics, LMU Munich

2.2.3 Linear energy transfer

The linear energy transfer (LET) is the energy per path length transferred to secondary electron through collisions, where only secondary electrons below an energy threshold Δ are considered:

$$L_\Delta = \left(\frac{dE}{dx}\right)_{\mathrm{col},\Delta} . \tag{2.37}$$

By definiton is

$$L_\Delta \leq S_{\mathrm{col}} \tag{2.38}$$

and

$$L_{\Delta\to\infty} = S_{\mathrm{col}} . \tag{2.39}$$

It is the mean energy imparted per unit path length within a finite radius (depending on the cutoff energy Δ) around the primary particle track. It is an important quantity in radiobiology, where a higher LET implicates a higher biological effect. This will be discussed in section 2.3.

2.2.4 Specific energy

Another important physical quantity which is relevant in the context of radiobiology is the *specific energy*. It is defined as the energy ϵ imparted to matter of mass m divided by m:

$$z = \frac{\epsilon}{m} , \tag{2.40}$$

where $\epsilon = \sum_i \epsilon_i$ is the sum of a finite number of energy deposition events. Due to the stochastic nature of energy deposition through ionizing radiation in a medium, z is also a stochastic quantity whose variance increases for small masses, low doses and densely ionizing radiation. By averaging over the single event probability distribution $f_1(z)$, the *frequency-mean specific energy* $\bar{z}_F$ is obtained as (Rossi and Zaider, 1996):

$$\bar{z}_F = \int_0^\infty z f_1(z) dz . \tag{2.41}$$

2.3 Radiobiology

In this section, radiobiological aspects in photon and proton therapy are briefly discussed.

2.3.1 Linear quadratic model

In the linear quadratic model the surviving fraction of cells irradiated with a photon dose d_X is modeled as

$$SF(d_\mathrm{X}) = \exp(-\alpha_\mathrm{X} d_\mathrm{X} - \beta_\mathrm{X} {d_\mathrm{X}}^2)\,, \tag{2.42}$$

where α_X and β_X are the X-ray radiosensitivity parameters of the cell. Although this is a simple empirical model for cell survival, it has a radiobiological interpretation: The linear term in the exponent can be interpreted to correspond to particle tracks which on their own inflict lethal damage to a cell. On the contrary, the quadratic term is interpreted to correspond to particle tracks that on their own inflict sublethal damage to the cell but are lethal if a cell is hit twice (Schlegel, Karger, and Jäkel, 2018). The linear quadratic model is frequently used in radiotherapy to model the effect of fractionation on cell survival. For example, under the simplest assumptions that in between fractions sublethal damage is repaired completely and that there is no proliferation of tumor cells, the survival fraction after n fractions with a fraction dose of d_X is

$$SF(n d_\mathrm{X}) = \exp(-n\alpha_\mathrm{X} d_\mathrm{X} - n\beta_\mathrm{X} {d_\mathrm{X}}^2)\,. \tag{2.43}$$

There are refined models including incomplete repair, proliferation and other effects (Schlegel, Karger, and Jäkel, 2018; McMahon, 2019).

2.3.2 Relative biological effectiveness

In photon therapy, dose prescription and constraints for healthy tissues are based on the physical quantity of absorbed dose. For proton therapy, and even more so for treatment with heavier ions, the same absorbed dose as for photon therapy may result in a different biological effect. This arises from the fact that these types of radiation have different microscopic dose deposition characteristics. To make dose prescriptions in proton therapy comparable to those in photon therapy the relative biological effectiveness (RBE) is defined as the ratio of the photon dose d_X to elicit a certain biological effect to the proton dose d_P which is necessary to trigger the same effect (e.g. Paganetti et al., 2019):

$$RBE(endpointX) = \frac{d_\mathrm{X}(endpointX)}{d_\mathrm{P}(endpointX)}\,. \tag{2.44}$$

Biological effect is hereby defined for a certain endpoint, e. g. survival fractions for a tumor cell type or a clinical endpoint such as the occurrence of a side effect in normal tissue. For protons, a spatially constant RBE of 1.1 is commonly assumed, a practice originating from *in vivo* measurements of the RBE at the center of the SOBP for a fraction dose of 2 Gy from the 1970s (Paganetti et al., 2019). However, the actual RBE is known to increase with

LET and therefore towards the end of the SOBP (Lühr et al., 2018). Variable RBE models are typically based on the linear quadratic model and aim at modeling the corresponding sensitivity parameters for proton radiation α_P and β_P. They can be categorized into empirical models, which are based on parameter fits to *in vitro* cell survival data, and mechanistic models explaining the biological effects of ion radiation in terms of biological mechanisms processing sublethal damage into more lethal forms of damage (Paganetti et al., 2019). With (tumor) cell survival as biological endpoint and equation 2.42, biological equivalence implies

$$SF_{\mathrm{Proton}}(d_P) = SF_X(RBE \cdot d_X) \tag{2.45}$$

and therefore

$$\exp(-\alpha_P d_P - \beta_P {d_P}^2) = \exp(-\alpha_X \cdot RBE \cdot d_X - \beta_X \cdot RBE^2 \cdot {d_X}^2)\,. \tag{2.46}$$

In general, α_P and β_P are energy dependent. For polyenergetic spectra, dose-weighted integrals of α_P and $\sqrt{\beta_P}$ need to be used (Zaider and Rossi, 1980):

$$\alpha_{P,d_P} = \frac{\int \alpha_P(E)\Phi(E)S(E)dE}{\int \Phi(E)S(E)dE} \quad \text{and} \tag{2.47}$$

$$\sqrt{\beta_{P,d_P}} = \frac{\int \sqrt{\beta_P(E)}\Phi(E)S(E)dE}{\int \Phi(E)S(E)dE}\,, \tag{2.48}$$

where Φ is the particle fluence spectrum and S is the collisional stopping power. By using the definition of RBE in equation 2.44, equation 2.46 can be resolved to (Paganetti, 2018):

$$RBE(\alpha_X, \beta_X, \alpha_P, \beta_P, d_P) = \frac{\sqrt{\alpha_X^2 + 4\beta_X d_P(\alpha_P + \beta_P d_P)} - \alpha_X}{2\beta_X d_P}\,. \tag{2.49}$$

Several ways to model α_P and β_P exist, in the following sections two of them, which were used in the scope of this thesis, are briefly discussed: First, the empirical Wedenberg model, which is based on linear fits to *in vitro* cell survival data (Wedenberg, Lind, and Hårdemark, 2013). And second, the mechanistic repair-misrepair-fixation (RMF) model which is based on modeling of sublethal damage and its biological processing (Carlson et al., 2008). Other established models, such as the mechanistic local effect model (LEM), the mechanistic microdosimetric-kinetic model (MKM) and the empirical models by McNamara, Carabe and Wilkens were not used in the scope of this thesis and are therefore not covered here (for reviews see Paganetti et al., 2019 and Karger and Peschke, 2018).

Wedenberg model

The aim of the Wedenberg model (Wedenberg, Lind, and Hårdemark, 2013) is to provide a simple, empirical RBE model which also holds for different cell lines (that is, different α_X/β_X ratio). For a given cell line, a simple linear dependence on LET is assumed for α_P:

$$\frac{\alpha_P}{\alpha_X} = 1 + k \cdot LET\,. \tag{2.50}$$

The slope k for different cell lines is assumed to be inversely proportional to their respective X-ray reference sensitivity parameters. By introducing

$$q = k \cdot \frac{\alpha_{\mathrm{X}}}{\beta_{\mathrm{X}}} \,. \tag{2.51}$$

equation 2.50 becomes

$$\frac{\alpha_{\mathrm{P}}}{\alpha_{\mathrm{X}}} = 1 + \frac{q}{\alpha_{\mathrm{X}}/\beta_{\mathrm{X}}} \cdot LET \,. \tag{2.52}$$

Furthermore, β_{P} is assumed to be independent of LET and equal to β_{X}:

$$\frac{\beta_{\mathrm{P}}}{\beta_{\mathrm{X}}} = 1 \,. \tag{2.53}$$

With these assumptions, q is the only free parameter of the model and independent of the $\alpha_{\mathrm{X}}/\beta_{\mathrm{X}}$ ratio. By fitting the model to *in vitro* data for 10 different cell lines with various $\alpha_{\mathrm{X}}/\beta_{\mathrm{X}}$ ratios, q is determined to be

$$q = 0.434 \text{ Gy} \frac{\mu\text{m}}{\text{keV}} \,. \tag{2.54}$$

In this model, RBE only depends on the proton dose, the LET and the $\alpha_{\mathrm{X}}/\beta_{\mathrm{X}}$ ratio for the given cell line. Equation 2.49 becomes

$$RBE(\alpha_{\mathrm{X}}/\beta_{\mathrm{X}}, d_{\mathrm{P}}, LET) = \frac{\sqrt{(\alpha_{\mathrm{X}}/\beta_{\mathrm{X}})^2 + 4d_{\mathrm{P}}(\alpha_{\mathrm{X}}/\beta_{\mathrm{X}} + q \cdot LET + d_{\mathrm{P}})} - \alpha_{\mathrm{X}}/\beta_{\mathrm{X}}}{2d_{\mathrm{P}}} \,. \tag{2.55}$$

Due to the linearity of equation 2.52, the dose-weighted $\alpha_{P,D}$ required for polyenergetic spectra can be calculated by evaluating it with the dose-weighted $LET_{d_{\mathrm{P}}}$:

$$LET_{d_{\mathrm{P}}} = \frac{\int LET(E)\Phi(E)S(E)dE}{\int \Phi(E)S(E)dE} \,. \tag{2.56}$$

RMF model

The mechanistic RMF model (Carlson et al., 2008) links DSB induction to reproductive cell death by modeling the processing of DSBs by repair mechanisms in the cell to lethal and non-lethal outcomes. Estimates for DSB yields from a Monte Carlo damage simulation (MCDS) (Semenenko and Stewart, 2004; Semenenko and Stewart, 2006) are used as an input. In this model, five possible mechanisms for the processing of initial DSBs into lethal forms of damage are considered:

- single DSB is intrinsically unrejoinable
- initially rejoinable, single DSB becomes unrejoinable through extrinsic fixation
- lethal misrepair of single DSB

- lethal binary misrepair of pair of DSBs from the same particle track
- lethal binary misrepair of pair of DSBs from different particle tracks

The change of the average number of potentially rejoinable DSBs L in a cell within a group of cells uniformly irradiated with dose rate $\dot{d}(t)$ is modeled with the balance equation

$$\frac{dL(t)}{dt} = f_{\mathrm{R}}\Sigma\dot{d}(t) - (\lambda + \eta f_{\mathrm{R}}\bar{z}_F\Sigma)L(t) - \eta L(t)^2\,, \tag{2.57}$$

where f_{R} is the fraction of potentially rejoinable DSBs, Σ is the rate of DSB induction, $\lambda = \lambda_{\mathrm{R}} + \lambda_{\mathrm{F}}$ is the sum of DSB repair (λ_{R}) and fixation (λ_{F}) rates, η is the rate of binary misrepair and $\bar{z}_F$ is the frequency-mean specific energy defined in section 2.2.4. The first term models the number of rejoinable DSBs generated by the irradiation and the second term (linear in L) models the removal of DSBs by pairwise interaction between DSBs of the same particle track (repair, misrepair, fixation of damage). The third term (quadratic in L) corresponds to the removal of DSBs through pairwise interaction of DSBs of different particle tracks (binary misrepair). The expected rate of change in the number of lethal DNA damages per cell F is modeled with the balance equation

$$\frac{dF(t)}{dt} = (1 - f_{\mathrm{R}})\Sigma\dot{d}(t) + (\Theta\lambda + \gamma\eta f_{\mathrm{R}}\bar{z}_F\Sigma)L(t) + \gamma\eta L(t)^2\,, \tag{2.58}$$

where γ is the probability of a lethal misrejoining of two DSBs and with

$$\Theta \equiv \frac{[(1-a)\varphi\lambda_{\mathrm{R}} + \lambda_{\mathrm{F}}]}{\lambda}\,, \tag{2.59}$$

where $(1-a)$ is the probability that a single DSB is misrepaired and φ is the probability that a misrepaired DSB is lethal. In equation 2.58, the first term accounts for intrinsically unrejoinable DSBs, the second term, which is linear in L, accounts for extrinsic fixation of DSBs, lethal misrepair of single DSBs and lethal binary misrepair of DSBs from the same particle track. The third term, quadratic in L, accounts for lethal binary misrepair of DSBs from different particle tracks. By estimating survival fractions from a time integrated solution of the RMF model,

$$SF(d) = \exp[-F(t \to \infty)] = \exp[-(\alpha d + \beta d^2)]\,, \tag{2.60}$$

and under the assumption that all DSBs are potentially rejoinable ($f_{\mathrm{R}} = 1$), linear quadratic parameters can be obtained as

$$\alpha = \Theta\Sigma + \kappa\bar{z}_F\Sigma^2 \quad \text{and} \tag{2.61}$$

$$\beta = (\kappa/2)\Sigma^2\,, \tag{2.62}$$

where $\kappa = [\eta/\lambda][\gamma - \Theta]$ is the fraction of initial DSBs that undergo pairwise damage interaction. Since equations 2.61 and 2.62 hold for both photons and protons and the constants

Θ and κ are not a function of radiation quality, linear quadratic parameters for proton beams can be linked to α_{X} und β_{X} for the respective tissue:

$$\alpha_{\mathrm{P}} = \frac{\Sigma}{\Sigma_{\mathrm{X}}}\left[\alpha_{\mathrm{X}} + 2\frac{\beta_{\mathrm{X}}}{\Sigma_{\mathrm{X}}}(\Sigma\bar{z}_F - \Sigma_{\mathrm{X}}\bar{z}_{F,\mathrm{X}})\right] \quad \text{and} \tag{2.63}$$

$$\beta_{\mathrm{P}} = \left(\frac{\Sigma}{\Sigma_{\mathrm{X}}}\right)^2 \beta_{\mathrm{X}}\,, \tag{2.64}$$

where Σ_{X} and $\bar{z}_{F,\mathrm{X}}$ are DSB yield and frequency mean specific energy for photons, respectively (Frese et al., 2012). By assuming a spherical water target with diameter $l = 5\mu$m for the cell nucleus, $\bar{z}_F$ (and likewise $\bar{z}_{F,\mathrm{X}}$) can be approximated as (Carlson et al., 2008):

$$\bar{z}_F = 0.204 \cdot \frac{LET}{l^2}\left[\frac{\mathrm{keV}}{\mu\mathrm{m}^3}\right]. \tag{2.65}$$

The DSB yields Σ and Σ_{X} can be obtained from an MCDS simulation (Semenenko and Stewart, 2004; Semenenko and Stewart, 2006; Stewart et al., 2011; Hsiao and Stewart, 2008). By incorporating equations 2.63 and 2.64 into the general RBE formula (equation 2.49), the RBE for the RMF model based on X-ray reference radiosensitivity parameters is obtained as (Frese et al., 2012):

$$RBE(\alpha_{\mathrm{X}}/\beta_{\mathrm{X}}, d_{\mathrm{P}}, \Sigma) = \frac{\sqrt{[\alpha_{\mathrm{X}}/\beta_{\mathrm{X}} + 2d_{\mathrm{P}}\frac{\Sigma}{\Sigma_{\mathrm{X}}}]^2 + \frac{8d_{\mathrm{P}}}{\Sigma_{\mathrm{X}}^2}(\bar{z}_F\Sigma^2) - \bar{z}_{F,\mathrm{X}}\Sigma_{\mathrm{X}}\Sigma} - \alpha_{\mathrm{X}}/\beta_{\mathrm{X}}}{2d_{\mathrm{P}}}. \tag{2.66}$$

For polyenergetic beams, equations 2.63 and 2.64 need to integrated against the particle fluence spectrum according to equations 2.47 and 2.48. Kamp and others showed that in this case, α_{X} and β_{X} can be factored out (Kamp, Carlson, and Wilkens, 2017). For a pencil beam with an initial energy E_0, the radio sensitivity parameters at depth z can be written as

$$\alpha_{\mathrm{P}}(E_0, z) = \alpha_{\mathrm{X}}c_1(E_0, z) + \beta_{\mathrm{X}}c_2(E_0, z) \quad \text{and} \tag{2.67}$$

$$\beta_{\mathrm{P}}(E_0, z) = \beta_{\mathrm{X}}(c_1(E_0, z))^2\,, \tag{2.68}$$

where all physical parameters (Φ, S, $\bar{z}_F$, Σ) are included in the pre-calculated, tabulated integrals c_1 and c_2. The latter have the convenient property, that for the superposition of multiple pencil beams, resulting radio sensitivity parameters can be calculated with dose-weighted sums of c_1 and c_2, allowing a fast RBE weighted dose calculation in a matrix multiplication approach (Wilkens and Oelfke, 2004; Wilkens and Oelfke, 2006; Kamp, Carlson, and Wilkens, 2017).

2.4 Treatment planning

Radiotherapy treatment planning is based on 3D imaging modalities such as X-ray computed tomography (CT), magnetic resonance imaging (MRI) and positron emission tomography (PET). These patient images have to serve two purposes in radiotherapy:

- The electron densities (or, in case of proton beams, stopping power ratios) in the patient tissue have to be determined to provide a patient model for dose calculation (*primary imaging*).
- Provide information on patient anatomy, tumor and organ-at-risk (OAR) localization. This information is used in image segmentation, that is, target definition and OAR delineation (*secondary imaging*).

As primary images typically X-ray CT images are used, as the CT values (*Hounsfield units*) are based on X-ray attenuation and are therefore physically linked to electron densities in the tissue. On the contrary, MRI does not contain information about electron densities. There are methods to use MRI as primary imaging and determine electron densities via bulk assignment or deep-learning approaches (see e. g. Edmund and Nyholm, 2017; Neppl et al., 2019; Maspero et al., 2020), however, these where not used in the scope of this work and are therefore not covered any further here. The secondary images are registered to the primary images via rigid, or, if necessary, deformable image registration to aid the delineating physician to define the target volume and contour OARs (Brock et al., 2017). As secondary images any 3D imaging modality may be used, typical modalities include different MRI sequences with or without contrast agent, PET-CT and CT with or without contrast agent. If necessary, also multiple secondary images can be combined. Which secondary imaging modality is used depends on the tumor type and location. For example, for lung tumors often a PET-CT is used as secondary imaging to differentiate between regions of atelectasis (regions of collapsed lung tissue) and vital tumor tissue. On the other hand, brain tumors such as glioblastoma are often delineated with the help of MRI with gadolinium contrast agent as secondary imaging (Wannenmacher, Debus, and Schulz-Ertner, 2013).

2.4.1 Target definition

In external beam photon therapy several target structures are commonly defined (Podgorsak et al., 2005): The gross tumor volume (GTV), which contains the macrospopic tumor volume, that is, the tumor volume which is visible on primary or secondary imaging. The clinical target volume (CTV) contains the GTV and additionally regions of microscopic tumor growth that are not visible on the used images. It is the volume in the patient which is to be irradiated with the prescribed dose in order to achieve the therapeutic goals of the treatment, and it is the task of radiation oncologists to define this region. This step is crucial for treatment outcome, however, it has been shown to be a source of uncertainty in radiotherapy treatment planning (Vinod et al., 2016). The CTV is expanded by a safety

margin to create the planning target volume (PTV). This volume is supposed to ensure a sufficient coverage of the CTV in presence of uncertainties (see also section 2.6). Figure 2.12 illustrates the PTV concept.

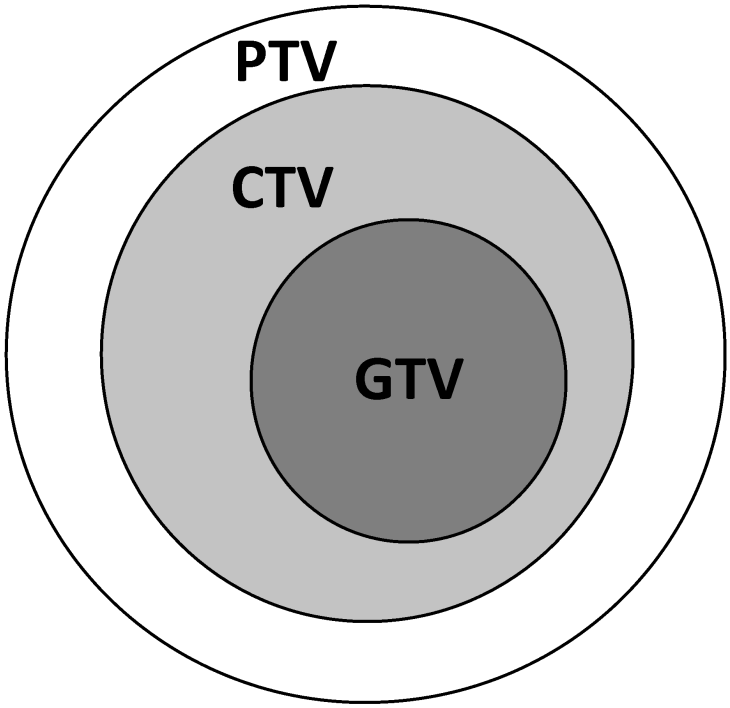

Figure 2.12: Volume definition in radiotherapy. The GTV includes the visible tumor volume, the CTV is the anatomical region which is to be treated and contains additionally regions of microscopic tumor growth. The PTV is an expansion of the CTV and supposed to ensure an adequate coverage of the same in presence of uncertainties.

2.4.2 Photon dose calculation

Before a treatment plan is delivered to a patient, the expected dose distribution in the patient is numerically simulated. Different algorithms for patient dose calculation exist. All have in common that the dose distribution is calculated on a discretized patient model, a grid of *voxels*. A scalar value for the electron density is assigned to each voxel based on the CT Hounsfield units, and a scalar dose value is calculated for each voxel. Since the dose calculation becomes increasingly computationally expensive with finer voxel grids, in clinical practice typically voxel sizes of 2 to 3 mm are used, which is a sufficient resolution for clinical treatment plan evaluation (Schlegel, Karger, and Jäkel, 2018). Since typically the CT resolution differs from the intended dose calculation voxel grid, the density grid used for dose calculation is often obtained through resampling of the CT data. In the following, different dose calculation algorithms for photon treatment plans are briefly described. An overview of dose calculation algorithms for proton beams is given in section 2.4.3.

Pencil beam algorithms

In pencil beam algorithms, the photon beam is described as a superposition of infinitesimal pencil beam kernels in beam direction (Mohan, Chui, and Lidofsky, 1986). The pencil beam kernels are pre-calculated in water. Tissue heterogeneities can be taken into account by scaling the pencil beam with the radiological depth in beam direction, however, lateral heterogeneities are not taken into account. For this reason pencil beam algorithms are extremely fast but have limitations in tissues of high heterogeneity, like for example, lung tissue (Schlegel, Karger, and Jäkel, 2018).

Convolution / superposition algorithms

Convolution / superposition algorithms are analytical methods for dose calculation. The dose deposition in the patient by a photon beam is essentially a two-step process. First, primary photons interact with the medium, which leads to the release of secondary radiation (both charged particles and secondary photons), and to the attenuation of the primary beam. This step is described by TERMA T, which can be calculated from the mass attenuation coefficient μ/ρ and primary energy fluence Ψ_E at position r (Schlegel, Karger, and Jäkel, 2018):

$$T_E(r) = \frac{\mu(E,r)}{\rho(r)} \Psi_E(r)\,. \tag{2.69}$$

The TERMA is not absorbed on the spot but also at other positions in the patient. This second step is described by a point spread kernel which is convoluted with the TERMA:

$$D(s) = \frac{1}{\rho(s)} \iiiint T_E(t)\rho(t)h_E(t,s)d^3t dE\,, \tag{2.70}$$

where the integrand describes the transferred TERMA from point t to point s in a differential energy spectrum dE. The integral corresponds to the energy imparted per unit volume. By dividing it by $\rho(s)$ it is converted to energy imparted per unit mass, the definition of dose. For homogeneous media, h_E depends only on the distance between the points t and s. For practical implementations, pre-calculated kernels in water are used which are then scaled with the radiological distance between the points t and s for heterogeneous media (Mackie et al., 1988). Typically also the energy dependence of TERMA and the kernel h_E is avoided by averaging over a broad energy spectrum. In these approximations, equation 2.70 becomes

$$D(s) = f(s)\frac{1}{\rho(s)} \iiint T(t)\rho(t)h(RD(t-s))d^3t\,, \tag{2.71}$$

where $f(s)$ is a depth-dependent correction factor and RD denotes the radiological distance (Schlegel, Karger, and Jäkel, 2018). Since this approach is still quite computationally expensive when a full patient dose calculation is to be performed ($\sim O(N^7)$, where N is the number of voxels, Schlegel, Karger, and Jäkel, 2018), further approximations have been introduced, such as the collapsed cone convolution algorithm (Ahnesjö, 1989).

Monte Carlo algorithms

Monte Carlo (MC) algorithms model particle transport through a medium explicitly. Using random numbers, interactions along the trajectory of a particle are sampled. In case a large number of particle trajectories is simulated, the resulting dose distribution converges. MC algorithms are commonly acknowledged to be the most accurate method for dose calculation (Verhaegen and Seuntjens, 2003), and they are used for a variety of applications in radiotherapy, for example the calculation of dose kernels for the analytical dose calculation methods described above, full treatment head simulations for beam modeling and also patient dose calculation. In clinical treatment planning, where computational time is crucial, typically special fast MC algorithms like the X-ray voxel Monte Carlo (XVMC) algorithm are used (Fippel, 1999).

2.4.3 Proton dose calculation

Similar to dose calculation for photons, both analytical and stochastic algorithms exist for proton dose calculation.

Pencil beam algorithms

Pencil beam algorithms are based on the approach to model the proton energy loss on its way through a medium and its lateral scattering independently of one another (Newhauser and Zhang, 2015):

$$D(x, y, z) = D(z) \times OAF(x, y, z)\,, \tag{2.72}$$

where z is the depth coordinate, x and y are the lateral coordinates, $D(z)$ is the Bragg curve (i.e., laterally integrated depth-dose) and $OAF(x, y, z)$ is the off-axis-factor and describes the lateral properties of the dose distribution. By using pre-calculated look-up tables in water and the radiological depth for z in heterogeneous media, very fast proton dose calculation can be achieved. Such an algorithm has also been used in the scope of this work and is further described in the appendix to the publication in section 4.2 (Hofmaier et al., 2021). Like for photons, proton pencil beam algorithms have their limitations in the case of large heterogeneity, e.g. in lung tissue.

Monte Carlo algorithms

Also for proton dose calculation Monte Carlo codes are used. Fluktuierende Kaskade (FLUKA) (Ferrari et al., 2005) and Geant4 (Agostinelli et al., 2003) are two of the most common general purpose Monte Carlo codes. In the scope of this work, Geant4 simulated tabulated data for laterally integrated depth-dose curves[2] and the lateral spread of monoenergetic pencil beams in water were used for a fast, GPU-based implementation of a proton pencil beam algorithm.

[2] Courtesy of George Dedes, Faculty of Physics, Department of Medical Physics, LMU Munich

2.4.4 Treatment plan evaluation

Once a treatment plan has been generated, the calculated dose distribution needs to be evaluated in order to decide whether the plan should be delivered to the patient or not. One way to visualize the three-dimensional dose distributions is to show them as an overlay on CT slices of the patient (Schlegel, Karger, and Jäkel, 2018). Another important tool is to reduce the dose distribution to dose volume histograms (DVHs) calculated for the clinically relevant contoured structures (target structures and OARs). With an appropriate dose binning ($0 < d_1 < d_2 < ...$ up to the maximum dose and for sufficient, equidistant steps), DVHs can be calculated by counting the voxels inside a structure which fall into a certain dose bin. By plotting the percentage of voxels against the corresponding dose level, the relative volume of the structure receiving a certain dose level can be visualized (differential DVH):

$$DVH_{\text{diff}}(d_i) = \frac{n_{\text{s}}(d_i)}{n_{\text{s}}}\,, \tag{2.73}$$

where d_i is the i-th dose bin, n_{s} is the number of voxels in the structure and $n_{\text{s}}(d_i)$ is the number of voxels in the structure with a dose value that falls into dose bin d_i. In clinical practice, however, it is usually of more interest to know what relative volume of the structure receives a certain dose *or higher*. For this reason, typically the cumulative DVH is used. It is an integrated form of the differential DVH:

$$DVH_{\text{cum}}(d_i) = \sum_{i}^{\infty} DVH_{\text{diff}}(d_i)\,. \tag{2.74}$$

Examples for differential and cumulative DVHs are shown in figure 2.13.

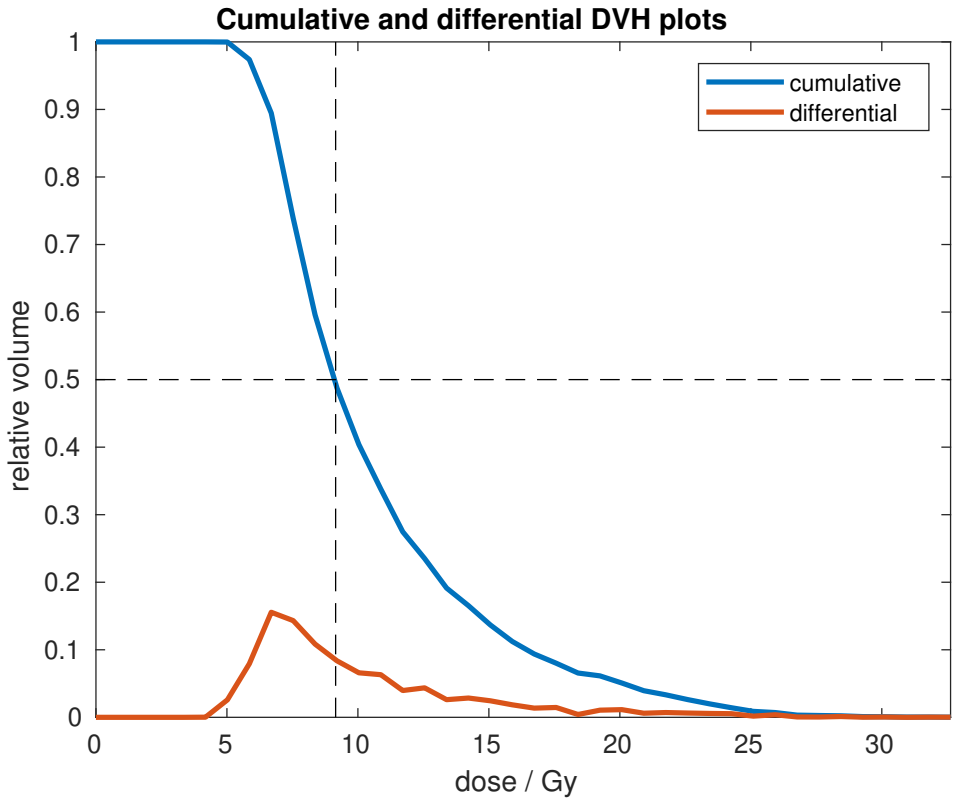

Figure 2.13: Example of cumulative and differential DVH plots. The point on the cumulative DVH marked by the helper lines indicates that 50 % of the structure volume receives 9.2 Gy or more, an information that is not as obvious in the corresponding differential DVH.

2.5 Modern treatment techniques

In this section, some widely used treatment techniques in photon and proton therapy are briefly described.

2.5.1 Three-dimensional conformal radiotherapy

Three-dimensional conformal radiotherapy (3D-CRT) was the first radiotherapy technique to use three-dimensional, voxel-based dose calculation. Target volumes are treated with static fields from multiple directions, whose external contours are matched to the projection of the shape of the target volume in beam direction with MLCs. The photon fluence within the individual fields is nearly uniform (e.g. Bortfeld, 2006; Schlegel, Karger, and Jäkel, 2018).

2.5.2 Dynamic conformal arc therapy

Three-dimensional therapy can also be applied dynamically, this is called dynamic conformal arc therapy (DCAT). The beam is continuously switched on while the gantry rotates around the patient. Meanwhile, the MLC positions are changed dynamically to fit the field to the shape of the target (e.g. Tobler, Watson, and Leavitt, 2002; Schlegel, Karger, and Jäkel, 2018).

2.5.3 Intensity-modulated radiotherapy

With intensity modulated radiotherapy (IMRT) techniques, the conformality of the dose distribution is further improved by modulating the fluence within the fields. Different methods to achieve this goal are available (e.g. Bortfeld, 2006; Schlegel, Karger, and Jäkel, 2018).

Step-and-shoot IMRT

In step-and-shoot IMRT, the fluence is modulated by composing the field via a sequence of smaller fields (called segments), which are irradiated one after another. The beam is switched off in between segments while the MLC moves to the configuration of the following segment. Multiple IMRT fields are delivered from static gantry positions (e. g. Bortfeld, 2006; Schlegel, Karger, and Jäkel, 2018).

Sliding window IMRT

Sliding window IMRT is a dynamic technique to deliver a modulated photon fluence. The collimator leaves move continuously through the field opening while the beam is on. By varying the leaf speed and opening, a modulated fluence pattern is created. Also for this technique the treatment plan is delivered with multiple IMRT fields from static gantry positions (e. g. Bortfeld, 2006; Schlegel, Karger, and Jäkel, 2018).

Volumetric modulated arc therapy

Volumetric modulated arc therapy (VMAT), the most advanced IMRT technique, goes one step further than sliding window IMRT by also moving the gantry around the patient while the beam is on. The dose is delivered to the patient in one or more continuous arcs. This technique has the advantage that the treatment delivery is faster than for step-and-shoot or sliding window IMRT, while employing more beam directions (e. g. Schlegel, Karger, and Jäkel, 2018; Teoh et al., 2011).

2.5.4 Passively scattered proton therapy

A mono-energetic proton beam deposits most of its energy at the depth of the Bragg peak. To cover the target volume with a uniform dose, multiple proton energies have to be superimposed to obtain a SOBP. In passively scattered proton therapy (PSPT), a widely used device to achieve this is the rotating modulation wheel (RMW). As the RMW rotates in the beam path of a nearly mono-energetic proton beam, it interposes different thicknesses of material. The angular coverage of the different thicknesses on the RMW is designed in a way such that a flat SOBP is generated. In addition, scatterers typically consisting of a combination high and low Z materials are used to broaden the beam laterally to achieve an extended field (e.g. Mohan and Grosshans, 2017).

2.5.5 Spot-scanning proton therapy

In spot scanning proton therapy (SSPT), a different approach to shape the desired dose distribution is used. First, the target volume is divided into energy layers of equal water-equivalent path length. Through magnetic steering of a pencil-like, nearly mono-energetic beam, the whole energy layer is scanned. After switching the proton beam energy, the next layer is scanned until the whole target volume is covered with the prescribed dose. SSPT provides a higher number of degrees of freedom than PSPT and also allows for the delivery of intensity modulated proton therapy (IMPT), where the individual beam directions do not necessarily have to deliver a uniform dose to the target (e.g. Mohan and Grosshans, 2017).

2.5.6 Inverse planning

Both IMRT and SSPT employ a high number of degrees of freedom to shape the dose distribution in the patient to optimally cover the target with the prescribed dose while sparing adjacent OARs as much as possible. For previous techniques, such as 3D-CRT and PSPT, *forward* treatment planning was performed. In the case of 3D-CRT, this means that the dosimetrist specifies all beam and collimator angles and the MLC configurations, calculates the dose distribution, and then evaluates the dose distribution, and repeats the whole process until a satisfactory treatment plan is found. Due to the high number of degrees of freedom in IMRT and SSPT, this approach is no longer practical. Instead,

inverse treatment planning is used. In this approach, the dosimetrist specifies optimization goals for dose metrics such as target coverage and allowed OAR exposure, and the optimal treatment plan is found in a numerical optimization (e. g. Schlegel, Karger, and Jäkel, 2018).

2.5.7 Image guided radiotherapy

Image guided radiotherapy (IGRT), in a general sense, refers to the integration of treatment machines with imaging devices to enable the acquisition of patient images immediately before or during treatment (Jaffray, 2012).

IGRT in photon therapy

In photon therapy, images are, among others, aquired using the treatment beam and portal imaging devices, ultrasound imaging and cone beam computed tomography (CBCT) (Van Herk, 2007). More recently, also MRI is used for image guidance (Chin et al., 2020). As of 2022, CBCT imaging devices (the combination of a gantry mounted X-ray tube with a flat-panel detector, Jaffray et al., 2002) are widely used in radiotherapy departments. Typically, CBCT images are used in combination with a robotic table to correct for setup errors: A rigid image registration of the CBCT image to the planning CT provides the six-dimensional (three dimensions for translation, three for rotation), and the table is moved accordingly (Oldham et al., 2005).

IGRT in proton therapy

Due to the unavailability of high energy proton beams (> 250 MeV) for transmission imaging in the early days of proton therapy, 2D orthogonal keV imaging was adopted already in the 1970s in proton therapy. Recently, volumetric imaging became available through in room CT on rails, gantry mounted CBCT, nozzle mounted CBCT, couch mounted CBCT and robotic C-arm CBCT. Like in photon therapy, volumetric images are used for position correction using robotic couches with six degrees of freedom (Landry and Hua, 2018). MRI guidance is not yet available in proton therapy, but it is actively investigated (Hoffmann et al., 2020).

2.5.8 Adaptive radiotherapy

If non-rigid changes to the patient geometry occur, the geometrical agreement between the patient at the actual treatment day and the planning CT deteriorates. Such changes might occur *interfractional* (change in between treatment fractions, e.g. tumor shrinkage, weight loss) or *intrafractional* (change during treatment fractions, e.g. movement of intestinal gas, breathing motion). In these cases, it might no longer be possible to achieve an adequate dose distribution with the current plan despite positional corrections and adaptation of the plan might be necessary. This concept is called adaptive radiotherapy (ART). Plan

adaptation can be performed in between treatment fractions (offline ART), immediately before the treatment (online ART) (Sonke, Aznar, and Rasch, 2019) or potentially even during the treatment (real-time ART) (Keall, Poulsen, and Booth, 2019). Online adaptive approaches that have been recently introduced into the clinical photon therapy routine rely on MRI (Chin et al., 2020). However, online adaptive radiotherapy is offered only by a minority of radiotherapy departments so far.

2.6 Quantitative uncertainties in radiation therapy

In this section, a brief overview over quantitative uncertainties in radiation therapy is given. While setup and motion uncertainty as well as inter-observer variability affect both photon and proton therapy, range and RBE uncertainties are specific sources of uncertainty which do not exist in photon therapy but play an important role in proton therapy. In the scope of this work, a framework for variance-based sensitivity analysis (SA) (see chapter 3 for an introduction of this statistical method) of uncertainties in proton therapy has been implemented (see section 4.2).

2.6.1 Setup and motion uncertainty

In order to deliver a treatment plan to a patient, the patient needs to be aligned to the treatment machine to reproduce the geometry of the planning image. Deviations from the planned patient positioning are called setup errors and do result in deviations between delivered and planned dose distribution. The magnitude of such errors depends on the treatment site (e.g. typically the positioning of the head with a mask system is more reproducible than the positioning of the pelvis using a vacuum mattress) and the used positioning workflow (e.g. setup errors can be considerably reduced if IGRT with volumetric imaging and a six degree of freedom robotic couch is employed). Motion uncertainty refers to changes in the internal anatomy, e.g. drift of the prostate within the body. The magnitude and timescale of this type of error largely depend on the treatment site, for example the mobility of the abdominal organs is larger than the mobility of the brain within the skull, and the drift of the prostate is slower than breathing motion. One way to manage these setup and motion uncertainties is the use of appropriate CTV to PTV margins (Stroom et al., 1999; Van Herk et al., 2000; Van Herk, 2004). These concepts rely on the *static dose cloud approximation*. In this concept, it is assumed, that the shape of the dose distribution with respect to the treatment room is not affected by changes in the patient anatomy and the CTV will always be sufficiently covered with the prescribed dose as long as it stays within the PTV. While this approximation is sufficient for photon treatments, it breaks down for proton therapy.

2.6.2 Range uncertainty

The fact that proton beams have a finite range is their biggest advantage over photon therapy, since it allows to spare healthy tissue distal to the Bragg peak. However, the steep dose fall off at the end of the proton range is also a source of dosimetric uncertainty, since deviations in the proton range prediction may, in the case of an overestimated proton range, lead to underdosage of the target, or, in the case of an underestimation of the proton range, unexpected dose to healthy tissue behind the target. Reasons for range uncertainty include, among others (see Paganetti, 2012b and McGowan, Burnet, and Lomax, 2013 for more details):

- *CT-to-stopping power ratio conversion.* For proton dose calculation on CT images, CT density values need to be converted to proton stopping power ratios relative to water. This process is subject to uncertainty due to image noise and the fact that tissues of different stopping power ratio may correspond to the same CT value. This error can be reduced by using dual energy CT (Wohlfahrt et al., 2017) and could be further reduced by using the proton beam for imaging (Dedes et al., 2019).

- *Range degradation due to multiple Coulomb scattering.* When a proton beam passes through matter, it repeatedly experiences Coulomb scattering, resulting in small direction changes. This introduces a variation in the proton path through the medium; and, in consequence, a degradation of the distal dose fall-off. In cases of high tissue heterogeneity, this degradation is not correctly predicted by analytical dose calculation algorithms (Paganetti, 2012b).

- *Basic physical parameters.* If Monte Carlo algorithms are used instead of analytical ones, the range prediction is still limited by accuracy with which basic parameters such as the mean excitation energy in water and other materials are known (Paganetti, 2012b).

- *Patient anatomy changes.* These changes may result in range errors by changing the density along the beam path, for example through weight loss, tumor shrinkage (e. g. Barker et al., 2004), filling of the paranasal sinus with fluid (e. g. Shusharina et al., 2019), rectal filling (e. g. Adamson and Wu, 2009) and others.

- *Patient setup.* A setup error can lead to a range error, in case it results in density changes in the beam path (McGowan, Burnet, and Lomax, 2013).

As already mentioned above, the static dose cloud approximation is not valid for proton therapy and margin recipes used in photon therapy are not sufficient. Therefore, if margins are used in proton therapy to compensate for both range and setup uncertainty, typically the single field uniform dose (SFUD) concept is employed: beam-specific PTV margins, also compensating for range uncertainty, are used and each proton beam is optimized to deliver a uniform dose to the target (McGowan, Burnet, and Lomax, 2013). More recently, the SFUD concept is abandoned and IMPT plan robustness against uncertainty is incorporated in the optimization itself. In the concept of probabilistic planning, the need for a PTV and explicit margins is eliminated. More information on this can be found in a review by Unkelbach et al., 2018.

2.6.3 RBE uncertainty

In proton therapy, an RBE of 1.1 is commonly assumed. However, the actual RBE is known to increase with LET. For this reason, variable RBE models have been developed, two of which are introduced in section 2.3.2. These models are subject to different types of uncertainties:

- *Biological data.* The biological experiments to investigate the RBE of proton beams include, among others, *in vitro* experiments with cell cultures, *in vivo* animal models and clinical studies. Large uncertainties are present in the known empirical data due to inconsistencies in experimental design, different LET spectra, differences in reference radiation, inconsistencies in the biological assays, and others (Mohan et al., 2017; Paganetti, 2014). Uncertainty is present both in the X-ray reference parameters α_X and β_X of the linear quadratic model and the empirical data for proton RBE. Furthermore, the validity of the linear quadratic model itself has its limitations, e.g. at low fraction doses (McMahon, 2019).

- *Physical parameters.* Since RBE calculations are based on physical quantities such as dose and LET, the physical uncertainties described in the previous section will not only affect the physical dose calculation itself, but also result in an uncertainty of the RBE prediction. In particular in the region of the dose fall-off in the distal part of the SOBP, where the highest RBE values are occurring, uncertainties in dose and LET prediction are high (Mohan et al., 2017).

- *Model-specific uncertainties.* Depending on the used RBE model, parameters particular of the specific model can be considered uncertain, e.g. the assumption of the Wedenberg model for β_P or the DSB induction prediction using MCDS for the RMF model (see section 2.3.2).

2.6.4 Inter-observer variability

The aim of the PTV concept and other robustness approaches in radiotherapy is to achieve an adequate coverage of the CTV in presence of uncertainties (see also section 2.12). However, due to inter observer variability (IOV), the CTV itself is subject to uncertainties. In margin concepts and robust planning approaches, IOV is typically neglected. Since setup and motion uncertainty are reduced through modern techniques such as IGRT, IOV is often seen as one of the largest remaining sources of uncertainty in radiotherapy (Njeh, 2008). The magnitude of IOV can vary significantly depending on the tumor site, experience of the contouring radiation oncologist, image quality and other factors. Including multimodal imaging into the contouring can reduce IOV (Weiss and Hess, 2003).

Chapter 3

Uncertainty and sensitivity analysis

In this work, two studies using the statistical method of global, variance-based sensitivity analysis (SA) to investigate the influence of different types of uncertainty on relative biological effectiveness (RBE)-weighted dose calculations in proton therapy are presented (see sections 4.2 and A.1). In this chapter, an overview over SA methods is given. The advantages of global, variance-based methods compared to other sensitivity analysis methods are briefly discussed and their use is motivated. An efficient way to calculate global, variance-based sensitivity measures, which has also been used in the above mentioned studies, is presented.

3.1 Overview

According to Saltelli et al., 2004, SA can be defined as *"the study of how uncertainty in the output of a model (numerical or otherwise) can be apportioned to different sources of uncertainty in the model input"*, where a "model" can be anything that produces quantitative output Y from a set of input factors $(X_1, ..., X_k)$:

$$Y = f(X_1, ..., X_k)\,, \tag{3.1}$$

where f could be defined in many different forms. For example, it could be a mathematical function that can be written down in closed form, a numerical simulation, or even a neural network, just to name a few examples. Typically SA is carried out together with uncertainty analysis (UA) to quantify the overall uncertainty. Relating to equation 3.1, the questions that SA and UA aim to answer are:

- If the individual uncertainties of the X_i are taken into account, what is the resulting overall uncertainty in Y? *(uncertainty analysis)*
- What is the fraction of the overall uncertainty in Y which is attributable to each of the X_i? *(sensitivity analysis)*

Different methods to tackle these questions exist. In the following section a few of these will be presented and discussed with focus on their limitations.

3.2 Simple method

The simplest way to investigate the influence of a parameter change is to reevaluate function 3.1:

$$\Delta Y_{X_i} = f(X_1^0, ..., X_i^0 + \Delta X_i, ..., X_k^0) - f(X_1^0, ..., X_i^0, ..., X_k^0)\,. \tag{3.2}$$

This approach has the advantage of being easy to implement and fast to execute. However, it has several limitations:

- A relative and normalized sensitivity measure cannot be defined based on equation 3.2.
- The method does not take into account the probability distribution of the X_i. Only a single ΔX_i space is considered, for example a worst-case scenario.
- If f is not monotonic in X_i, the worst-case in the input range does not necessarily correspond to largest error in Y.
- Interactions between multiple input parameters can in principle be evaluated by varying two or more of them simultaneously. If many input parameters are considered, visualization and interpretation of the results can be difficult.

3.3 Analytical method

If an analytical form of the function f in equation 3.1 is known and the error of the X_i can be assumed to be independent from each other and normal distributed with mean values X_i^0 and standard deviation σ_{X_i}, Gaussian error propagation can be applied. A Taylor expansion around the point $(X_1^0, ..., X_k^0)$ is performed:

$$Y_\mathrm{T} = f_\mathrm{T}(X_1^0 + \Delta X_1, ..., X_k^0 + \Delta X_k) \approx f_\mathrm{T}^0 + \sum_{i=1}^{k} \Delta X_i \left[\frac{\partial f}{\partial X_i}\right]_{X_1^0,...,X_k^0}\,, \tag{3.3}$$

with the constant

$$f_\mathrm{T}^0 = f(X_1^0, ..., X_k^0)\,. \tag{3.4}$$

The variance of each of the summation terms on the right hand side of equation 3.3 is

$$V_{X_i} = \sigma_{X_i}^2 \left[\frac{\partial f}{\partial X_i}\right]^2_{X_1^0,...,X_k^0}\,, \tag{3.5}$$

while f_T^0 does not contribute to variance. The overall variance can then be calculated as

$$V_{Y_\mathrm{T}} = \sum_{i=1}^{k} V_{X_i}\,. \tag{3.6}$$

Since the X_i are normal distributed, Y_T will also be normal distributed with mean value f_T^0 and standard deviation (Taylor, 1997):

$$\sigma_{Y_\mathrm{T}} = \sqrt{V_{Y_\mathrm{T}}}\,. \tag{3.7}$$

A sensitivity measure for the fraction of overall variance that can be attributed to input parameter X_i can be defined by normalizing V_{X_i} to the overall variance:

$$S_\mathrm{Gauss} = \frac{V_{X_i}}{V_{Y_\mathrm{T}}}\,. \tag{3.8}$$

This method has several limitations:

- An analytical, differentiable form of f needs to be known.
- The linear approximation needs to be valid within the range of error of the X_i.
- The method does neglect interaction terms between multiple input parameters.

3.4 Global variance-based methods

This section is mostly based on Saltelli et al., 2004, Saltelli et al., 2008 and Saltelli et al., 2010 and aims to give a brief introduction to methods used throughout this work. The idea behind variance-based approaches to SA is to sample all input parameters simultaneously within their respective assumed distributions and decompose the resulting overall variance $V(Y)$. Assuming independent input factors $(X_1, ..., X_k)$, a decomposition of f into terms of increasing dimensionality whose mean is zero is considered (Sobol, 2001):

$$Y = f(X_1, ...X_k) = f_0 + \sum_{i=1}^{k} f_i(X_i) + \sum_{i=1}^{k}\sum_{j>i}^{k} f_{ij}(X_i, X_j) + ... + f_{12...k}(X_1, ..., X_k)\,, \tag{3.9}$$

with

$$\int f_{1...s}(X_1, ..., X_s) dX_p = 0 \tag{3.10}$$

for all $p = 1, ..., s$. Then, all summands in equation 3.9 are orthogonal (Sobol, 2001). Consequently, these terms can be calculated as conditioned expectation values of Y

$$\begin{aligned}
f_0 &= E(Y)\,, && (3.11)\\
f_i &= E(Y|X_i) - E(Y)\,, && (3.12)\\
f_{ij} &= E(Y|X_i, X_j)) - f_i - f_j - f_0\,, && (3.13)\\
f_{ijm} &= E(Y|X_i, X_j, X_m)) - f_{ij} - f_{jm} - f_{im} - f_i - f_j - f_m - f_0 && (3.14)
\end{aligned}$$

and so on (Saltelli et al., 2008). The expectation value is $E(Y|X_i)$ is hereby calculated over all possible values of all input factors except X_i, which is kept fixed. By calculating the variances

$$V_i = V(f_i(X_i)), \tag{3.15}$$
$$V_{ij} = V(f_{ij}(X_i, X_j)), \tag{3.16}$$
$$V_{ijm} = V(f_{ijm}(X_i, X_j, X_m)) \tag{3.17}$$

and so on, the overall variance $V(Y)$ of the model f can be decomposed as

$$V(Y) = \sum_i V_i + \sum_i \sum_{j>i} V_{ij} + ... + V_{12...k}\,. \tag{3.18}$$

Sensitivity indices are defined by normalizing to the overall variance

$$S_i = \frac{V_i}{V(Y)}, \tag{3.19}$$
$$S_{ij} = \frac{V_{ij}}{V(Y)}, \tag{3.20}$$
$$S_{ijm} = \frac{V_{ijm}}{V(Y)} \tag{3.21}$$

and so on. Due to the normalization to the overall variance, the sensitivity indices are normalized to 1:

$$\sum_i S_i + \sum_i \sum_{j>i} S_{ij} + ... + S_{12...k} = 1\,. \tag{3.22}$$

Since the number of different sensitivity indices increases exponentially with k (their total number is $2^k - 1$), the so called the *total effects* are introduced. These are defined as the sum of all sensitivity indices of all orders that contain input i:

$$ST_i = S_i + \sum_{j \neq i} S_{ij} + ... + S_{12...k}\,, \tag{3.23}$$

which reduces the number of sensitivity indices reported to characterize a model with k input factors to $2k$ ($S_1 ... S_k$ and $ST_1 ... ST_k$).

Interpretation of the sensitivity indices

First order and total effects allow for an intuitive interpretation: S_i is the mean fraction by which the overall variance could be reduced if the input factor X_i could be fixed anywhere in its range. ST_i is the mean fraction of the overall variance that would remain if all input factors but X_i could be fixed anywhere in their range. The total effect indices also allow identifying non-influential input parameters (that is, input parameters that do not

contribute to the overall uncertainty). The necessary and sufficient condition for the input parameter X_i being non-influential is

$$ST_i = 0\,. \tag{3.24}$$

Note that $S_i = 0$ is necessary but not sufficient for X_i to be a non-influential parameter, since X_i might contribute to overall uncertainty through higher-order terms. On the contrary, if

$$S_i = 1\,, \tag{3.25}$$

this means that X_i is the only influential input factor while all other input factors are non-influential ($ST_j = 0$ for all $j \neq i$). In case the model is *additive*, that is, it does not include interactions between the input factors, the equation

$$\sum_j S_j = 1 \tag{3.26}$$

holds and all the higher order terms are zero, implying:

$$S_i = ST_i\,. \tag{3.27}$$

There is an efficient method to calculate S_i and ST_i directly without explicitly calculating all interaction terms, which will be described in the next section.

Numerical estimation of first order and total effects

A Monte Carlo method for calculation of S_i and ST_i has been introduced in an article by Saltelli, 2002 and is also described in the books *Sensitivity Analysis in Practice: A Guide to Assessing Scientific Models* (Saltelli et al., 2004) and *Global Sensitivity Analysis. The Primer* (Saltelli et al., 2008). A numerical improvement of this method, which has also been used in the scope of this work, has been presented in Saltelli et al., 2010.

First, a sample of $(N, 2k)$ random numbers is generated, where k is the number of input factors and N is the Monte Carlo sample size which has to be chosen large enough to ensure convergence, typically in the range from a few hundred to a few thousand. The convergence can be accelerated by sampling from quasi-random, low discrepancy sequences instead of pseudo-random sequences, an approach that has also been used in the scope of this work. In the study presented in section 4.2, Sobol sequences were used (Sobol, 1967; Sobol et al., 1992). Two independent matrices A and B with a size of $N \times k$ are obtained from the sample:

$$A = \begin{bmatrix} x_1^{(1)} & x_2^{(1)} & \dots & x_i^{(1)} & \dots & x_k^{(1)} \\ x_1^{(2)} & x_2^{(2)} & \dots & x_i^{(2)} & \dots & x_k^{(2)} \\ \dots & \dots & \dots & \dots & \dots & \dots \\ x_1^{(N-1)} & x_2^{(N-1)} & \dots & x_i^{(N-1)} & \dots & x_k^{(N-1)} \\ x_1^{(N)} & x_2^{(N)} & \dots & x_i^{(N)} & \dots & x_k^{(N)} \end{bmatrix} \tag{3.28}$$

and

$$B = \begin{bmatrix} x_{k+1}^{(1)} & x_{k+2}^{(1)} & \dots & x_{k+i}^{(1)} & \dots & x_{2k}^{(1)} \\ x_{k+1}^{(2)} & x_{k+2}^{(2)} & \dots & x_{k+i}^{(2)} & \dots & x_{2k}^{(2)} \\ \dots & \dots & \dots & \dots & \dots & \dots \\ x_{k+1}^{(N-1)} & x_{k+2}^{(N-1)} & \dots & x_{k+i}^{(N-1)} & \dots & x_{2k}^{(N-1)} \\ x_{k+1}^{(N)} & x_{k+2}^{(N)} & \dots & x_{k+i}^{(N)} & \dots & x_{2k}^{(N)} \end{bmatrix} . \tag{3.29}$$

For each of the input factors, a matrix C_i is constructed, which consists of all columns of matrix A, except for the i-th column, which is taken from B:

$$C_i = \begin{bmatrix} x_1^{(1)} & x_2^{(1)} & \dots & x_{k+i}^{(1)} & \dots & x_k^{(1)} \\ x_1^{(2)} & x_2^{(2)} & \dots & x_{k+i}^{(2)} & \dots & x_k^{(2)} \\ \dots & \dots & \dots & \dots & \dots & \dots \\ x_1^{(N-1)} & x_2^{(N-1)} & \dots & x_{k+i}^{(N-1)} & \dots & x_k^{(N-1)} \\ x_1^{(N)} & x_2^{(N)} & \dots & x_{k+i}^{(N)} & \dots & x_k^{(N)} \end{bmatrix} . \tag{3.30}$$

Then the model f is evaluated for all three matrices. Each of the rows of the matrices corresponds to one model run, so there are N runs for each matrix. Since there are k matrices C_1,C_2,...,C_k and the two matrices A and B, the total number of necessary model runs is

$$N_{\text{runs}} = N(k+2) . \tag{3.31}$$

The model evaluations result in output vectors of length N for each of the matrices:

$$y_A = f(A) , \tag{3.32}$$

$$y_B = f(B) \quad \text{and} \tag{3.33}$$

$$y_{C_i} = f(C_i) . \tag{3.34}$$

With these output vectors, first order and total effects are estimated as

$$S_i = \frac{\frac{1}{N}\sum_j^N y_B^{(j)} \cdot \left(y_{C_i}^{(j)} - y_A^{(j)} \right)}{V(Y)} \quad \text{and} \tag{3.35}$$

$$ST_i = \frac{\frac{1}{2N}\sum_j^N \left(y_{C_i}^{(j)} - y_A^{(j)} \right)^2}{V(Y)} . \tag{3.36}$$

where the total variance $V(Y)$ is numerically estimated from y_A and y_B (Saltelli et al., 2010). A drawback of the method is that being a Monte Carlo method it requires a relatively large number of model evaluations and can therefore become computationally

expensive. For example, for a typical value of $N = 1024$ and a model with $k = 10$ input factors, according to equation 3.31 the number of necessary model evaluations would be

$$N_{\text{runs}} = N(k+2) \approx 1.22 \cdot 10^4 \,. \tag{3.37}$$

Which would, for example, result in a calculation time of approximately 20 minutes if one model evaluation took 0.1 seconds. On the other hand, this method can overcome several limitations discussed for the methods described above:

- Relative and normalized measures for sensitivity are defined in a systematic and comprehensive way.
- There are no requirements for the form of model f, which can be considered a "black box" in this approach. Since only the output Y is analyzed, the variance-based approach can be applied to all kinds of quantitative models (among others e.g. a numerical simulation, an optimization result or a neural network).
- The Monte Carlo approach is able to handle arbitrary (both continuous and discrete) probability distributions for the input parameters.
- Since all k parameters are sampled simultaneously, the whole k-dimensional input space is explored (*global* method that also takes into account interaction terms).

Chapter 4

Studies

4.1 Paper 1: Multi-criterial patient positioning based on dose recalculation on scatter-corrected CBCT images

Reprinted with permission from "Multi-criterial patient positioning based on dose recalculation on scatter-corrected CBCT images." by Hofmaier J, Haehnle J, Kurz C, Landry G, Maihoefer C, Schüttrumpf L, Süss P, Teichert K, Söhn M, Spahr N, Brachmann C, Weiler F, Thieke C, Küfer KH, Belka C, Parodi K and Kamp F; Radiotherapy and Oncology (2017). Dec;125(3):464-469 doi:10.1016/j.radonc.2017.09.020

Radiotherapy and Oncology 125 (2017) 464–469

Contents lists available at ScienceDirect

Radiotherapy and Oncology

journal homepage: www.thegreenjournal.com

Dose guided positioning

Multi-criterial patient positioning based on dose recalculation on scatter-corrected CBCT images

Jan Hofmaier [a,c,*], Jonas Haehnle [b], Christopher Kurz [a,c], Guillaume Landry [c], Cornelius Maihoefer [a,g], Lars Schüttrumpf [a,g], Philipp Süss [b], Katrin Teichert [b], Matthias Söhn [a], Nadine Spahr [d], Christoph Brachmann [e], Florian Weiler [e], Christian Thieke [a], Karl-Heinz Küfer [b], Claus Belka [a,f,g], Katia Parodi [c], Florian Kamp [a]

[a] *Department of Radiation Oncology, University Hospital, LMU Munich, Munich;* [b] *Fraunhofer Institute for Industrial Mathematics ITWM, Kaiserslautern;* [c] *Department of Medical Physics, Faculty of Physics, Ludwig–Maximilians-Universität München, Munich;* [d] *Fraunhofer Institute for Medical Image Computing MEVIS, Lübeck;* [e] *Fraunhofer Institute for Medical Image Computing MEVIS, Bremen;* [f] *German Cancer Consortium (DKTK), Munich; and* [g] *Clinical Cooperation Group Personalized Radiotherapy in Head and Neck Cancer, Helmholtz Zentrum München, Munich, Germany*

ARTICLE INFO

Article history:
Received 30 May 2017
Received in revised form 18 September 2017
Accepted 19 September 2017
Available online 12 October 2017
This work has been partially presented at the ESTRO 36 meeting in Vienna, May 2017.

Keywords:
Isocenter correction
Scatter correction
CBCT
Dose guided positioning

ABSTRACT

Background and purpose: Our aim was to evaluate the feasibility and potential advantages of dose guided patient positioning based on dose recalculation on scatter corrected cone beam computed tomography (CBCT) image data.

Material and methods: A scatter correction approach has been employed to enable dose calculations on CBCT images. A recently proposed tool for interactive multicriterial dose-guided patient positioning which uses interpolation between pre-calculated sample doses has been utilized. The workflow was retrospectively evaluated for two head and neck patients with a total of 39 CBCTs. Dose–volume histogram (DVH) parameters were compared to rigid image registration based isocenter corrections (clinical scenario).

Results: The accuracy of the dose interpolation was found sufficient, facilitating the implementation of dose guided patient positioning. Compared to the clinical scenario, the mean dose to the parotid glands could be improved for 2 out of 5 fractions for the first patient while other parameters were preserved. For the second patient, the mean coverage over all fractions of the high dose PTV could be improved by 4%. For this patient, coverage improvements had to be traded against organ at risk (OAR) doses within their clinical tolerance limits.

Conclusions: Dose guided patient positioning using in-room CBCT data is feasible and offers increased control over target coverage and doses to OARs.

In modern intensity-modulated radiotherapy (IMRT), a treatment plan is optimized in order to cover the target volume with the prescribed dose while optimally sparing adjacent healthy structures. The optimization takes the individual patient geometry into account, which is imaged before the beginning of the treatment course by a computed tomography (CT) scan. To ensure that the delivered dose is in agreement with the calculated dose in the treatment planning system, the patient needs to be positioned and aligned to the treatment unit in a reproducible and accurate way. Typically, this is performed using in-room imaging equipment such as cone-beam computed tomography (CBCT) [1]. A rigid registration with 6 or 3 degrees of freedom between planning CT (pCT) and CBCT is performed, and the patient table is moved accordingly to account for set-up errors [2]. The rigid registration is typically based on anatomical landmarks close to the tumor (e.g. bones) or implanted fiducial markers [3]. However, during the course of treatment, considerable non-rigid changes may occur, such as tumor shrinkage or weight-loss [4,5]. In this case, the actual dose distribution might differ substantially from the one calculated on the pCT [6], and determining the clinically favorable rigid isocenter correction is not obvious. This could possibly result in both a clinically relevant underdosage of the tumor and an overdosage of relevant organs at risk (OAR), thus risking reduced tumor control and increasing toxicity. Due to the high scatter contribution, CT numbers of CBCTs are not sufficiently accurate for dose calculation. However, lately there has been a lot of progress in intensity correction strategies for CBCT to enable photon and proton dose calculation on these images [7–9], and it seems therefore reasonable to

* Corresponding author at: Klinikum der Universität München, Klinik und Poliklinik für Strahlentherapie und Radioonkologie, Marchioninistraße 15, D-81377 München, Germany.
E-mail address: jan.hofmaier@med.uni-muenchen.de (J. Hofmaier).

https://doi.org/10.1016/j.radonc.2017.09.020
0167-8140/

base the isocenter correction on a dose recalculation on the image of the day rather than on the clinically used rigid image registration between pCT and CBCT. This has first been suggested for proton therapy [6,10]. Recently, an interactive, multicriterial approach to dose-guided patient positioning has been presented and evaluated for re-planning CTs of head and neck (H&N) and prostate patients treated with photon IMRT [11]. In the present work, we evaluate the potential of the method using dose recalculation on scatter corrected CBCT (scCBCT) images.

Methods

Fig. 1 gives an overview of the overall workflow. The three main features are a scatter correction method for CBCTs, a propagation of contours from the pCT to the scCBCT and an interactive, pareto optimal dose-based isocenter correction, balancing dose–volume histogram (DVH) objectives. The workflow has been evaluated for two H&N patient cases with a total of 39 CBCTs.

Imaging and rigid registration based isocenter correction

The pCTs were acquired with a Toshiba Acquilion CT scanner. The CBCT images were acquired with the integrated scanner in the Elekta Axesse system. The clinical rigid registration between CBCT and pCT was applied using a bony match in the Elekta XVI software. Isocenter position corrections were restricted to 3 degrees of freedom, i.e. only translational corrections.

Scatter correction and CBCT contouring

After the CBCT acquisition, a scatter correction of the CBCT is performed. Our implementation of scatter correction closely followed [8,9]. Virtual CTs (vCTs) obtained by deformable image registration (DIR) are used as a prior to estimate the scatter contribution in the CBCT projections.

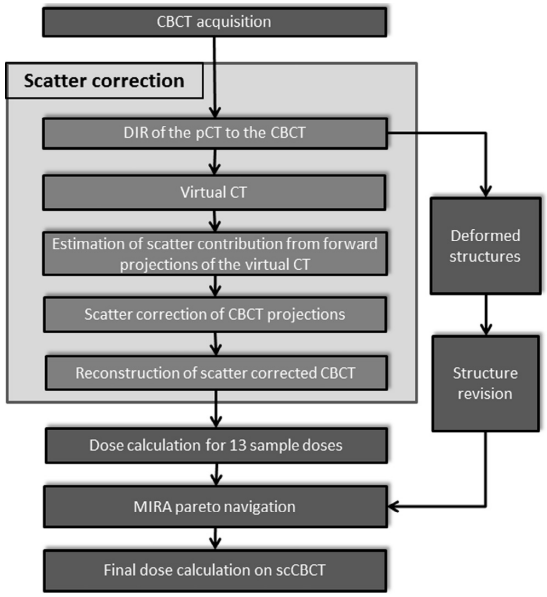

Fig. 1. Overview of the applied dose guided positioning workflow. The deformable image registration is performed both for the scatter correction and to obtain deformed contours, which are used as a starting point for the contouring of the CBCTs. To avoid any interpolation errors in the evaluation, a final dose calculation was added once a satisfying isocenter correction was found.

The workflow of the scatter correction is as follows (as also highlighted in Fig. 1):

1. DIR of the pCT to the CBCT to obtain a vCT "of the day". The vector field is also used to propagate the contours from the pCT to the vCT.
2. Forward projection of the vCT according to the cone beam geometry.
3. Application of a correction factor (CF) to the CBCT projections to match the intensities to the vCT forward projections. Following [8], we used CF = 25.6.
4. Estimation of scatter by subtraction of the vCT forward projections from the CBCT projections and a smoothing operation (a 2D median filter with 25-by-25 pixels width, followed by a Gaussian filter of 1.5 pixels standard deviation).
5. Subtraction of scatter from the CBCT projections.
6. Reconstruction of the scCBCT.

The advantage of this approach over using the vCT itself for dose calculation is that it is insensitive to small errors in the DIR and contrast of the CBCT is not altered by the scatter-correction [7,8].

In our workflow, a variational approach is used for DIR and aims for image similarity and deformation regularity. Image similarity is measured by Normalized Gradient Fields (NGF) [12] and deformation regularity is modeled by curvature regularization [13]. The resulting optimization problem is solved in a discretize-then-optimize scheme using a quasi-Newton L-BFGS optimizer.

Due to the limited field of view (FOV) of the CBCT and hence the scCBCT, the corresponding regions of the pCT outside the FOV were stitched to the scCBCT. This was necessary to account for beam attenuation when irradiating through the shoulders of the patients, which were not covered by the CBCT FOV. A comparison of the different types of CTs can be found in Supplemental Fig. 1.

The propagated contours of organs at risk (OARs) were adapted by a trained clinical expert. The PTV contours were adapted by senior physicians.

Dose calculation and interpolation

The dose distribution of the original clinical plan on the scCBCT was calculated using a Monte Carlo (MC) algorithm on a $3 \times 3 \times 3$ mm^3 dose grid. The used dose engine was MCverify v2.44, a scriptable research version of the same algorithm used in Elekta Monaco 5.1. Clinical treatment plans of the evaluated patients were delivered with an Elekta Axesse LINAC. For every scCBCT, the dose was calculated for 13 sample isocenter positions: the central position, based on a rigid alignment of the CBCT to the pCT, and shifts of ±3 mm and ±6 mm along every axis. For each fraction, the clinically delivered plan was used for the dose calculations on the scCBCTs (also in case of a clinical re-planning). As described in more detail in [11], linear combinations of the sample dose distributions are used to estimate dose distributions in a continuous space of possible isocenter shifts. To avoid errors in our evaluation of DVH parameters, which might be introduced by inaccuracies in the dose interpolation, also a final dose calculation was performed once a satisfying isocenter correction was found. Reported DVH parameters were therefore always determined from a dose calculation for the final isocenter position without interpolation involved. Interpolated doses were only used during the multicriterial optimization described below to find that isocenter position. The interpolation accuracy was evaluated by interpolating dose cubes for random 3D isocenter shifts within the accessible range of the interpolation and comparing them to the respective forward calculation using a 2% dose difference criterion and a 2%/2 mm gamma criterion. 100 random shifts for each scCBCT of patient 1 and 30 random shifts for each scCBCT of patient 2 were evaluated.

Multicriterial interactive radiotherapy assistant

The multicriterial interactive radiotherapy assistant (MIRA) is a research treatment planning system for IMRT. The interface gives the user the possibility to browse pareto-optimal plan candidates interactively [14–16]. The recently implemented multicriterial isocenter optimization in MIRA has been described in [11]. Pre-calculated sample doses for a set of isocenter shifts and interpolation between them are used to enable interactive navigation in real-time. The multicriterial approach is DVH based, meaning that the user doesn't manipulate the isocenter directly. Instead, the tool offers sliders corresponding to DVH deviation cost functions for the structures of interest. These cost functions compare a DVH on the pCT with the respective DVH on the scCBCT for a possible isocenter position. For OARs, they are defined as follows:

$$q_{OAR}(d^{c,scCBCT}, d^{pCT}) = \sqrt{\sum_{i=0}^{100} \max\left(0, D_i^{c,scCBCT} - D_i^{pCT}\right)^2}$$

where c denotes a possible isocenter shift, d denotes the respective dose distributions on pCT and scCBCT and $D_{0\ldots100}$ are the dose quantiles of the corresponding cumulative DVH. It is a one-sided cost function, which penalizes any of the D_i^{scCBCT} being larger than the respective D_i^{pCT}.

For target structures the cost function is defined analogously:

$$q_{Target}(d^{c,scCBCT}, d^{pCT}) = \sqrt{\sum_{i=0}^{49} \max\left(0, D_i^{c,scCBCT} - D_i^{pCT}\right)^2 + \sum_{i=50}^{100} \max\left(0, D_i^{pCT} - D_i^{c,scCBCT}\right)^2}$$

This cost function penalizes any increase of the dose quantiles $D_{0\ldots49}$ and any decrease of the dose quantiles $D_{50\ldots100}$, therefore it maximizes target coverage while still minimizing overdosage.

The multicriterial optimization restricts the accessible isocenters to the subset of pareto-optimal solutions – therefore, no DVH objective can be improved without worsening another. When the user manipulates the sliders, he immediately gets the result of this trade-off. The tool is up to now restricted to translational shifts in 3 dimensions and does not yet support rotational adjustments.

Application to patient data

Clinical datasets of two patients who had received curative-intended radiotherapy for head and neck cancer have been retrospectively evaluated. Their characteristics are shown in Table 1. Patients were positioned in supine position and immobilized with a thermoplastic mask. The clinical step-and-shoot IMRT (ssIMRT) treatment plan for patient 1 was generated with Hyperion V2.42, a research version of the treatment planning system (TPS) Elekta Monaco. For validation, the plan was re-calculated in the TPS Oncentra Masterplan. The clinical VMAT plans for patient 2 were optimized in Monaco itself. Both patients were treated with a simultaneous integrated boost (SIB) concept. All calculated values for particular fractions were scaled to the total plan dose. Our evaluation focused on the trade-off between PTV coverage and dose to the parotid glands, which is of interest due to its association with xerostomia [17]. For patient 2, the left parotid gland was inside of the target volume, therefore, only the parotid gland on the right hand side was considered. For the other OARs, it was always assured that the clinical constraints in Table 2 were met for the final dose guided isocenter shift.

Results

Interpolation accuracy

The median pass-rate for the 2% dose difference criterion over all 1520 calculated shifts was 92.8% (range 86.8–100.0%). Failing points were located predominantly at the patient surface, where the interpolation cannot be accurate. For a 2%/2 mm gamma criterion, median pass-rate was 99.0% (range 96.6–100.0%).

DVH parameters

Table 3 shows mean values of relevant DVH parameters for both patients. For patient 1 the mean dose to both parotid glands could be improved compared to the clinical, rigid registration based shifts (31.0 to 30.2 Gy and 26.4 to 25.3 Gy, respectively). Other parameters were unchanged, except for a very small decrease in target coverage for the boost PTVs. Fig. 2 shows DVHs for one exemplary fraction of this patient. In this particular fraction, the mean dose to the left parotid gland improved from 30.6 to 26.1 Gy, the mean dose to the right parotid showed a small increase from 30.2 to 30.6 Gy. The coverage of the high dose PTV with the 95% isodose was slightly decreased. Isodose lines of a representative dose distribution for this patient can be found in Supplemental Fig. 2.

Fig. 3 shows the change of DVH parameters for patient 2 over time. For this patient, the mean coverage of the high dose PTV with the 95% isodose improved from 77% to 81% using dose guided positioning. The dose to the spared right parotid gland remained stable for this patient (mean value over all fractions of D_{mean} was 26.1 Gy both for the rigid registration based and dose guided isocenter corrections). A decrease in coverage occurs both for clinical as well as dose guided shifts around fraction 7, when large anatomical changes occurred due to necrotic degradation of the tumor (this is also visible in the plot of PTV size, Fig. 3f). This patient underwent offline-re-planning during his treatment course. The coverage is restored in fraction 18, when the original plan is replaced by the new one. After re-planning, the dose guided shifts perform better in preserving the coverage than the rigid image registration based shifts. However, improvements in coverage had to be traded against additional dose to the spinal cord (Fig. 2d and Table 3: the mean $D_{2\%}$ increased from 37.4 to 38.3) and the brain stem (Table 3: mean $D_{2\%}$ increased from 40.1 to 41.2).

The average Euclidean distance between the clinical and the optimized isocenter corrections for all available fractions was 1.8 mm (range 0.8–3.2 mm) for patient 1 and 2.0 mm (range 0.0–3.5 mm) for patient 2. A detailed plot of the difference between rigid registration based and dose guided isocenters can be found in Supplemental Fig. 3.

Discussion

A recently proposed tool for dose guided patient positioning has been evaluated with in-room CBCT imaging data for the first time. The dose interpolation necessary for a fast multicriterial optimiza-

Table 1
Evaluated patient cases.

No.	Prescription	Site of primary tumor	Technique	Sparing of parotid glands	Fractions with CBCT	Clinical re-planning	Primary tumor PTV volume change
1	66 Gy/60 Gy/54 Gy	Oral cavity	ssIMRT	bilateral	5/30	No	Stable (+4.8%)
2	70 Gy/56 Gy	Left cheek	VMAT	Only right side	34/35	Yes, after 17 fractions	Pronounced (−54.8%)

Table 2
OAR constraints that were always respected in the final dose isocenter shift.

Structure	Constraint
Spinal cord	$D_{2\%} \leq 45$ Gy
Optic chiasm	$D_{2\%} \leq 54$ Gy
Optic nerve	$D_{2\%} \leq 54$ Gy
Brain stem	$D_{2\%} \leq 54$ Gy

tion based on 13 sample isocenter positions was found accurate. In principle, the accuracy of the interpolation could be further improved with the inclusion of further sample points. A final forward calculation of the plan with the chosen isocenter shift was added for verification. A scatter correction approach was used to facilitate dose calculation on CBCTs. This approach was up to now only used and validated for proton dose calculation. A proton range agreement of less than 2 mm for more than 80% of the BEV profiles and a gamma passrate of more than 96% using a 2%/2 mm criterion for the proton dose distribution was reported comparing scCBCT and conventional CT [9]. Since photons are less prone to CT number inaccuracies than protons, it is safe to use scCBCTs for photon dose calculations. The validation in [9] was performed using the Elekta XVI system, which was also used in our study. Applying the scatter correction approach using other CBCT scanners might require a similar initial validation first. Also in [9], it was shown that the scatter correction approach can overcome small inaccuracies in the DIR, due to the smoothing function [8] applied to the scatter map. Due to the limited FOV of the scCBCT, regions of the pCT outside of the scCBCT FOV were stitched to the scCBCT to account for beam attenuation in these regions. The dosimetric uncertainty introduced by this approach is expected to be minimal, since head and neck are always fully covered by the FOV and in this region only the treatment table and patient immobilization devices are added, which are not subject to changes. In addition, the shoulders are added below the neck. Due to the treatment being coplanar, the uncertainty which might be introduced by an unprecise stitching affects only the lowest slices of the low dose PTV (lymphatic drainage area).

For patient 1, the mean dose to the parotid glands was improved compared to the clinical standard rigid anatomy based isocenter corrections, while other DVH parameters could be kept stable, except for a very small reduction in target coverage for the boost PTVs. For patient 2, coverage improvements had to be traded against OAR doses. For the affected OARs, spinal cord and brain stem, DVH parameters could be kept well below clinical constraints. The large maximum doses for the high dose PTV during the first days of treatment (Fig. 3e) are explained by the fact that this tumor was exulcerated and its volume had still increased by 8% between pCT (day 0 in Fig. 3f) and the first treatment fraction, which was delivered 7 days later. In order to improve the target coverage at the surface of the tumor, the clinical treatment plan had high fluence tangentially to the tumor surface. The "auto flash margin" feature in Monaco, which opens the fields at the PTV borders when these are located at the patient surface, had then extended the high fluence regions beyond the patient surface. The tumor had grown into these fluence regions. In this particular case, this rather non-robust plan had been accepted, since the dose elevation only affected the exulcerated tumor and no healthy tissue was at risk. After the tumor volume decreased because parts of the tumor disappeared due to necrotic degradation around fraction 7, the maximum dose decreased to normal and the coverage of the PTV70 deteriorated. This also shows the limitations of this workflow: In the presence of such major anatomical changes, both rigid registration based and dose guided approach fail to restore an acceptable coverage of the target. At this time, clearly an adaptive online re-planning would have been beneficial. However, after the offline re-planning on day 18, the dose guided positioning approach performs considerably better than the rigid registration based approach in preserving target coverage in the presence of the smaller volume changes occurring during the rest of the treatment course.

In the presented implementation the isocenter corrections are limited to 3 translational degrees of freedom (d.o.f). In principle, the approach might be extended to 6 d.o.f. in future implementations, allowing also for rotational adjustments.

A drawback of the presented approach compared to the rigid registration based alignment is the need for contours on the daily image. In the presented workflow, contours are propagated from the pCT to the scCBCT using DIR. However, these contours need to be revised by physicians before a clinical decision can be made using them. In a future online implementation of the workflow, this will probably be the most time-consuming step. Besides the time needed for the contour adaption and their review also intra and inter observer variability remains a challenge for all studies and clinical workflows that require (re-) contouring. Other steps of the workflow, which in our current implementation take a few minutes (DIR and scatter correction) or an hour (the MC dose calculations), might be brought down to a few minutes altogether using fast GPU implementations, e.g. [18,19], on a single integrated platform. In such an environment, the dose calculation might also run in the background while the contours are revised to further speed up the process. Since the interactive step to find the optimal shift is very fast (less than a minute) we estimate a time benefit compared to a full adaptive re-planning, as has been discussed in [11]. Under this assumption, the dose guided approach might also have its place in integrated systems alongside with online re-planning capability. Such a workflow might look as follows:

- Acquire CBCT images
- Perform scatter correction
- Stitch pCT regions outside of scCBCT FOV to scCBCT

Table 3
Mean values of DVH statistics over all available fractions. The bold values indicate improvements compared to the rigid registration based shifts. For patient 1, the dose to the parotid glands was improved. For patient 2, the target coverage of the high dose PTV was increased.

Parameter	High dose PTV $V_{95\%}$	Intermediate dose PTV $V_{95\%}$	Low dose PTV $V_{95\%}$	Parotid R D_{mean} [Gy]	Parotid L D_{mean} [Gy]	Spinal Cord $D_{2\%}$ [Gy]	Brain stem $D_{2\%}$ [Gy]	Opt. nerve l $D_{2\%}$ [Gy]	Opt. nerve r $D_{2\%}$ [Gy]	Opt. chiasm $D_{2\%}$ [Gy]
Patient 1										
-planning CT	90.7%	90.7%	91.0%	29.8	29.8	36.7				
-rigid reg.	90.4%	89.5%	91.6%	**31.0**	**26.4**	38.6	n. a.	n. a.	n.a.	n.a.
-dose guided	89.9%	89.1%	91.4%	**30.2**	**25.3**	38.1				
Patient 2										
-planning CT	90%		97%	25.9	57.5	36.2	39.7	48.1	29.9	39.8
-rigid reg.	**77%**	n.a.	96%	26.1	57.7	37.4	40.1	49.2	29.4	39.2
-dose guided	**81%**		96%	26.1	58.1	38.3	41.2	49.2	30.0	39.8

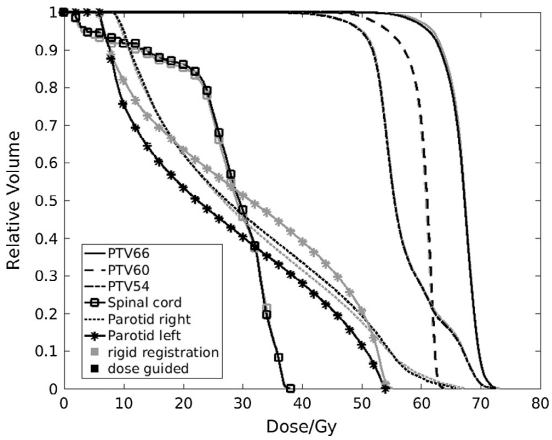

Fig. 2. DVHs for one fraction of patient 1. The DVHs are scaled to the total plan dose. Compared to the rigid image registration based shifts, the dose guided approach showed comparable DVHs for PTV66Gy, PTV60Gy, PTV54Gy and the spinal cord. The dose to the left parotid gland was decreased; the dose to the right parotid gland showed a small increase.

- Revise contours
- Perform dose guided alignment
- In case a satisfactory isocenter correction is found, apply treatment
- If not, trigger adaptive re-planning (including revision/approval of the adapted plan and QA)

Dose guided positioning could have the potential to reduce the mean time per fraction compared to a daily re-planning, while still preserving DVH objectives. In clinical practice, one might also think about monitoring DVH parameters during the fractions only using dose guided positioning, and making the decision for adaptive re-planning before the next fraction as soon as parameters of interest come close to pre-defined thresholds. Methods to identify patients who benefit the most from adaptive radiotherapy might also help guiding decision making [20,21]. As already discussed in [11], a potential advantage of the proposed workflow over a full adaptive re-planning is that no new plan is created, which would always require the approval of a senior physician and a physicist. The approach has therefore the potential to reduce the required manpower during patient treatment. Furthermore, there is no need for quality assurance of a new plan. To date it is unclear how many full re-plannings for H&N patients are actually beneficial, but there

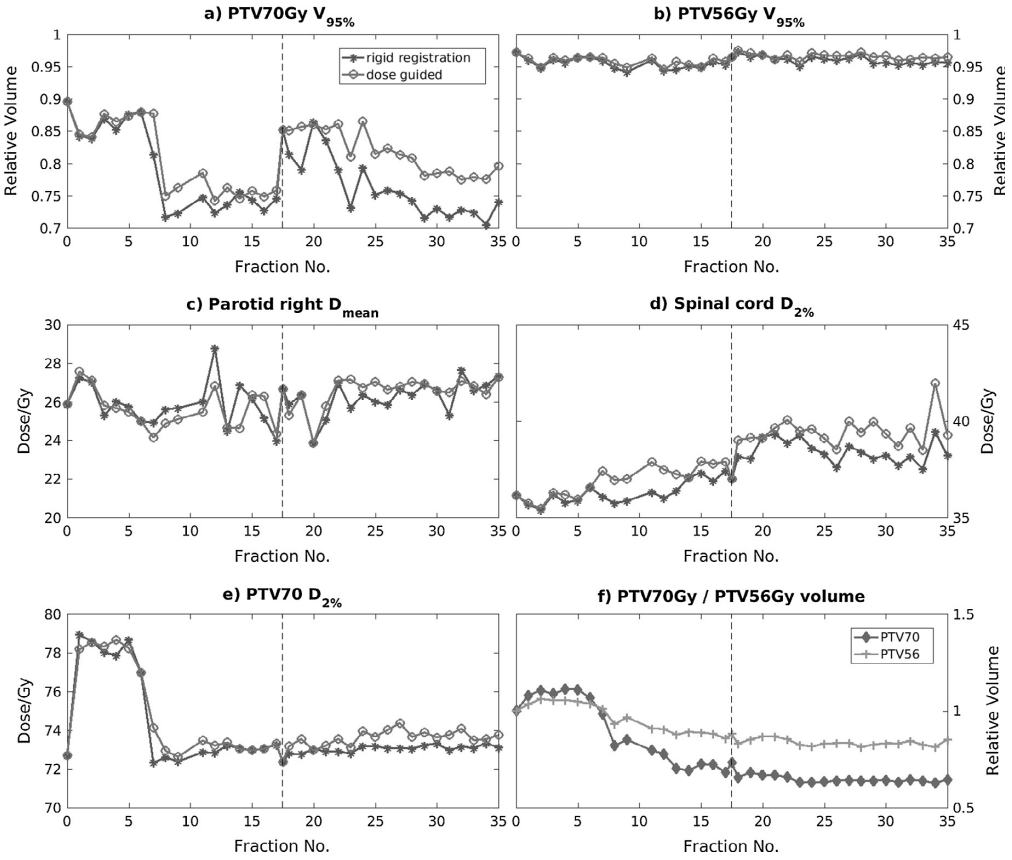

Fig. 3. Evolution over time of selected DVH parameters (a–e) and PTV volumes (f) for patient 2. The calculated values are the values for the corresponding fraction and on scCBCT, scaled to the total plan dose. The dashed vertical line indicates the re-planning. The planning CT is included as day 0, the re-planning CT is included between day 17 and day 18. PTV volumes are normalized to their volumes on the planning CT.

are data suggesting that for many patients only 3 adaptive re-plannings might be sufficient [22].

In principle, dose guided positioning might also be used in integrated systems with magnetic resonance imaging (MRI) capability, given that an accurate dose calculation on MRI is available, e.g. on synthetic CTs [23,24].

An important issue regarding a potential clinical implementation of the approach is the overall uncertainty of the DVH parameters, which is generally difficult to address. While the scatter correction approach can overcome uncertainties in the pCT to CBCT DIR and has been successfully validated in [9], and the influence of the pCT stitching to the uncertainty is considered negligible, as discussed above, the uncertainty of the updated contours depends strongly on the individual physician re-contouring the scCBCTs. Inter- and intra-observer variability in the contouring is difficult to quantify and hence to include into the evaluation of feasibility studies. Since all scCBCTs for a patient in this study have been contoured by the same physician, it is only influenced by the – potentially smaller – intra-observer variability. However, since the potential improvements of 3–5% have to be set in proportion to the overall uncertainty, this issue currently remains a major hurdle for a clinical implementation of the approach, as it is the case for any procedure with the need for updated contours.

An aspect which was not evaluated in the present feasibility study is the potential for margin reductions. In this study the coverage of the PTV was evaluated. In case a CTV can be determined with sufficient confidence based on the image of the day, it might be more plausible to use the CTV coverage in the multicriterial optimization, or a reduced PTV with smaller margins than the ones used in rigid registration based workflows.

Conclusion

Dose guided patient positioning using scatter corrected CBCT images is feasible and offers increased control over target coverage and OAR dose compared to the clinical anatomy-based registration approach. In an integrated workflow alongside with adaptive re-planning, the approach could help reducing the number of full re-plannings and therefore reduce treatment time and workload compared to a daily re-planning scenario.

Conflict of interest

The authors declare no conflict of interest.

Acknowledgements

DFG cluster of excellence: Munich-Centre for Advanced Photonics (MAP) EXC 158.

BMBF-SPARTA (grant number 01IB31001).

Markus Alber for providing the scriptable MC dose engine MCverify.

Larissa Ermoschkin for contouring organs-at-risk.

Appendix A. Supplementary data

Supplementary data associated with this article can be found, in the online version, at https://doi.org/10.1016/j.radonc.2017.09.020.

References

[1] Jaffray DA, Siewerdsen JH, Wong JW, Martinez AA. Flat-panel cone-beam computed tomography for image-guided radiation therapy. Int J Radiat Oncol Biol Phys 2002;53:1337–49. https://doi.org/10.1016/S0360-3016(02)02884-5.

[2] Oldham M, Létourneau D, Watt L, Hugo G, Yan D, Lockman D, et al. Cone-beam-CT guided radiation therapy: A model for on-line application. Radiother Oncol 2005;75:1–8. https://doi.org/10.1016/j.radonc.2005.03.026.

[3] Shi W, Li JG, Zlotecki RA, Yeung A, Newlin H, Palta J, et al. Evaluation of kV cone-beam CT performance for prostate IGRT. Am J Clin Oncol 2011;34:16–21. https://doi.org/10.1097/COC.0b013e3181d26b1a.

[4] Barker JL, Garden AS, Ang KK, O'Daniel JC, Wang H, Court LE, et al. Quantification of volumetric and geometric changes occurring during fractionated radiotherapy for head-and-neck cancer using an integrated CT/linear accelerator system. Int J Radiat Oncol Biol Phys 2004;59:960–70. https://doi.org/10.1016/j.ijrobp.2003.12.024.

[5] Müller BS, Duma MN, Kampfer S, Nill S, Oelfke U, Geinitz H, et al. Impact of interfractional changes in head and neck cancer patients on the delivered dose in intensity modulated radiotherapy with protons and photons. Phys Medica 2015;31:266–72. https://doi.org/10.1016/j.ejmp.2015.02.007.

[6] Cheung J, Aubry JF, Yom SS, Gottschalk AR, Celi JC, Pouliot J. Dose recalculation and the Dose-Guided Radiation Therapy (DGRT) process using megavoltage cone-beam CT. Int J Radiat Oncol Biol Phys 2009;74:583–92. https://doi.org/10.1016/j.ijrobp.2008.12.034.

[7] Niu T, Sun M, Star-Lack J, Gao H, Fan Q, Zhu L. Shading correction for on-board cone-beam CT in radiation therapy using planning MDCT images. Med Phys 2010;37:5395–406. https://doi.org/10.1118/1.3483260.

[8] Park Y, Sharp GC, Phillips J, Winey BA. Proton dose calculation on scatter-corrected CBCT image: feasibility study for adaptive proton therapy. Med Phys 2015;42:4449–59. https://doi.org/10.1118/1.4923179.

[9] Kurz C, Kamp F, Park Y-K, Zöllner C, Rit S, Hansen D, et al. Investigating deformable image registration and scatter correction for CBCT-based dose calculation in adaptive IMPT. Med Phys 2016;43:5635–46. https://doi.org/10.1118/1.4962933.

[10] Cheung JP, Park PC, Court LE, Ronald Zhu X, Kudchadker RJ, Frank SJ, et al. A novel dose-based positioning method for CT image-guided proton therapy. Med Phys 2013;40:51714. https://doi.org/10.1118/1.4801910.

[11] Haehnle J, Süss P, Landry G, Teichert K, Hille L, Hofmaier J, et al. A novel method for interactive multi-objective dose-guided patient positioning. Phys Med Biol 2017;62. https://doi.org/10.1088/1361-6560/62/1/165.

[12] Haber E, Modersitzki J. Intensity gradient based registration and fusion of multi-modal images. Methods Inf Med 2007;46:292–9. https://doi.org/10.1160/ME9046.

[13] Fischer B, Modersitzki J. Curvature based image registration. J Math Imaging Vis 2003;18:81–5. https://doi.org/10.1023/A:1021897212261.

[14] Thieke C, Küfer KH, Monz M, Scherrer A, Alonso F, Oelfke U, et al. A new concept for interactive radiotherapy planning with multicriteria optimization: first clinical evaluation. Radiother Oncol 2007;85:292–8. https://doi.org/10.1016/j.radonc.2007.06.020.

[15] Craft DL, Hong TS, Shih HA, Bortfeld TR. Improved planning time and plan quality through multicriteria optimization for intensity-modulated radiotherapy. Int J Radiat Oncol Biol Phys 2012;82:83–90. https://doi.org/10.1016/j.ijrobp.2010.12.007.

[16] Kierkels RGJ, Visser R, Bijl HP, Langendijk JA, van't Veld AA, Steenbakkers RJHM, et al. Multicriteria optimization enables less experienced planners to efficiently produce high quality treatment plans in head and neck cancer radiotherapy. Radiat Oncol 2015;10:87. https://doi.org/10.1186/s13014-015-0385-9.

[17] Thor M, Owosho AA, Clark HD, Oh JH, Riaz N, Hovan A, et al. Internal and external generalizability of temporal dose response relationships for xerostomia following IMRT for head and neck cancer. Radiother Oncol 2016;122:200–6. https://doi.org/10.1016/j.radonc.2016.11.005.

[18] Gu X, Pan H, Liang Y, Castillo R, Yang D, Choi D, et al. Implementation and evaluation of various demons deformable image registration algorithms on a GPU. Phys Med Biol 2010;55:207–19. https://doi.org/10.1088/0031-9155/55/1/012.

[19] Gu X, Choi D, Men C, Pan H, Majumdar A, Jiang SB. GPU-based ultra-fast dose calculation using a finite size pencil beam model. Phys Med Biol 2009;54:6287. https://doi.org/10.1088/0031-9155/54/20/017.

[20] Brown E, Owen R, Harden F, Mengersen K, Oestreich K, Houghton W, et al. Predicting the need for adaptive radiotherapy in head and neck cancer. Radiother Oncol 2015;116:57–63. https://doi.org/10.1016/j.radonc.2015.06.025.

[21] Brouwer CL, Steenbakkers RJHM, van der Schaaf A, Sopacua CTC, van Dijk LV, Kierkels RGJ, et al. Selection of head and neck cancer patients for adaptive radiotherapy to decrease xerostomia. Radiother Oncol 2016;120:36–40. https://doi.org/10.1016/j.radonc.2016.05.025.

[22] Zhang P, Simon A, Rigaud B, Castelli J, Ospina Arango JD, Nassef M, et al. Optimal adaptive IMRT strategy to spare the parotid glands in oropharyngeal cancer. Radiother Oncol 2016;120:41–7. https://doi.org/10.1016/j.radonc.2016.05.028.

[23] Guerreiro F, Burgos N, Dunlop A, Wong K, Petkar I, Nutting C, et al. Evaluation of a multi-atlas CT synthesis approach for MRI-only radiotherapy treatment planning. Phys Medica 2017;35:7–17. https://doi.org/10.1016/j.ejmp.2017.02.017.

[24] Farjam R, Tyagi N, Veeraraghavan H, Apte A, Zakian K, Hunt MA, et al. Multi-atlas approach with local registration goodness weighting for MRI-based electron density mapping of head and neck anatomy. Med Phys 2017;44:3706–17. https://doi.org/10.1002/mp.12303.

4.2 Paper 2: Variance-based sensitivity analysis for uncertainties in proton therapy: A framework to assess the effect of simultaneous uncertainties in range, positioning, and RBE model predictions on RBE-weighted dose distributions

Reprinted with permission from "Variance-based sensitivity analysis for uncertainties in proton therapy: Effect of simultaneous uncertainties in range, positioning and RBE model predictions on RBE-weighted dose distributions." by Hofmaier J, Dedes G, Carlson DJ, Parodi K, Belka C and Kamp F; Medical Physics (2021). 48(2):805-818. doi:10.1002/mp.14596

Variance-based sensitivity analysis for uncertainties in proton therapy: A framework to assess the effect of simultaneous uncertainties in range, positioning, and RBE model predictions on RBE-weighted dose distributions

Jan Hofmaier[a)]
Department of Radiation Oncology, University Hospital, LMU Munich, Munich 81377, Germany

George Dedes
Department of Medical Physics, Faculty of Physics, LMU Munich, Garching b. Munich 85748, Germany

David J. Carlson
Department of Radiation Oncology, University of Pennsylvania, Philadelphia, PA 19104, USA

Katia Parodi
Department of Medical Physics, Faculty of Physics, LMU Munich, Garching b. Munich 85748, Germany

Claus Belka
Department of Radiation Oncology, University Hospital, LMU Munich, Munich 81377, Germany
German Cancer Consortium (DKTK), Munich 81377, Germany

Florian Kamp
Department of Radiation Oncology, University Hospital, LMU Munich, Munich 81377, Germany

(Received 12 August 2019; revised 20 October 2020; accepted for publication 11 November 2020; published 18 December 2020)

Purpose: Treatment plans in proton therapy are more sensitive to uncertainties than in conventional photon therapy. In addition to setup uncertainties, proton therapy is affected by uncertainties in proton range and relative biological effectiveness (RBE). While to date a constant RBE of 1.1 is commonly assumed, the actual RBE is known to increase toward the distal end of the spread-out Bragg peak. Several models for variable RBE predictions exist. We present a framework to evaluate the combined impact and interactions of setup, range, and RBE uncertainties in a comprehensive, variance-based sensitivity analysis (SA).

Material and methods: The variance-based SA requires a large number (10^4–10^5) of RBE-weighted dose (RWD) calculations. Based on a particle therapy extension of the research treatment planning system CERR we implemented a fast, graphics processing unit (GPU) accelerated pencil beam modeling of patient and range shifts. For RBE predictions, two biological models were included: The mechanistic repair-misrepair-fixation (RMF) model and the phenomenological Wedenberg model. All input parameters (patient position, proton range, RBE model parameters) are sampled simultaneously within their assumed probability distributions. Statistical formalisms rank the input parameters according to their influence on the overall uncertainty of RBE-weighted dose–volume histogram (RW-DVH) quantiles and the RWD in every voxel, resulting in relative, normalized sensitivity indices (S = 0: noninfluential input, S = 1: only influential input). Results are visualized as RW-DVHs with error bars and sensitivity maps.

Results and conclusions: The approach is demonstrated for two representative brain tumor cases and a prostate case. The full SA including $\sim 3 \times 10^4$ RWD calculations took 39, 11, and 55 min, respectively. Range uncertainty was an important contribution to overall uncertainty at the distal end of the target, while the relatively smaller uncertainty inside the target was governed by biological uncertainties. Consequently, the uncertainty of the RW-DVH quantile D_{98} for the target was governed by range uncertainty while the uncertainty of the mean target dose was dominated by the biological parameters. The SA framework is a powerful and flexible tool to evaluate uncertainty in RWD distributions and DVH quantiles, taking into account physical and RBE uncertainties and their interactions. The additional information might help to prioritize research efforts to reduce physical and RBE uncertainties and could also have implications for future approaches to biologically robust planning and optimization. © *2020 The Authors. Medical Physics published by Wiley Periodicals LLC on behalf of American Association of Physicists in Medicine.* [https://doi.org/10.1002/mp.14596]

Key words: proton therapy, range uncertainty, relative biological effectiveness, sensitivity analysis, uncertainty analysis

1. INTRODUCTION

Treatment plans in proton therapy are more prone to uncertainties than in photon therapy. In addition to setup uncertainty, which is also relevant for treatment with photons, proton beams are affected by range uncertainties. Furthermore, the relative biological effectiveness (RBE) of proton beams needs to be taken into account and additional sources of uncertainty are introduced through the conversion of physical to RBE-weighted dose (RWD). Since uncertainties in the actually delivered RWD may give rise to unexpected normal tissue toxicities or local treatment failure and may impede the intercomparability of different radiation modalities (photons, protons, heavier ions) in clinical studies, a well-founded understanding of the magnitude of the overall uncertainty and the impact and interactions of the different sources of uncertainty is crucial. To enable the comparison of different planning strategies (e.g., beam arrangements) with regard to these quantities, a systematic way to estimate them for an individual treatment plan is desirable. While there are many studies assessing the impact of physical[1–4] or biological uncertainties,[5–7] no method for the systematic assessment of the combined impact and interactions of setup, range, and biological uncertainties has been presented so far. When multiple sources of uncertainty are combined, the analysis is typically restricted to range and motion.[8,9] A possible way to deal with these uncertainties in intensity-modulated proton therapy (IMPT) is robust optimization. Up to now, robustness approaches are also mostly restricted to setup and range uncertainties and do not explicitly consider biological modeling. If at all, linear energy transfer (LET) is considered as a surrogate of biological effect.[10,11] Therefore, a better understanding of uncertainty in biological modeling in combination with setup and range uncertainties is needed to enable biologically robust planning. Furthermore, quantifying the relative impact of setup, range and RBE uncertainty on the overall uncertainty of clinically relevant dose metrics could help to prioritize research efforts aiming at reducing the individual uncertainties and improve cost-effectiveness in radiotherapy. The technique of global, variance-based sensitivity analysis (SA) is a method to evaluate the influence of the uncertainty in various input factors on the output of a quantitative model.[12] Compared to local methods, such as derivative-based approaches, regression analysis, or the isolated treatment of the different input factors (one factor at a time approaches), this technique has the advantage of exploring the entire input space by varying all input factors simultaneously, which allows to take into account also interactions between multiple input factors.[13] While the alternative techniques mentioned have their limitations in the case of nonlinear models, global, variance-based SA is a model-independent approach and is applicable for any probability distribution of the input factors. In the field of medical physics, this technique has so far only been applied to RBE modeling of carbon ion therapy, excluding range and setup uncertainties[14,15] and to nuclear medicine, in order to assess the impact of interpatient variability on organ dose estimates.[16] In this feasibility study, we present a framework to apply the technique of global, variance-based SA to uncertainties in proton therapy, explicitly modeling RBE, range, and setup errors.

2. MATERIALS AND METHODS

2.A. Global variance-based sensitivity analysis

Global variance-based SA is a method to estimate the relative influence of the k input factors $X=(x_1,x_2\cdots,x_k)$ on the output Y of a model f:

$$Y=f(X) \tag{1}$$

The function f can be decomposed into terms of increasing dimensionality whose mean is zero, that is[17]

$$f=f_0+\sum_{l}^{k}f_l(x_l)+\sum_{l=1}^{k}\sum_{m>l}^{k}f_{lm}(x_l,x_m)+\ldots+f_{12\ldots k}(x_1,x_2,\ldots,x_k) \tag{2}$$

where for all $p=1,\ldots,s$

$$\int f_{1\ldots s}(x_1,\ldots,x_s)dx_p=0 \tag{3}$$

Sobol proved that then all summands in equation (2) are orthogonal.[17] The variance in Y can be decomposed[12]

$$V(Y)=\sum_{l=1}^{k}V_l+\sum_{l=1}^{k}\sum_{m>l}^{k}V_{lm}+\ldots+V_{1,\ldots,k} \tag{4}$$

where

$$V_l=V(f_l)=V[E(Y|X_l)] \tag{5}$$

The expectation value $E(Y|X_l)$ is hereby calculated over all possible values of all input factors except for X_l, which is kept fixed. The higher order terms are

$$V_{lm}=V(f_{lm})=V[E(Y|X_l,X_m)]-V_l-V_m \tag{6}$$

and so on. The first- and second-order sensitivity indices introduced by Sobol' are defined as[12]:

$$S_l=\frac{V_l}{V(Y)} \tag{7}$$

$$S_{lm}=\frac{V_{lm}}{V(Y)} \tag{8}$$

Higher order terms are defined in an analogous fashion. Monte Carlo estimates for all sensitivity indices can be calculated without the need to know an explicit form of f or any of the terms in the expansion in Eq. (2). Due to the normalization to the overall variance, the Sobol' indices are normalized to 1. Since the number of sensitivity indices is (2^k-1) for k input factors, making interpretation of the results very difficult, total effects ST_l are introduced.[18] For the input factor l they are defined as the sum of all terms of any order containing l:

$$ST_l = S_l + \sum_{m \neq l}^{k} S_{lm} + \ldots + S_{1,\ldots,k} \tag{9}$$

when only first order and total effects for each input factor are considered, the number of indices is reduced to $2k$. First order and total effects allow for an intuitive interpretation: S_l is the average fraction by which the overall variance would be reduced if input factor l could be fixed anywhere in its range, ST_l is the average fraction of the overall variance that would remain if all input factors except for l could be fixed within their respective range. $ST_l = 0$ is the necessary and sufficient condition for input l being noninfluential. By examining the difference, $(ST_l - S_l)$, the impact of interaction terms involving input factor l can be characterized. If $(ST_l - S_l) = 0$, interactions with input factor l do not contribute to overall variance.

Saltelli[19] proposed an efficient method for direct Monte Carlo calculation of S_l and ST_l, without the need to calculate all the interaction terms, which has also been used in this paper.

In this approach, S_l and S_{Tl} are estimated via:

$$S_l = \frac{\frac{1}{N}\sum_{m=1}^{N} f(B)_m \cdot \left[f\left(A^{(l)}\right)_m - f(A)_m\right]}{V(Y)} \tag{10}$$

$$S_{Tl} = \frac{\frac{1}{2N}\sum_{m=1}^{N} \left[f(A)_m - f\left(A^{(l)}\right)_m\right]^2}{V(Y)} \tag{11}$$

where A and B are independently sampled input matrices of N input vectors (size:$N \times k$). The matrix $A^{(l)}$ is equal to matrix A, except for column l, which is taken from B. $(A)_m$ and $(B)_m$ are the m-th rows of A and B, respectively. The total number of model evaluations in this approach is $N \cdot (k+2)$. N has to be chosen sufficiently large for Eqs. (10) and (11) to converge.

A faster convergence of Eqs. (10) and (11) is achieved when the input parameters are sampled from quasi-random, low-discrepancy sequences.[19] In our implementation, we used the Sobol' sequence[20,21] as suggested by Saltelli.

In our application of the concept, the model f will correspond to an RWD distribution calculation including a calculation of RBE-weighted dose volume histograms (RW-DVHs), the input vector X will contain isocenter shifts in three spatial dimensions, relative and absolute range shifts as well as biological model parameters. The output Y will include the dose in every voxel and RW-DVH quantiles for structures of interest. Since for the variance-based SA the model needs to be evaluated approximately 10^4–10^5 times, a fast RWD calculation for any set of X from the input space is required. To achieve this, a GPU-based RWD calculation was implemented based on a particle extension of the research treatment planning system CERR.[22–26] To model the physical uncertainties, the following approximations were made: The proton beams were assumed to be nondivergent, and patient deformations and rotations were excluded. Range uncertainty was modeled as a relative and an absolute range shift, which was applied to all spots of the same beam equally. A detailed description of the implementation can be found in Appendices A and B.

In clinical routine, a constant RBE of 1.1 is commonly assumed. However, there is evidence from *in vitro* experiments that RBE is dependent on dose, biological endpoint, and proton energy and there is an ongoing debate if the current clinical practice needs to be revised.[5–7,27,28] For variable RBE prediction, two biological models are currently implemented: the mechanistic repair-misrepair-fixation (RMF) model,[29,30] which uses double strand break (DSB) yields from a Monte Carlo Damage simulation (MCDS)[31] and the phenomenological Wedenberg model.[32] Both models provide a method to calculate radiosensitivity parameters of the linear quadratic (LQ) model, α_P and β_P and have the advantage that they can be executed very fast for changed model and x-ray reference radiosensitivity parameters. For the RMF model, the DSB yield Σ and the x-ray reference parameters α_X/β_X were treated as uncertain; details on the implementation can be found in Appendix C.1. For the Wedenberg model, x-ray reference parameters α_X/β_X, the fit parameter q and the model assumption $\beta_P = \beta_X$ were treated as uncertain. Details on the implementation can be found in Appendix C.2.

2.B. Application to patient cases

The framework was applied to two brain tumor patient cases. The evaluation of an additional prostate case can be found in the supplementary material S1. In both brain tumor cases the clinical target volume (CTV) was overlapping with the optic nerve and in close proximity to the brain stem. For patient 1, the CTV partially overlapped with the optic chiasm while for patient 2 the chiasm was almost completely within the CTV. The CTV of patient 1 had a larger volume with a size of 15.2 cm^3, for patient 2 it was 4.7 cm^3. Planning target volumes were created using an isotropic CTV-to-PTV margin of 3 mm. The plan for patient 1 consisted of two PBS beams from 60° and 135°, the plan for patient 2 of two opposing PBS beams from 90° and 270°. Both plans were optimized for a fraction RWD of 1.8 Gy (RBE), where a constant RBE of 1.1 was assumed. The total prescribed RWD was 54 Gy (RBE) in both cases. In the plan optimization, the total $D_{2\%}$ for adjacent and overlapping OARs (chiasm, optic nerves, brain stem) was constrained to be smaller or equal to 54 Gy (RBE). In each plan, the two beams were optimized independently to deliver a homogeneous dose distribution to the target (single field uniform dose (SFUD) concept). Sensitivity analyses of the resulting plans were performed using the RMF and the Wedenberg model. All input parameter uncertainties were assumed to follow normal distributions truncated to two standard deviations (σ). The following σ were used:

- *1* mm *for patient shifts in X, Y, and Z direction*[33]
- *3% for relative range uncertainty*[1] (R_{rel})
- *1* mm *absolute range uncertainty*[1] $(R1_{abs}$, $R2_{abs}$ *for beam numbers 1,2,...)*

- *10% for the x-ray reference radiosensitivity parameters*(α_X/β_X)
- *15% for the parameterq of the Wedenberg model*[32]
- *10% for*β_P *in the Wedenberg model*
- *5% for the DSB yield* Σ *used in the RMF model*

These assumptions are not definitive and might differ between tumor sites (e.g., in the abdomen a larger setup error than 1 mm might be adequate) or CT acquisition (e.g., in case a dual-energy CT is used for stopping power determination a smaller relative range uncertainty might be reasonable[34]). To model a possible higher uncertainty in the x-ray reference sensitivity parameters in organs at risk (e. g., the chiasm), an additional calculation was performed where α_X/β_X was assumed to be uniformly distributed over the interval 1.5 to 10 Gy. All other input uncertainties remained unchanged. For the CTV and the chiasm, the overall uncertainty of all RW-DVH quantiles was visualized by plotting the RW-DVH with its respective 95% and 68% confidence intervals. For selected quantiles of (CTV $D_{98\%}$, CTV $D_{50\%}$, brain stem $D_{2\%}$, optic nerve $D_{2\%}$, and chiasm $D_{2\%}$), first order and total effect sensitivity indices were calculated. Additionally, the first-order sensitivity for the RBE-weighted dose was calculated on a voxelwise basis and visualized as sensitivity map.

To demonstrate the application of the framework to a prostate case, an additional evaluation of a such a plan can be found in supplementary material S1.

3. RESULTS

A fast modeling of patient shifts, range shifts and changes in biological parameters was implemented which allows the calculation of RWD distributions for arbitrary sets of these input parameters from the input space. The simultaneous variation of all input parameters allows to model interactions of different sources of uncertainty and to perform a global, variance-based SA. Here the results for the two brain tumor cases are shown, the results for the prostate case can be found in the supplementary material S1.

On a computer with 16 CPU cores (Intel Xeon E5-2690 @ 2.90 GHz), 192 GB RAM and two Nvidia Tesla K80 GPUs the full SA including $\sim 3 \times 10^4$ RWD calculations was performed in 39 min for patient 1 and 11 min for patient 2.

Figure 1 shows the convergence of the first-order indices and total effects for selected DVH quantiles, a representative voxel at the center of the PTV and a representative voxel in the high LET region for patient 1. N refers to the number of rows of the input matrices used for the Saltelli estimator for S_i and ST_i described above, the actual number of RWD calculations performed is $N \cdot (k+2)$, with the number of input factors k.

3.A. DVH quantiles

Figures 2 and 3 show the RW-DVH of the CTV and the chiasm for patients 1 and 2, respectively. The proton treatment plan was optimized on 1.8 Gy(RBE) in tumor assuming a constant RBE of 1.1. Then the SA was performed with both biological models assuming a spatially constant $\alpha_X/\beta_X = 2$ Gy ($\alpha_X = 0.1$ Gy^{-1} and $\beta_X = 0.05$ Gy^{-2}).[35] For each model, the treatment plans were recalculated $\sim 3 \times 10^4$ times, randomly varying patient position, proton range and RBE model parameters within their assumed uncertainties. To quantify the overall uncertainty, 95% and 68% confidence intervals were calculated empirically from the resulting RW-DVHs and visualized in Figs. 2 and 3. As expected, a higher RBE than 1.1 is predicted for both biological models. The same calculation was in addition also applied to an RWD calculation assuming a constant RBE of 1.1., including only range and setup uncertainties. The resulting RW-DVH is plotted for comparison. For both patients, a larger overall uncertainty was observed for the variable RBE models with their respective uncertainties included. For example, the expectation value for the mean RWD to the CTV for patient 1 was $2.04^{+0.19}_{-0.19}$ Gy(RBE), $2.03^{+0.14}_{-0.14}$ Gy(RBE) and $1.77^{+0.04}_{-0.11}$ Gy (RBE) for the RMF model, the Wedenberg model and a constant RBE of 1.1, respectively (the reported ranges are the 95% confidence intervals.). For patient 2, the mean RWD to the CTV was $2.01^{+0.21}_{-0.22}$ Gy(RBE), $2.00^{+0.16}_{-0.17}$ Gy(RBE) and $1.75^{+0.04}_{-0.14}$ Gy(RBE) for the RMF model, the Wedenberg model and a constant RBE of 1.1, respectively. For the chiasm, the D_2 for patient 1 was $2.23^{+0.23}_{-0.23}$ Gy(RBE) and $2.17^{+0.18}_{-0.18}$ for the RMF model and the Wedenberg model, respectively, when an $\alpha_X/\beta_X = 2$ Gy with a standard deviation of 10% was assumed. In the calculation with the large α_X/β_X variation it was $2.09^{+0.28}_{-0.23}$ Gy(RBE) (RMF) and $1.98^{+0.28}_{-0.20}$ Gy(RBE) (Wedenberg). For patient 2, a chiasm D_2 of $2.12^{+0.25}_{-0.24}$ Gy(RBE) and $2.09^{+0.19}_{-0.17}$ Gy(RBE) was observed for RMF and Wedenberg, respectively, when an $\alpha_X/\beta_X = 2$ Gy with a standard deviation of 10% was assumed. $2.01^{+0.26}_{-0.24}$ Gy(RBE) (RMF) and $1.93^{+0.24}_{-0.16}$ Gy(RBE) (Wedenberg) was found for the D_2 in the calculation with the large α_X/β_X variation.

For selected clinically relevant RW-DVH quantiles, the confidence intervals in Figs. 2 and 3 are broken down to the impact of the different uncertainties in terms of S_l and ST_l in Fig. 4. All plots show results of the calculation with $\alpha_X/\beta_X = 2$ Gy and a standard deviation of 10%. SA results are color-coded for both patients and both RBE models. For most quantiles, the differences between the S_l and ST_l are small, indicating a low impact of interaction terms on the overall uncertainty. For range uncertainty, however, interactions often do play a role. For example, for the D_2 of the right optic nerve for patient 2 [Figs. 4(c) and 4(d)] ST_l is considerably larger than S_l both for the relative range uncertainty (R_{rel}) for both biological models ($ST_{R_{rel}} = 0.56, S_{R_{rel}} = 0.26$ for the RMF model and $ST_{R_{rel}} = 0.54, S_{R_{rel}} = 0.28$ for the Wedenberg model, respectively) and for shifts in Y and Z direction ($S_Y = 0.03, S_Z = 0.18, ST_Y = 0.25, ST_Z = 0.45$ for the RMF model and $S_Y = 0.07, S_Z = 0.20, ST_Y = 0.26, ST_Z = 0.44$ for the Wedenberg model, respectively). This suggests that, in this plan, a relevant fraction of the overall D_2 uncertainty for the right optic nerve is attributable to interaction between setup and range uncertainty. Biological

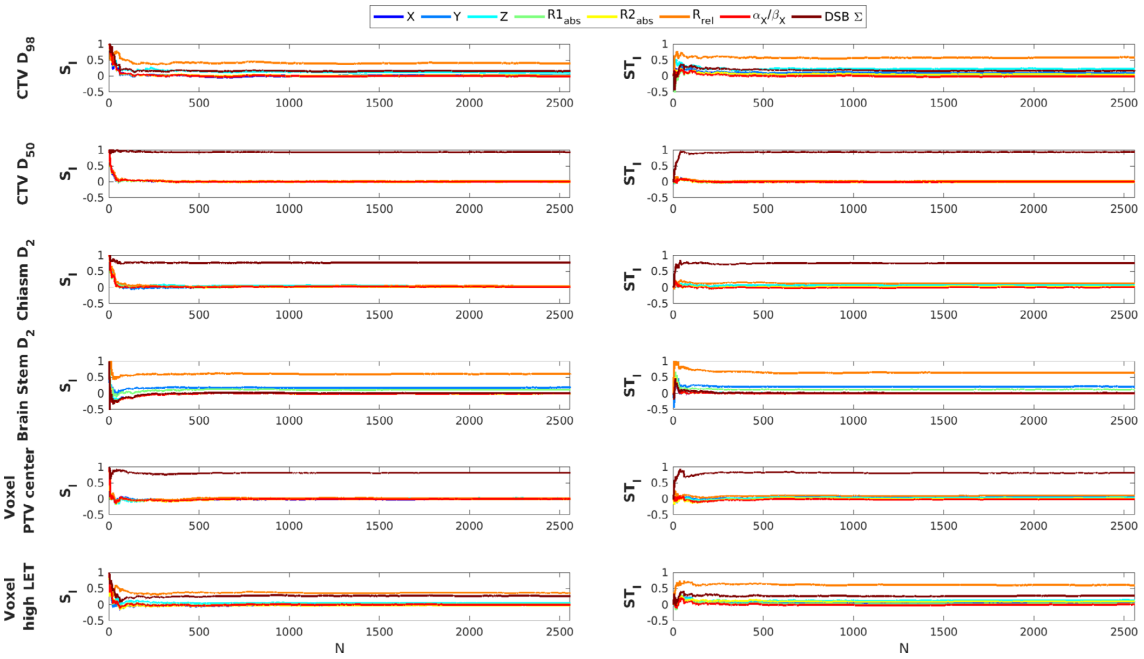

FIG. 1. Convergence of first-order sensitivity indices and total effects with sample size N for selected RW-DVH quantiles and two representative voxels for patient 1. [Color figure can be viewed at wileyonlinelibrary.com]

uncertainty generally was driven by $DSB\Sigma$ for the RMF model and by q and β_P for the Wedenberg model and the most important contribution to the CTV D_{50}(e.g., for patient 2: $S_{DSB\Sigma}=0.75, ST_{DSB\Sigma}=0.77$ for the RMF model and $S_q=0.42, S_{\beta_P}=0.23, ST_q=0.43, ST_{\beta_P}=0.23$ for the Wedenberg model, respectively). In both models, the relative impact of the x-ray reference parameters α_X/β_X was very low in comparison (e.g., for the CTV D_{50} for patient 2: $S_{(\alpha/\beta)_X}<0.01, ST_{(\alpha/\beta)_X}<0.01$ for the RMF model and $S_{(\alpha/\beta)_X}=0.02, ST_{(\alpha/\beta)_X}=0.02$ the Wedenberg model, respectively). Biological uncertainty was also the most important contribution to the chiasm D_2 for patient 1 ($S_{DSB\Sigma}=0.78$ for the RMF model and $S_q=0.41$ and $S_{\beta_P}=0.14$ for the Wedenberg model). The relative range uncertainty R_{rel} was an important input factor for many investigated DHV quantiles with the exception of the D_{50} of the CTV and the D_2 of the brain stem for patient two, which due to its position lateral to the two opposing beams from 90° and 270° was not affected by range shifts. For this parameter, the most relevant contribution to overall uncertainty is observable for a patient shift in Y direction ($S_Y=0.71$ for the RMF model and $S_Y=0.69$ for the Wedenberg model, respectively).

3.B. Voxelwise SA

The result of the voxel-based SA assuming $\alpha_X/\beta_X = 2$ Gy with a standard deviation of 10 % for patient 1 is shown in Fig. 5 for the RMF model and in Fig. 6 for the Wedenberg model. Nominal RWD distribution, the local standard deviation as a measure of local uncertainty and the dose-weighted LET distribution are shown in the first row. SA maps report the contribution of the input uncertainties to the local variance for every voxel, indicating the spatial changes of the impact of different uncertainties. The largest uncertainties are observed at the distal end of the beams, were they are governed by R_{rel}. The impact of the absolute range uncertainties $R1_{abs}$ and $R2_{abs}$ is small in comparison, as well as the uncertainty in the x-ray reference parameters α_X/β_X. In the CTV and in the entrance plateaus, the biological input factors β_P for the Wedenberg and DSB Σ for the RMF model are the most important contributions, where the overall uncertainty is generally lower than at the distal ends of the beams.

4. DISCUSSION

The presented framework is, to the best of our knowledge, the first implementation of a tool for variance-based sensitivity analysis of the combined impact of setup, range and RBE uncertainties in proton therapy, including also their interactions. Additionally to the numerical calculation of confidence intervals for the RBE-weighted dose in every voxel and RW-DVH quantiles, it allows to break down the overall uncertainty to the impact of the different sources of uncertainty. This complimentary sensitivity information has not yet been reported or used in proton therapy. The computation times were below 40 min which is extremely fast given the recalculation of $\sim 3\times10^4$

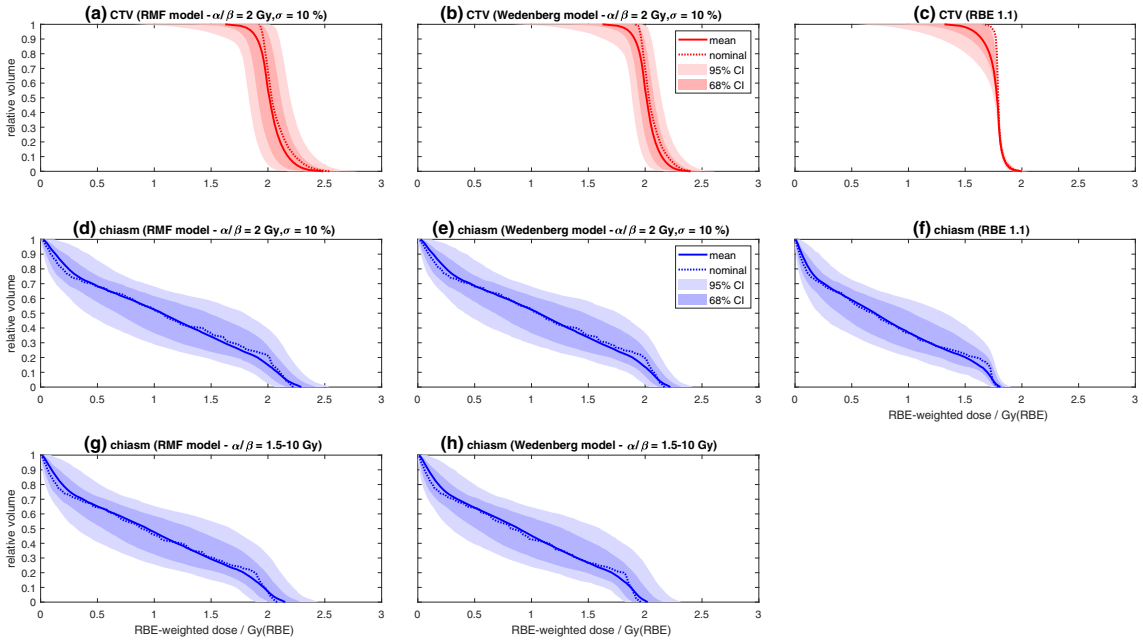

FIG. 2. RW-DVHs for the clinical target volume and the chiasm for a plan optimized for a constant RBE of 1.1 for patient 1. The uncertainty analysis was performed by recalculating the dose using the RMF (a and d) and the Wedenberg model (b and e) including range, setup, and RBE uncertainty. Panels (c) and (f) show the RW-DVHs for a constant RBE of 1.1 including only range and setup uncertainty. Panels (g) and (h) show the variation of the RW-DVH of the chiasm including range, setup and RBE uncertainty when α_X/β_X is varied over the larger interval from 1.5 to 10 Gy for comparison. 68% and 95% confidence intervals of the RW-DVHs are visualized by the shaded areas. "Nominal" refers to a forward calculation in the respective model with all input factors fixed to their nominal value. The solid line shows the expectation value of the DVH. [Color figure can be viewed at wileyonlinelibrary.com]

(corresponding to N = 2560 in the Saltelli formalism) treatment plans per SA execution for patient 1. For patient 2, which has a considerably smaller CTV the simulation time was even shorter. This was expected, since both the number of treated voxels (due to the restriction to the 2 cm expansion of the target volume) and the number of PBS spots increase with the target volume and therefore the number of entries in the *ij*-matrices increase. The quick convergence of the sensitivity indices suggests that actually a much smaller number of about N = 500 would already be sufficient. Since the calculation time scales linearly with the number of dose calculations, this would mean a reduction by 80%, to well below 10 minutes for patient 1 and to less than 2 and a half minutes for patient 2. The SA was performed for RW-DVH quantiles and the RWD in every voxel of interest. Further plan quality metrics based on the RWD distribution such as equivalent uniform dose, homogeneity index, conformity index, tumor control, and normal-tissue complication probabilities and others could be included at very little extra computational cost. An alternative approach to modeling uncertainties was proposed by Bangert et al.,[8] who introduced analytical probabilistic modeling (APM), a technique to propagate setup and range uncertainties through a pencil beam dose calculation via analytical integration to calculate expectation values and variances for dose distribution and other plan quality indicators. Wieser et al.[36] used APM to investigate the influence of setup and range uncertainties on RWD distributions, however, uncertainties in the biological modeling itself were not considered in their work. Note that both works do not include the possibility to determine sensitivity values. Perkó et al.[9] used an alternative approach to sensitivity analysis using polynomial chaos expansion, but also did not consider uncertainties in RBE modeling.

4.A. Potential applications

The current performance of the SA framework is sufficient to be forward calculated for the clinical evaluation of proton treatment plans. In such a setting, the additional uncertainty and sensitivity information could support the decision for or against a treatment plan and help to find the optimal compromise. Forward calculation of the SA could also be used in planning studies for the systematic assessment of the impact of setup, range, and RBE uncertainty on clinically relevant dosimetric parameters in proton therapy. The information which type of uncertainty is dominating the overall uncertainty could help to prioritize research attempts to reduce the uncertainties. In this regard, higher cost effectiveness could be achieved by concentrating on the dominant contributions

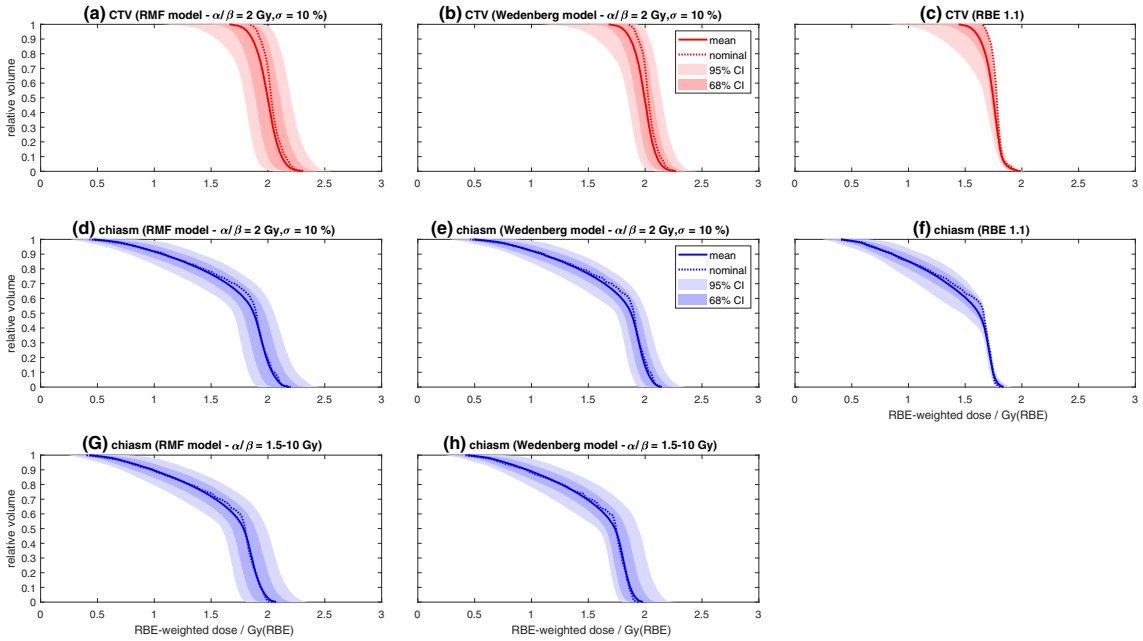

FIG. 3. RW-DVHs for the CTV and the chiasm for a plan optimized for a constant RBE of 1.1 for patient 2. The uncertainty analysis was performed by recalculating the dose using the RMF (a and d) and the Wedenberg model (b and e) including range, setup, and RBE uncertainty. Panels (c) and (F) show the RW-DVHs for a constant RBE of 1.1 including only range and setup uncertainty. Panels (g) and (h) show the variation of the RW-DVH of the chiasm including range, setup, and RBE uncertainty when α_X/β_X is varied over the larger interval from 1.5 to 10 Gy for comparison. 68% and 95% confidence intervals of the RW-DVHs are visualized by the shaded areas. "Nominal" refers to a forward calculation in the respective model with all input factors fixed to their nominal value. The solid line shows the expectation value of the DVH. [Color figure can be viewed at wileyonlinelibrary.com]

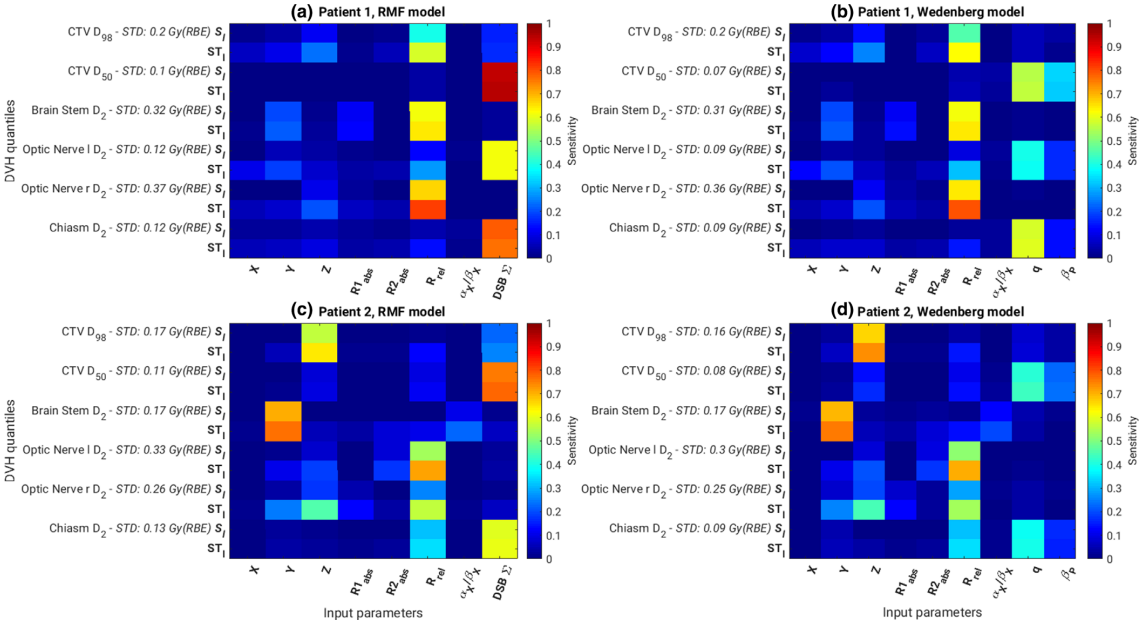

FIG. 4. First-order sensitivities and total effects for selected DVH quantiles of the CTV, brain stem, the optic nerves, and the chiasm for both patients and both RBE models in the calculation with $\alpha_X/\beta_X = 2$ Gy with a standard deviation of 10%. The empirical standard deviations of the respective quantile are also reported. [Color figure can be viewed at wileyonlinelibrary.com]

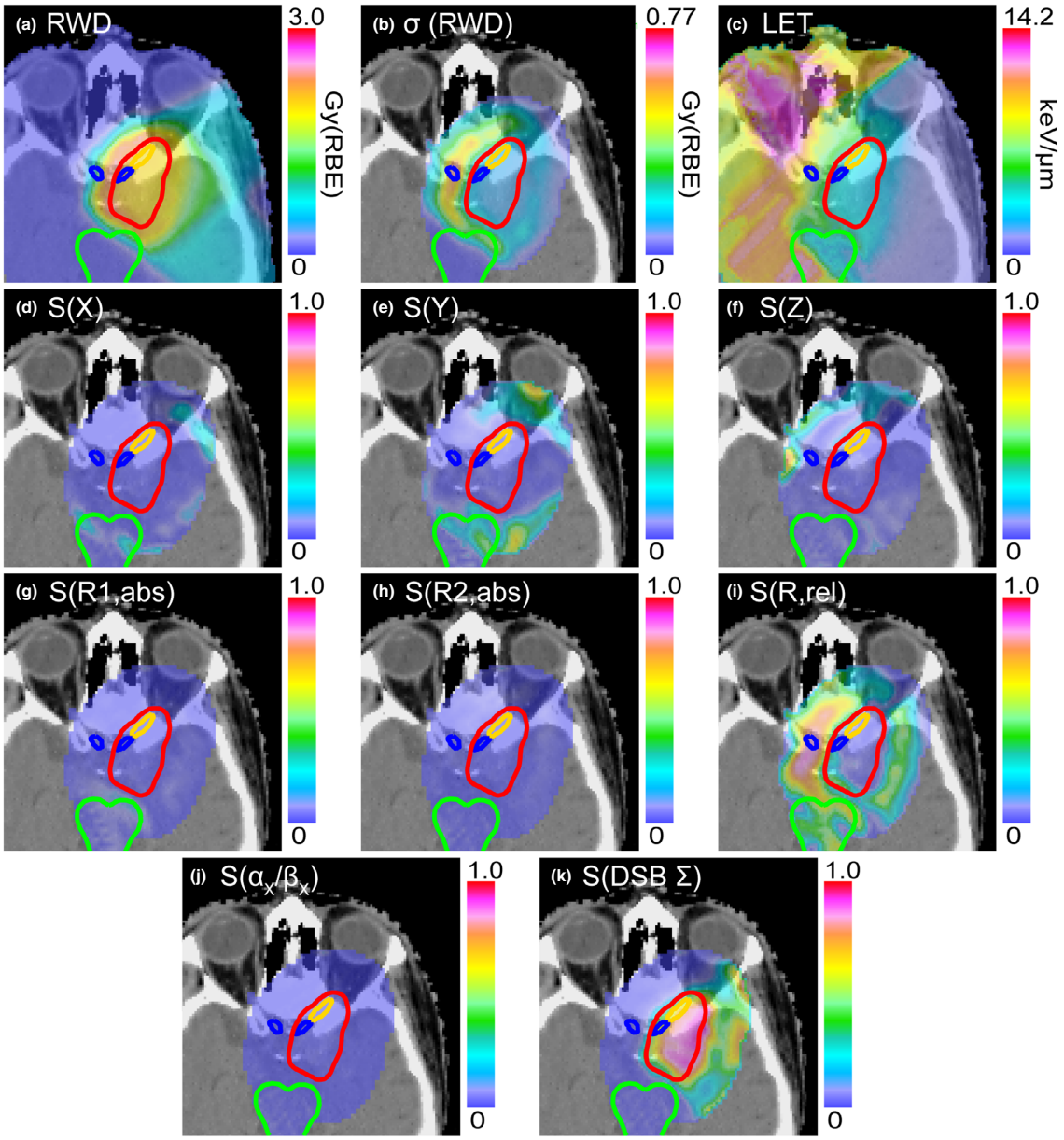

FIG. 5. RWD distribution, local standard deviation, LET distribution, and sensitivity maps for patient 1 and the RMF model in the calculation with range, setup, and RBE uncertainties included. For α_X/β_X, a nominal value of 2 Gy and a standard deviation of 10% was assumed. [Color figure can be viewed at wileyonlinelibrary.com]

to overall uncertainty. Another possible application of the SA framework could be the systematic comparison of proton treatment plans to evaluate, for example, different robust planning concepts.[10,11] This would allow to determine the residual uncertainty of RW-DVH quantiles of interest for these plans and analyze the sources of this uncertainty using the sensitivity indices.

4.B. Limitations

Current limitations of our SA framework include the restriction to rigid patient shifts, excluding rotations. Deformations are not explicitly modeled, either, although some nonrigid changes (such as weight loss and filling of air cavities with fluid) are modeled by the employed heuristic model

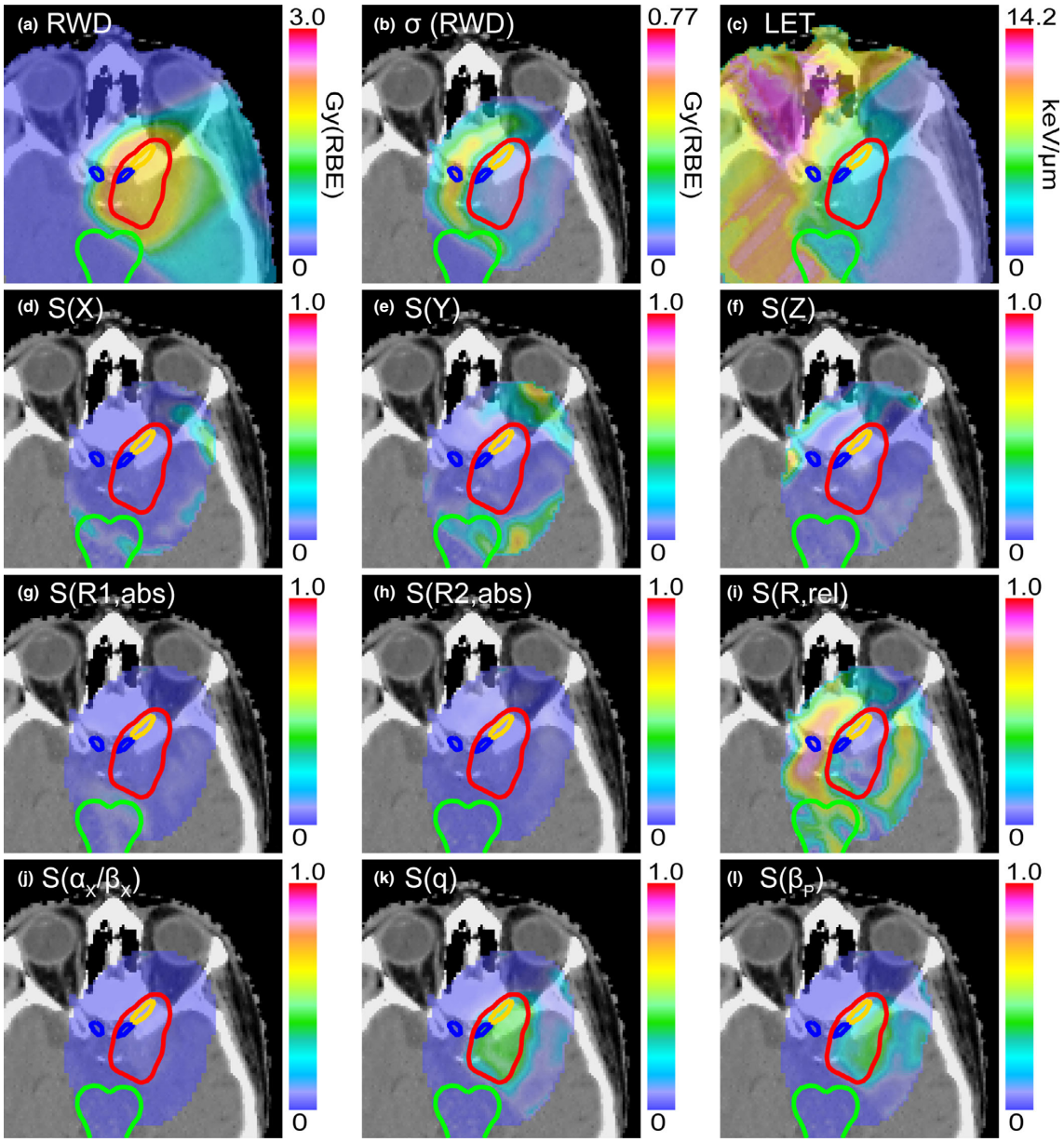

FIG. 6. RWD distribution, local standard deviation, LET distribution, and sensitivity maps for patient 1 and the Wedenberg model in the calculation with range, setup, and RBE uncertainties included. For α_X/β_X,a nominal value of 2 Gy and a standard deviation of 10% was assumed. [Color figure can be viewed at wileyonlinelibrary.com]

of absolute range uncertainties. However, considerable deformations of the patients' anatomy cannot be modeled. Furthermore, the method does not yet cover all possible types of uncertainties. Additional uncertainties exist in radiotherapy planning and delivery, which are not included in our approach, for example, inter- and intraobserver delineation variability. In this work, a pencil beam algorithm based on precalculated Geant4 simulated data in water was used. Although Monte Carlo algorithms are known to be more accurate than pencil beam algorithms, the necessary high number of RWD calculations cannot be achieved with a Monte Carlo algorithm in reasonable time. The accuracy of pencil beam algorithms is known to decrease in regions with high tissue heterogeneity, therefore, results obtained with the

SA framework using the current pencil beam algorithm will be less reliable in such cases.

Having a good assumption of the underlying uncertainties in the input factors is crucial for the execution of the SA. Unfortunately, these uncertainties can be difficult to estimate, in particular for the biological parameters. For example, a 95% confidence interval of about ±18% was reported for q as a fit parameter over various in-vitro experiments,[32] which corresponds to standard deviation of 9% for normal distributed data. To account for additional uncertainties related to the transfer from in-vitro data to the clinic, a standard deviation of 15% was assumed for q. The 5% standard deviation for DSB Σ in the RMF model was based on reasoning about the underlying Monte Carlo simulation of DSB induction.[37] However, these should be considered rather rough estimates of the actual uncertainty. Therefore, we did not aim at comparing the RBE prediction uncertainties of the two models. The objective is to show the flexibility of the approach with regard to the used biological model. It should also be kept in mind that the variance-based SA gives information about the variability, that is, the precision of the output, but does not give any information about the accuracy of a model. This means, for instance, that a higher robustness of an RBE model against uncertainties in its input parameters does not imply a higher accuracy.

In our analysis, the impact of the x-ray reference parameter α_X/β_X on the overall RWD variability was low compared to the other biological parameters when the RWD of a single fraction was calculated, even when α_X/β_X was varied over the large interval from 1.5 to 10 Gy. This means that the used RBE models are rather robust against α_X/β_X variability. It should be stressed, however, that this does not include fractionation effects.

4.C. Outlook

In this first analysis we applied the SA framework to proton therapy. The application to other charged particle types, such as helium or carbon ions could be achieved in the same way. Given that for these heavier ions the RBE is generally expected to be higher than for protons, a systematic assessment of uncertainty might be even more important in these cases.

Given the present performance of our SA framework, also future applications in robust plan optimization itself are imaginable if the execution of the variance-based SA can be further accelerated. While the framework is currently limited to the forward evaluation of proton treatment plans since the code still takes too long to be executed during optimization (for our patient cases from a few minutes to more than half an hour), the quick convergence of the sensitivity indices suggests that a considerable reduction of the number of model evaluations is feasible. In addition, the sensitivity analysis could be restricted to regions of interest with respect to plan robustness. The use of multiple, high-end GPUs with more memory for this highly parallelizable code is also expected to significantly improve the performance. All this might accelerate the estimation of the sensitivity indices to a point where they can be evaluated during optimization. To date, most robust optimization approaches do not include RBE variability.[10] If at all, RBE is only considered indirectly using LET as a surrogate. While it is in theory possible to fully compensate for setup and range uncertainty (although at the cost of additional dose to normal tissue), this is not the case for RBE uncertainty. Although RBE uncertainty can be reduced by avoiding excessive LET hot spots, it cannot be fully eliminated by shaping the physical dose distribution. Explicit inclusion of RBE uncertainty would therefore lead to an inevitably larger overall uncertainty, rendering current robust optimization approaches insufficient. The complimentary sensitivity information has the potential to overcome these limitations since it allows introducing additional SA-based cost functions into the optimization. For example, one could use SA-based cost functions ensuring, for example, $ST_{X,Y,Z}(D_{95\%,CTV})<5\%$ and $ST_{R_{abs},R_{rel}}(D_{95\%,CTV})<5\%$ while allowing for larger sensitivity values in the biological inputs. By using the total effects also interactions between physical and RBE uncertainties are taken into account. Once the necessary performance for the execution of the variance-based SA during inverse planning is achieved, this will allow a systematic approach to physically and biologically robust IMPT planning. The consecutive step should then be followed by an evaluation of clinically relevant scenarios with focus on achievable improvements in proton therapy planning.

5. CONCLUSIONS

A framework for global, variance-based sensitivity analysis of proton therapy treatment plans has been implemented and demonstrated for two different variable RBE models. It is a powerful and flexible tool to assess the combined impact and interactions of positioning, range, and RBE uncertainties. Besides resulting overall uncertainties, the method provides quantitative information on the relative impact of the different input factors, which might have implications for future biologically robust IMPT planning.

ACKNOWLEDGMENT

This project was supported by the DFG grant KA 4346/1-1 and the DFG Cluster of Excellence Munich Center for Advanced Photonics (MAP). Open access funding enabled and organized by ProjektDEAL.

CONFLICT OF INTEREST

The authors have no conflict of interest to disclose.

APPENDIX A

The following paragraphs describe how the individual sources of uncertainty are modeled.

A. MODELING OF PATIENT SHIFTS

In the particle extension of CERR, the dose calculation is performed as follows:

$$D_{ij} = PDD_{E_j}(RD_{ij}) \cdot \frac{1}{2\pi \cdot \sigma^2_{E_j}(RD_{ij})} \cdot \exp\left(-\frac{r^2_{ij}}{2 \cdot \sigma^2_{E_j}(RD_{ij})}\right) \tag{A1}$$

where PDD_{E_j} and $\sigma^2_{E_j}$ are precalculated look-up tables for the depth-dose-curve and the lateral dose spread in water for incident proton energy E_j in water, RD_{ij} denotes the radiological depth on the central beam axis of the j-th spot at the depth of the i-th voxel, and r_{ij} is the distance of the i-th voxel to the central beam axis of the j-th spot. The lookup tables PDD_{E_j} and $\sigma^2_{E_j}$ were precalculated in water using the Monte Carlo algorithm Geant4 for all relevant incident energies (50 to 260 MeV in steps of 1 MeV) assuming generic, mono-energetic beams.

Once the D_{ij} matrix is obtained, the dose in the i-th voxel can be calculated as:

$$d_i = \sum_j D_{ij}\omega_j \tag{A2}$$

With a vector containing the pencil beam scanning (PBS) spot weights ω. Therefore, the full dose vector can be obtained by a matrix-vector multiplication. In the particle extension of CERR, this is used for treatment plan optimization: Eq. (A2) is evaluated repeatedly to find the optimal weight vector. Throughout the entire optimization, D_{ij}, which contains all geometric information, is kept constant.

In order to recalculate treatment plans for a changed geometry, a fast way to generate the changed influence matrix is required. To achieve this, the following approximations are made: First, nondivergent beams are assumed, which is equivalent to assuming that the source is far away from the patient. The second approximation is that no patient deformations occur and the third that only rigid translations (isocenter shifts) are modeled, excluding rotations.

Then, r_{ij} and RD_{ij} in Eq. (A1) have to be replaced in order to reflect a patient shift. When r_{ij} is expressed in a two-dimensional Cartesian coordinate with axes perpendicular to the beam (i.e., a beams-eye-view (BEV) coordinate system):

$$r^2_{ij} = x^2_{ij} + y^2_{ij} \tag{A3}$$

The changes to the lateral offsets x_{ij} and y_{ij} caused by a rigid patient shift are then, in the approximation of nondivergent beams, the projection of the shift onto these axis:

$$x'_{ij} = x_{ij} + \Delta x(\varphi_n) \tag{A4}$$

$$y'_{ij} = y_{ij} + \Delta y(\varphi_n) \tag{A5}$$

where x'_{ij} and y'_{ij} denote the updated lateral offsets, which, for a given patient shift and in the approximation of nondivergent beams, only depend on the gantry angle φ_n of the beam n, making the computation very efficient for large ij-matrices, since all entries belonging to the same beam can be treated in the same manner.

RD_{ij} can be updated quickly by precalculating a set of neighboring raytracings of the original beam axis. Those raytracings are performed parallel to the original beam axis. The positions are defined on a 2D regular grid in the BEV coordinate system. During dose calculation, the algorithm has to select the correct neighbor raytracing RD^*_{ij} to replace RD_{ij} based on the lateral offsets Δx and Δy from Eqs. (A4) and (A5). This method is similar to the "virtual beamlets" approach proposed by Unkelbach et al.,[38] with the difference, that in our approach only the raytracing is approximated by the neighbor which is closest to the patient shift, while the lateral part in Eq. (A1) is modeled exactly according to Eqs. (A4) and (A5). The approach to keep precalculated neighboring raytracings for every PBS spot is memory intensive, however, since only small setup errors are expected and need to be treated in the SA, sets of only a few shifts of up to a few millimeters are sufficient. In our calculations, we used a 5 by 5 grid of raytracings (where the raytracing at the center corresponded to the nominal case without setup error) with a grid constant of 2 mm, therefore setup errors of up to about 4 mm can be handled. Since in our patient cases described below we assumed the setup error to be normal distributed in all three spatial dimensions with standard deviation 1 mm, this is sufficient for our purposes. If necessary, additional grid points can be included to support larger shifts at the cost of an increased memory usage.

B. MODELING OF RANGE UNCERTAINTY

Range uncertainty is modeled by applying a further transformation to the radiological depth:

$$RD_{ij} = (1 + \Delta RD_{rel}) \cdot RD^*_{ij} + \Delta RD_{abs} \tag{A6}$$

where RD^*_{ij} is the "neighbor raytracing" from the last paragraph, ΔRD_{rel} is the relative error mostly associated with imperfect CT number to stopping power conversion and ΔRD_{abs} is an absolute offset suited to model patient changes in the beam path (e.g., weight loss, filling of the paranasal sinus with liquid etc.).[1,39] In this approximation, the absolute range shift applied in one RWD calculation is the same for all PBS spots in one beam, therefore, perturbations only affecting parts of the beam cannot be modeled. The relative range shift is the same for all beams. This coupling between different beam directions is justified by the fact that the relative range shift is assumed to originate primarily in imperfect CT to stopping power conversion.

C. MODELING OF RBE UNCERTAINTY

Currently, two models for variable RBE predictions are supported: the mechanistic RMF and the phenomenological Wedenberg model.

C.1. RMF model

The repair-misrepair-fixation (RMF) model was introduced by Carlson et al.[29] In our implementation, it uses estimates from a Monte Carlo damage simulation (MCDS)[31] to link α_P and β_P to double strand break (DSB) yields.[30] For a given particle type and energy, these are calculated as:

$$\alpha_P = \frac{\Sigma}{\Sigma_X}\left[\alpha_X + 2\frac{\beta_X}{\Sigma_X}\left(\Sigma\cdot\bar{z}_F - \Sigma_X\cdot\bar{z}_{F,X}\right)\right] \tag{A7}$$

$$\sqrt{\beta_P} = \sqrt{\beta_X}\cdot\frac{\Sigma}{\Sigma_X} \tag{A8}$$

where α_X and β_X are the reference x-ray reference radiosensitivity parameters, Σ and Σ_X are the DSB yields for the particle (defined as the initial number of DSB per Gray per giga base pair $\mathrm{Gy}^{-1}\,\mathrm{Gbp}^{-1}$) and reference radiation of a Co-60 source, respectively; and $\bar{z}_F$ and $\bar{z}_{F,X}$ denote the frequency-mean specific energy. The default RMF model settings were used for the predictions. The model does not require any fit to experimental data. The MCDS software version 3.10A[31] with default settings (cell nucleus diameter 5 µm) was used to calculate DSB yields and the frequency-mean specific energy for all relevant proton energies. The DSB yields and frequency-mean specific energy were used as inputs for the RMF model as previously demonstrated by Carlson et al.,[29] Frese et al.[30] and Kamp et al.[25]

A rapid implementation[25,26] of this model in the *ij*-formalism for carbon ions has already been used for a variance-based SA of biological uncertainties by Kamp et al.[15] and for RWD optimization by Guan et al.[40]. We use a similar approach. To obtain $\alpha_{P,ij}$ and $\beta_{P,ij}$ (the radiosensitivity parameters for the dose contribution of the *j*-th spot to the *i*-th voxel), Eqs. (A7) and (A8) need to be integrated against the fluence spectrum ϕ_{ij} and the stopping power *SP*, which are both a function of the particle energy *E*. By simulating the fluence spectra using Geant4 as described above, precalculated, tabulated data for the resulting integrals can be obtained.

Integration of Eqs. (A7) and (A8) against the fluence spectrum Φ_{ij} and the stopping power $SP(E)$ yields:

$$\begin{aligned}\alpha_{P,ij} &= \alpha_{x,i}\frac{\int_0^\infty \frac{\Sigma(\mathrm{E})}{\Sigma_X}\cdot\Phi_{ij}(E)\cdot SP(E)dE}{\int_0^\infty \Phi_{ij}(E)\cdot SP(E)dE} \\ &+ \frac{\int_0^\infty 2\beta_{X,i}\cdot\left[\frac{\Sigma(\mathrm{E})}{\Sigma_X}\right]^2\cdot\bar{Z}_F(E)\cdot\Phi_{ij}(E)\cdot SP(E)dE}{\int_0^\infty \Phi_{ij}(E)\cdot SP(E)dE} \\ &- \frac{\int_0^\infty 2\beta_{X,i}\cdot\frac{\Sigma(\mathrm{E})}{\Sigma_X}\cdot\bar{Z}_{F,X}\cdot\Phi_{ij}(E)\cdot SP(E)dE}{\int_0^\infty \Phi_{ij}(E)\cdot SP(E)dE}\end{aligned} \tag{A9}$$

$$\sqrt{\beta_{P,ij}} = \sqrt{\beta_{X,i}}\cdot\frac{\int_0^\infty \frac{\Sigma(\mathrm{E})}{\Sigma_X}\cdot\Phi_{ij}(E)\cdot SP(E)dE}{\int_0^\infty \Phi_{ij}(E)\cdot SP(E)dE} \tag{A10}$$

By introducing precalculated constants for the integrals:

$$\frac{\int_0^\infty \frac{\Sigma(\mathrm{E})}{\Sigma_X}\cdot\Phi_{ij}(E)\cdot SP(E)dE}{\int_0^\infty \Phi_{ij}(E)\cdot SP(E)dE} = C_{1,ij} \tag{A11}$$

$$\frac{\int_0^\infty 2\cdot\left[\frac{\Sigma(\mathrm{E})}{\Sigma_X}\right]^2\cdot\bar{Z}_F(E)\cdot\Phi_{ij}(E)\cdot SP(E)dE}{\int_0^\infty \Phi_{ij}(E)\cdot SP(E)dE} = C^*_{2,ij} \tag{A12}$$

equations (A9) and (A10) can be written as:

$$\begin{aligned}\alpha_{P,ij} &= \alpha_{X,i}\cdot C_{1,ij} + \beta_{X,i}\cdot C^*_{2,ij} - 2\beta_{X,i}\cdot\bar{z}_{F,X}\cdot C_{1,ij} \\ &= \left(\alpha_{X,i} - 2\beta_{X,i}\cdot\bar{z}_{F,X}\right)\cdot C_{1,ij} + \beta_{X,i}\cdot C^*_{2,ij}\end{aligned} \tag{A13}$$

$$\sqrt{\beta_{P,ij}} = \sqrt{\beta_{X,i}}\cdot C_{1,ij} \tag{A14}$$

This reparametrization is very closely related to the one used by Kamp et al.,[26] who used the two reparametrization constants $C_{1,ij}$ and $C_{2,ij}$. While in our case $C_{1,ij}$ is defined in exactly the same way, note that our $C^*_{2,ij}$ is related to $C_{2,ij}$ via:

$$C_{2,ij} = C^*_{2,ij} - 2\cdot\bar{z}_{F,X}\cdot C_{1,ij}]] \tag{A15}$$

The precalculated tables C_1 and C^*_2 are referenced with the radiological depth and the corresponding incident proton energy to obtain $C_{1,ij}$ and $C^*_{2,ij}$:

$$C_{1,ij} = C_{1,E_j}\left(RD_{ij}\right) \tag{A16}$$

$$C^*_{2,ij} = C^*_{2,E_j}\left(RD_{ij}\right) \tag{A17}$$

To model biological uncertainty in the RMF model, we will treat Σ as uncertain and apply a relative variation $\left(\frac{\Delta\Sigma}{\Sigma}\right)$. Under the assumption, that this variation is independent of the energy, $C_{1,ij}$ depends linearly on $\left(\frac{\Delta\Sigma}{\Sigma}\right)$. For $C^*_{2,ij}$, there is a quadratic dependence. Therefore, Eqs. (A13) and (A14) become:

$$\begin{aligned}\alpha'_{p,ij}\left(\frac{\Delta\Sigma}{\Sigma}\right) = &\left(\alpha_{X,i} - 2\beta_{X,i}\bar{z}_{F,X}\right)\cdot C_{1,ij}\cdot\left(1+\frac{\Delta\Sigma}{\Sigma}\right) + \\ &\beta_{X,i}\cdot C^*_{2,ij}\cdot\left(1+\frac{\Delta\Sigma}{\Sigma}\right)^2\end{aligned} \tag{A18}$$

$$\sqrt{\beta'_{P,ij}\left(\frac{\Delta\Sigma}{\Sigma}\right)} = \sqrt{\beta_{X,i}}\cdot C_{1,ij}\cdot\left(1+\frac{\Delta\Sigma}{\Sigma}\right) \tag{A19}$$

C.2. Wedenberg model

In the Wedenberg model,[32] α_P is assumed to depend on the x-ray reference radiosensitivity parameter and increase linearly with the linear energy transfer (LET)::

$$\frac{\alpha_{P,ij}}{\alpha_{X,i}} = 1 + \frac{q\cdot LET_{ij}}{(\alpha/\beta)_{X,i}} \tag{A20}$$

where $q = 0.434\,\mathrm{Gy}\,\frac{\mu\mathrm{m}}{\mathrm{keV}}$ is obtained from a fit to in-vitro cell survival data and LET_{ij} is the LET contribution of the *j*-th PBS spot to the *i*-th voxel. It is obtained by referencing precalculated depth-LET tables for the incident proton energies E_j with the radiological depth RD_{ij}:

$$LET_{ij} = LET_{E_j}\left(RD_{ij}\right) \tag{A21}$$

where LET_{E_j} contains MC calculated data for the dose-weighted LET in water simulated using Geant4 as described above. β_P is assumed to be equal to the reference value:

$$\frac{\beta_{P,ij}}{\beta_{X,i}} = 1 \tag{A22}$$

To include uncertainty in this model, both q and $\beta_{P,ij}$ were treated as uncertain:

$$q' = q \cdot \left(1 + \frac{\Delta q}{q}\right) \tag{A23}$$

$$\beta'_{P,ij} = \beta_{P,ij} \cdot \left(1 + \frac{\Delta \beta_P}{\beta_{P,ij}}\right) \tag{A24}$$

For both RBE models, $\alpha_{P,i}$ and $\sqrt{\beta_{P,i}}$ for the i-th voxel can then be calculated as dose-weighted sums in the ij-formalism[41]:

$$\alpha_{P,i} = \frac{1}{d_i}\sum_j \alpha_{P,ij} \cdot D_{ij} \cdot \omega_j \tag{A25}$$

$$\sqrt{\beta_{P,i}} = \frac{1}{d_i}\sum_j \sqrt{\beta_{P,ij}} \cdot D_{ij} \cdot \omega_j \tag{A26}$$

Then, the RBE is calculated using the formula:

$$RBE_i\left(\alpha_{X,i}, \beta_{X,i}, \alpha_{P,i}, \beta_{P,i}, d\right) = \frac{-\alpha_{X,i} + \sqrt{\alpha_{X,i}^2 + 4\beta_X d_i \cdot \left(\alpha_{P,i} + \beta_{P,i} d_i\right)}}{2\beta_{X,i} d_i} \tag{A27}$$

$RBE_i\left(\alpha_{X,i}, \beta_{X,i}, \alpha_{P,i}, \beta_{P,i}, d\right)$ reduces to $RBE_i\left(\alpha_{X,i}/\beta_{X,i}, LET_i, q, d\right)$ for the Wedenberg model and to $RBE_i\left(\alpha_{X,i}/\beta_{X,i}, C_{1,i}, C^*_{2,i}, d\right)$ for the RMF model, therefore the uncertainty in the x-ray reference parameters can be treated by varying one parameter, the fraction $\alpha_{X,i}/\beta_{X,i}$.

A convenient property of the ij-formalism is that the RWD calculation can be restricted to arbitrary subgroups regions of interest to reduce memory usage. In our calculations we typically restricted the RWD calculation to a 2 cm expansion of the CTV and all OARs for whom the DVH quantiles were included in the SA (optic nerves, chiasm, brain stem).

[a]Author to whom correspondence should be addressed. Electronic mail: jan.hofmaier@med.uni-muenchen.de; Telephone: 004989440076744.

REFERENCES

1. Paganetti H. Range uncertainties in proton therapy and the role of Monte Carlo simulations. *Phys Med Biol*. 2012;57:R99–R117.
2. Schuemann J, Dowdell S, Grassberger C, Min CH, Paganetti H. Site-specific range uncertainties caused by dose calculation algorithms for proton therapy. *Phys Med Biol*. 2014;59:4007–4031.
3. Lomax AJ. Intensity modulated proton therapy and its sensitivity to treatment uncertainties 1: the potential effects of calculational uncertainties. *Phys Med Biol*. 2008;53:1027–1042.
4. Lomax AJ. Intensity modulated proton therapy and its sensitivity to treatment uncertainties 2: the potential effects of inter-fraction and inter-field motions. *Phys Med Biol*. 2008;53:1043–1056.
5. Paganetti H. Relative biological effectiveness (RBE) values for proton beam therapy. Variations as a function of biological endpoint, dose, and linear energy transfer. *Phys Med Biol*. 2014;59:R419–R472.
6. Mohan R, Peeler CR, Guan F, Bronk L, Cao W, Grosshans DR. Radiobiological issues in proton therapy. *Acta Oncol (Madr)*. 2017;56:1367–1373.
7. Paganetti H. Proton relative biological effectiveness-uncertainties and opportunities. *Int J Part Ther*. 2018;5:2–14.
8. Bangert M, Hennig P, Oelfke U. Analytical probabilistic modeling for radiation therapy treatment planning. *Phys Med Biol*. 2013;58:5401–5419.
9. Perkó Z, van der Voort SR, van de Water S, Hartman CMH, Hoogeman M, Lathouwers D. Fast and accurate sensitivity analysis of IMPT treatment plans using Polynomial Chaos Expansion. *Phys Med Biol*. 2016;61:4646–4664.
10. Unkelbach J, Alber M, Bangert M, et al. Robust radiotherapy planning. *Phys Med Biol*. 2018;63:22TR02.
11. Unkelbach J, Paganetti H. Robust proton treatment planning: physical and biological optimization. *Semin Radiat Oncol*. 2018;28:88–96.
12. Sobol IM. Global sensitivity indices for nonlinear mathematical models and their Monte Carlo estimates. *Math Comput Simul*. 2001;55:271–280.
13. Borgonovo E, Plischke E. Sensitivity analysis: a review of recent advances. *Eur J Oper Res*. 2016;248:869–887.
14. Kamp F, Brüningk S, Cabal G, Mairani A, Parodi K, Wilkens JJ. Variance-based sensitivity analysis of biological uncertainties in carbon ion therapy. *Phys Medica*. 2014;30:583–587.
15. Kamp F, Wilkens JJ. Application of variance-based uncertainty and sensitivity analysis to biological modeling in carbon ion treatment plans. *Med Phys*. 2019;46:437–447.
16. Zvereva A, Kamp F, Schlattl H, Zankl M, Parodi K. Impact of interpatient variability on organ dose estimates according to MIRD schema: uncertainty and variance-based sensitivity analysis. *Med Phys*. 2018;45:3391–3403.
17. Sobol IM. Sensitivity estimates for nonlinear mathematical models. *Math Model Comput Exp*. 1993;1:407–414.
18. Homma T, Saltelli A. Importance measures in global sensitivity analysis of nonlinear models. *Reliab Eng Syst Saf*. 1996;52:1–17.
19. Saltelli A, Annoni P, Azzini I, Campolongo F, Ratto M, Tarantola S. Variance based sensitivity analysis of model output. Design and estimator for the total sensitivity index. *Comput Phys Commun*. 2010;181:259–270.
20. Sobol IM. On the distribution of points in a cube and the approximate evaluation of integrals. *USSR Comput Math Math Phys*. 1967;7:86–112.
21. Sobol' I, Turchaninov V, Levitan Y, Shukhman B. Quasi-random sequence generators. Ipm zak; 1992:30.
22. Deasy JO, Blanco AI, Clark VH. CERR: a computational environment for radiotherapy research. *Med Phys*. 2003;30:979–985.
23. Schell S, Wilkens JJ. Advanced treatment planning methods for efficient radiation therapy with laser accelerated proton and ion beams. *Med Phys*. 2010;37:5330–5340.
24. Brüningk SC, Kamp F, Wilkens JJ. EUD-based biological optimization for carbon ion therapy. *Med Phys*. 2015;42:6248–6257.
25. Kamp F, Cabal G, Mairani A, Parodi K, Wilkens JJ, Carlson DJ. Fast biological modeling for voxel-based heavy ion treatment planning using the mechanistic repair-misrepair-fixation model and nuclear fragment spectra. *Int J Radiat Oncol Biol Phys*. 2015;93:557–568.
26. Kamp F, Carlson DJ, Wilkens JJ. Rapid implementation of the repair-misrepair-fixation (RMF) model facilitating online adaption of radiosensitivity parameters in ion therapy. *Phys Med Biol*. 2017;62:N285–N296.
27. Lühr A, von Neubeck C, Pawelke J, et al. "Radiobiology of proton therapy": results of an international expert workshop. *Radiother Oncol*. 2018;128:56–67.
28. Paganetti H, Blakely E, Carabe-Fernandez A, et al. Report of the AAPM TG-256 on the relative biological effectiveness of proton beams in radiation therapy. *Med Phys*. 2019;46:e53–e78.
29. Carlson DJ, Stewart RD, Semenenko VA, Sandison GA. Combined use of Monte Carlo DNA damage simulations and deterministic repair

models to examine putative mechanisms of cell killing. *Radiat Res*. 2008;169:447–459.
30. Frese MC, Yu VK, Stewart RD, Carlson DJ. A mechanism-based approach to predict the relative biological effectiveness of protons and carbon ions in radiation therapy. *Int J Radiat Oncol Biol Phys*. 2012;83:442–450.
31. Stewart RD, Yu VK, Georgakilas AG, Koumenis C, Park JH, Carlson DJ. Effects of radiation quality and oxygen on clustered DNA lesionsand cell death. *Radiat Res*. 2011;176:587–602.
32. Wedenberg M, Lind BK, Hårdemark B. A model for the relative biological effectiveness of protons: the tissue specific parameter α/β of photons is a predictor for the sensitivity to LET changes. *Acta Oncol (Madr)*. 2013;52:580–588.
33. Mesías MC, Boda-Heggemann J, Thoelking J, Lohr F, Wenz F, Wertz H. Quantification and assessment of interfraction setup errors based on cone beam CT and determination of safety margins for radiotherapy. *PLoS One*. 2016;11:e0150326.
34. Wohlfahrt P, Möhler C, Stützer K, Greilich S, Richter C. Dual-energy CT based proton range prediction in head and pelvic tumor patients. *Radiother Oncol*. 2017;125:526–533.
35. Schulz-Ertner D, Karger CP, Feuerhake A, et al. Effectiveness of carbon ion radiotherapy in the treatment of skull-base chordomas. *Int J Radiat Oncol Biol Phys*. 2007;68:449–457.
36. Wieser HP, Hennig P, Wahl N, Bangert M. Analytical probabilistic modeling of RBE-weighted dose for ion therapy. *Phys Med Biol*. 2017;62:8959–8982.
37. Semenenko VA, Stewart RD. A fast Monte Carlo algorithm to simulate the spectrum of DNA damages formed by ionizing radiation. *Radiat Res*. 2004;161:451–457.
38. Unkelbach J, Bortfeld T, Martin BC, Soukup M. Reducing the sensitivity of IMPT treatment plans to setup errors and range uncertainties via probabilistic treatment planning. *Med Phys*. 2009;36:149–163.
39. Taasti VT, Bäumer C, Dahlgren CV, et al. Inter-centre variability of CT-based stopping-power prediction in particle therapy: survey-based evaluation. *Phys Imaging Radiat Oncol*. 2018;6:25–30.
40. Guan F, Geng C, Carlson DJ, et al. A mechanistic relative biological effectiveness model-based biological dose optimization for charged particle radiobiology studies. *Phys Med Biol*. 2018;64:015008.
41. Wilkens JJ, Oelfke U. Fast multifield optimization of the biological effect in ion therapy. *Phys Med Biol*. 2006;51:3127–3140.

SUPPORTING INFORMATION

Additional supporting information may be found online in the Supporting Information section at the end of the article.

Data S1. Application of the SA framework to an additional prostate case.

Chapter 5

Summary and outlook

Since quantitative uncertainties in radiation therapy may result in underdosage of the tumor volume or overdosage of organs-at-risk (OARs), which may lead to unexpected toxicities or tumor recurrence, a well-founded understanding of these uncertainties and adequate management strategies are required. In this thesis, a method for dose guided patient positioning based on recalculation of the original treatment plan on scatter corrected cone beam computed tomography (CBCT) images for management of anatomical changes in photon therapy for head and neck cancer has been discussed. Furthermore, a framework for variance-based sensitivity analysis of multiple uncertainties in proton therapy has been presented. By combining multiple types of uncertainty in a comprehensive variance-based sensitivity analysis, different types of uncertainty and their interactions can be considered, and their influence on the overall dosimetric parameters can be compared.

5.1 Dose-guided patient positioning

A scatter correction for CBCT images has been combined with a tool for multi-criterial dose guided patient positioning. The study shows the feasibility of a dose guided positioning workflow. In a comparison with a rigid registration based workflow involving 39 CBCTs of two head and neck cancer patients, target coverage was improved for the dose guided workflow. Sometimes OAR doses had to be traded against target coverage within their clinical tolerance limits. In the case of extreme anatomical changes, target coverage could no longer be restored with dose guided positioning and a re-planning was required. Compared to a fully adaptive workflow, only small advantages with respect to treatment time can be expected, since the most time-consuming step, on table contouring or revision of automatically delineated target and OAR structures is required in both the fully adaptive and the dose guided workflow. However, the dose guided approach has the advantage that no new treatment plan is created, which in most centers requires approval by a senior physician and a medical physicist. For this reason, the dose guided approach could have its place alongside adaptive re-planning in integrated systems. The workflow would then look like follows:

- Revise or delineate contours
- Perform dose guided alignment
- If a satisfactory dose distribution is found, apply treatment
- If not, trigger adaptive re-planning

Deep learning based approaches to scatter correction (e.g. Hansen et al., 2018; Kurz et al., 2019; Jiang et al., 2019; Rusanov et al., 2021) which are capable of performing a CBCT scatter correction in a few seconds might further accelerate the workflow in the future.

5.2 Variance-based sensitivity analysis

A framework for variance-sensitivity analysis of uncertainties in proton therapy has been presented. It is capable of re-calculating a proton treatment plan many times while simultaneously varying patient position, proton range and relative biological effectiveness (RBE) parameters within their assumed error distributions. In a second step, it was extended to include inter observer variability (IOV) by adding the capability to switch between multiple treatment plans (see appendix A.1). The Monte Carlo approach allows to determine the overall uncertainty and to calculate sensitivity indices: relative measures for the impact of each of the sources of uncertainty on the overall uncertainty of the dose to a certain voxel or plan quality indicators such as dose volume histogram (DVH) quantiles. By using a fast, graphics processing unit (GPU) accelerated pencil beam algorithm, calculation times of a few minutes up to 3 hours for $\sim 3 \cdot 10^4$ plan re-calculations were achieved. The framework could be used to systematically assess the impact of setup, range, RBE uncertainty and IOV on the overall uncertainty and could help to prioritize research attempts to reduce the input uncertainties. For example, it could help to answer the question how far range uncertainty can be reduced through technological innovation until there is no additional benefit with respect to the reduction of overall uncertainty, since other sources of uncertainty become the dominant contribution. Another potential application is the detailed evaluation and comparison of different margin concepts and robust planning approaches in presence of these uncertainties. Since these approaches typically are limited to robustness against setup and range uncertainty and do not explicitly include RBE uncertainty or IOV, it is an interesting question to what extent these uncertainties are implicitly compensated in these concepts. Also in this context it could be an interesting question what would be the effect of a reduction of setup and range uncertainty if this reduction motivates a reduction of margins or robust planning parameters.

5.3 Final remarks

The findings of this thesis suggest the feasibility of a dose-guided positioning workflow for management of inter-fraction motion and for a Monte Carlo approach to variance-based sensitivity analysis for multiple sources of uncertainty. Both the quantification of and management strategies for the various sources of uncertainty will remain a matter of ongoing research. In future work also the combination of aspects of the two projects presented in this work are conceivable. For example, dose calculation on scatter corrected CBCT images could be included into the sensitivity analysis framework to add the capability to take inter-fraction motion into account. In turn, the information obtained through the sensitivity analysis could be used to guide decision making in multi-criterial optimization.

Appendix A

Further publication

A.1 Technical Note: Combining inter-observer variability, range and setup uncertainty in a variance-based sensitivity analysis for proton therapy

Reprinted with permission from "Combining inter-observer variability, range and setup uncertainty in a variance-based sensitivity analysis for proton therapy." by Hofmaier J, Walter F, Hadi I, Rottler M, von Bestenbostel R, Dedes G, Parodi K, Niyazi M, Belka C and Kamp F; Physics and Imaging in Radiation Oncology (2021). 20:117-120. doi:10.1016/j.phro.2021.11.005

Physics and Imaging in Radiation Oncology 20 (2021) 117–120

Contents lists available at ScienceDirect

Physics and Imaging in Radiation Oncology

journal homepage: www.sciencedirect.com/journal/physics-and-imaging-in-radiation-oncology

Technical Note

Combining inter-observer variability, range and setup uncertainty in a variance-based sensitivity analysis for proton therapy

Jan Hofmaier [a,*], Franziska Walter [a], Indrawati Hadi [a], Maya Rottler [a], Rieke von Bestenbostel [a], George Dedes [c], Katia Parodi [c], Maximilian Niyazi [a], Claus Belka [a,d], Florian Kamp [a,b]

[a] Department of Radiation Oncology, University Hospital, LMU Munich, Munich, Germany
[b] Department of Radiation Oncology and CyberKnife Center, Faculty of Medicine, University Hospital Cologne, Cologne, Germany
[c] Department of Medical Physics, Faculty of Physics, LMU Munich, Munich, Germany
[d] German Cancer Consortium (DKTK), Munich, Germany

ARTICLE INFO

Keywords:
Proton therapy
Range uncertainty
Setup uncertainty
Inter-observer variability
Sensitivity analysis

ABSTRACT

Margin concepts in proton therapy aim to ensure full dose coverage of the clinical target volume (CTV) in presence of setup and range uncertainty. Due to inter-observer variability (IOV), the CTV itself is uncertain. We present a framework to evaluate the combined impact of IOV, setup and range uncertainty in a variance-based sensitivity analysis (SA). For ten patients with skull base meningioma, the mean calculation time to perform the SA including 1.6×10^4 dose recalculations was 59 min. For two patients in this dataset, IOV had a relevant impact on the estimated CTV $D_{95\%}$ uncertainty.

1. Introduction

Treatment plans in proton therapy are affected by range and setup uncertainties. These are typically compensated through margin concepts or robust planning approaches. Margin concepts aim at covering the clinical target volume (CTV) in presence of range and setup uncertainty [1]. However, due to inter-observer variability (IOV), the CTV itself is uncertain. While there are many studies assessing IOV, only few studies have investigated dosimetric consequences of IOV [2], e.g Lobefalo et al. [3] who investigated the dosimetric impact of IOV in three-dimensional conformal radiotherapy (3D-CRT) and volumetric modulated arc therapy for rectal tumours, Hellebust et. al. [4] who assessed the dosimetric impact of IOV in brachytherapy for cervical cancer and Eminowicz et al. [5], who studied the dosimetric impact of IOV in VMAT for cervical cancer. To the best of our knowledge, there is no study assessing the combined and relative impact of range, setup uncertainty and IOV in proton therapy in a quantitative way. The statistical method of variance-based sensitivity analysis (SA) is suited for this, since it can be used to assess the impact of uncertainty of multiple input parameters on the output of a quantitative model [6]. In the context of patient dose calculation in medical physics, the technique has been previously applied to relative biological effectiveness (RBE) uncertainties in carbon ion therapy [7,8] and to estimate the impact of interpatient variability on organ dose estimates in nuclear medicine [9]. Recently, a framework to evaluate the combined impact of range, setup and RBE uncertainty in a variance-based SA has been presented by our group [10]. In this technical note, an extension of the framework to include IOV is shown. The feasibility of the approach was demonstrated by using it to investigate the relative impact of IOV, range and setup uncertainty on proton plans for a dataset with ten patients with skull base meningioma.

2. Materials and methods

2.1. Variance-based sensitivity analysis

In the Monte Carlo method of global variance-based SA, the output of a model $Y = f(X)$ with k input factors $X = (x_1, x_2, \ldots, x_k)$ which are subject to uncertainty is recalculated many times while simultaneously and randomly varying the input factors within their assumed distributions. In our particular case, the model $f(X)$ corresponded to a dose calculation followed by a dose volume histogram (DVH) calculation. The output Y corresponded to DVH parameters of interest. The input factors $(x_1, x_2 \ldots x_k)$ included patient shifts in three spatial dimensions, absolute and relative range shifts as well as IOV, resulting in $k = 6$ input factors. The resulting variance $V(Y)$ is decomposed as [6]:

* Corresponding author.
E-mail address: jan.hofmaier@med.uni-muenchen.de (J. Hofmaier).

https://doi.org/10.1016/j.phro.2021.11.005
Received 30 September 2021; Received in revised form 16 November 2021; Accepted 16 November 2021
Available online 2 December 2021

$$V(Y) = \sum_{l=1}^{k} V_l + \sum_{l=1}^{k}\sum_{m>l}^{k} V_{lm} + \sum_{l=1}^{k}\sum_{m>l}^{k}\sum_{n>m}^{k} V_{lmn} + \ldots + V_{1\ldots k} \quad (1)$$

resulting in $(2^k - 1)$ terms. The first order terms are

$$V_l = V[E(Y|X_l)] \quad (2)$$

The expectation value $E(Y|X_l)$ is hereby calculated over all possible values of all input factors except for X_l, which is kept fixed. The second order terms, which are representing the interaction between the inputs X_l and X_m, are

$$V_{lm} = V[E(Y|X_l, X_m)] - V_l - V_m \quad (3)$$

Higher order terms are defined in an analoguous fashion. Sensitivity indices are defined by normalising to the overall variance

$$S_l = \frac{V_l}{V(Y)} \quad (4)$$

$$S_{lm} = \frac{V_{lm}}{V(Y)} \quad (5)$$

and so on. Total effect indices are defined by summing all terms of any order containing l:

$$ST_l = S_l + \sum_{m\neq l}^{k} S_{lm} + \ldots + S_{1\ldots k} \quad (6)$$

Like in a previous study from our group [10], the efficient Monte Carlo method proposed by Saltelli [6] was used for direct calculation of S_l and ST_l, and sampling from low-discrepancy quasi-random sequences was employed to improve convergence. This method requires $N(k+2)$ model evaluations, where N is typically of the order of 10^3. In our study, as described above, we had $k = 6$ input factors. We set $N = 2048$, which resulted in approximately $1.6{\cdot}10^4$ model evaluations. The sensitivity analysis framework was extended to include IOV. Additionally to the fast, graphics processing unit (GPU) based pencil beam algorithm capable of modeling setup and range variations described in the previous publication from our group [10], the possibility to include multiple treatment plans and to switch randomly between them was added.

2.2. Clinical dataset

Datasets of ten patients with benign (WHO grade I) meningioma of the skull base were included in this study. For all patients, contrast enhanced magnetic resonance imaging (MRI) and DOTATATE positron emission tomography (PET) images were available in addition to a planning computed tomography (CT).

2.3. Target delineation and treatment planning

A rigid image registration of MRI, PET and planning CT images was performed. For each patient, four clinicians independently delineated the gross tumor volume (GTV) taking into account all imaging modalities ($GTV_{observer}$). A consensus GTV (GTV_{STAPLE}) was created using the simultaneous truth and performance level estimation (STAPLE) algorithm [11] in the research treatment planning system computational environment for radiological research (CERR) [12]. This implementation of an expectation-maximization algorithm generates a probabilistic estimate of the true volume based on the volumes delineated by multiple observers. The GTV_{STAPLE} was used as the "ground truth" GTV. As an example, the four $GTV_{observer}$ and the GTV_{STAPLE} contours for patient number 1 are shown in the supplementary material. The $CTV_{observer}$ and the CTV_{STAPLE} were defined as the respective GTV without any margins applied (i.e. GTV = CTV), as suggested in a current guideline [13]. To obtain the planning target volumes (PTVs), gantry-angle specific margins were applied. To compensate for proton range uncertainty, larger margins were applied in beam direction than laterally. The applied margins were 6, 5 and 3 mm in distal, proximal and lateral directions, respectively. For a typical margin receipe of 3.5% + 3 mm, the distal margin of 6 mm would correspond to a radiological target depth of approximately 9 cm. Since all tumours were at the skull base and therefore at similar depths, the same absolute margins were applied to all patients for simplicity. For each $CTV_{observer}$ a $PTV_{observer}$ was created. For each $PTV_{observer}$ of each patient a spot scanning proton treatment plan with one beam was generated using non-robust optimization, resulting in a total number of 40 treatment plans (four treatment plans for each of the ten patients). The gantry angle was chosen individually for each patient. The proton plans were optimized to deliver 1.8 Gy (RBE) per fraction to the $PTV_{observer}$. A spatially constant RBE of 1.1 was assumed.

2.4. Application of the SA framework

Like in the previous study from our group [10], the variance-based SA was performed assuming the following uncertainty distributions for the input factors mentioned in Section 2.1: For patient shifts in X,Y and Z directions, a normal distribution with standard deviation $\sigma_{X,Y,Z} =$ 1 mm truncated to $2\sigma_{X,Y,Z}$ was assumed. For relative range shifts the probability density was set to a normal distribution with standard deviation $\sigma_{r,rel} = 3$ % truncated to $2\sigma_{r,rel}$. Additionally, absolute range shifts following a normal distribution with standard deviation $\sigma_{r,abs} = 1$ mm truncated to $2\sigma_{r,abs}$ were assumed. For IOV, an equal probability of p = 0.25 for each of the four observer treatment plans was chosen. To perform the SA, the dose distribution was re-calculated approximately $1.6{\cdot}10^4$ times (corresponding to $N = 2048$ and $k = 6$ in the Saltelli formalism, as described in Section 2.1) while simultaneously sampling from the above uncertainty distributions. An Nvidia Quadro RTX 8000 GPU with 48 gigabytes of memory was used. For the resulting dose distributions, DVHs were calculated for the CTV_{STAPLE}. Confidence intervals (CIs) and sensitivity indices for the dose level enclosing 95% of the CTV_{STAPLE} ($D_{95\%}$) were calculated. Convergence plots of the sensitivity indices were created. The obtained total effect indices ST were converted to SI_{IOV}, the sum of all interaction terms with involvement of IOV and SI_{other}, the sum of all interaction terms without involvement of IOV. By definition is

$$SI_{IOV} = ST_{IOV} - S_{IOV} \quad (7)$$

and due to normalization

$$SI_{other} = 1 - S_{setup} - S_{range} - ST_{IOV} \quad (8)$$

3. Results

The mean calculation time to perform the $1.6{\cdot}10^4$ dose calculations was 59 min. Large differences were observed for the calculation times for different patients, which ranged from 11 min to 195 min. Convergence plots for S_l and ST_l for an exemplary patient are shown in panels A and B of Fig. 1. By visual inspection of the convergence plots it becomes evident that a sufficient convergence was achieved well below $N =$ 2048.

Results for the $D_{95\%}$ are presented in Table 1. For six patients, the width of the $CI_{95\%}$ for the $D_{95\%}$ was below 0.18 Gy (10% of the prescribed dose of 1.8 Gy). Uncertainties of more than 10 % were observed for patients 2, 3, 7 and 9. Here the widths of the $CI_{95\%}$ for the $D_{95\%}$ were 0.57, 0.24, 0.28 and 0.48 Gy, respectively. Plots of the DVHs for the CTV_{STAPLE} for these four patients with their corresponding 95 % and 68 % CIs are shown in panels C to F of Fig. 1. For two of these patients, the overall influence of IOV was negligible ($S_{IOV} + SI_{IOV} < 0.05$ for patients 7 and 9). In both cases, range uncertainty was the most important contribution to overall uncertainty (S_{range} was 0.53 and 0.70 for patients 7 and 9, respectively). For patients 2 and 3, however, IOV played a major

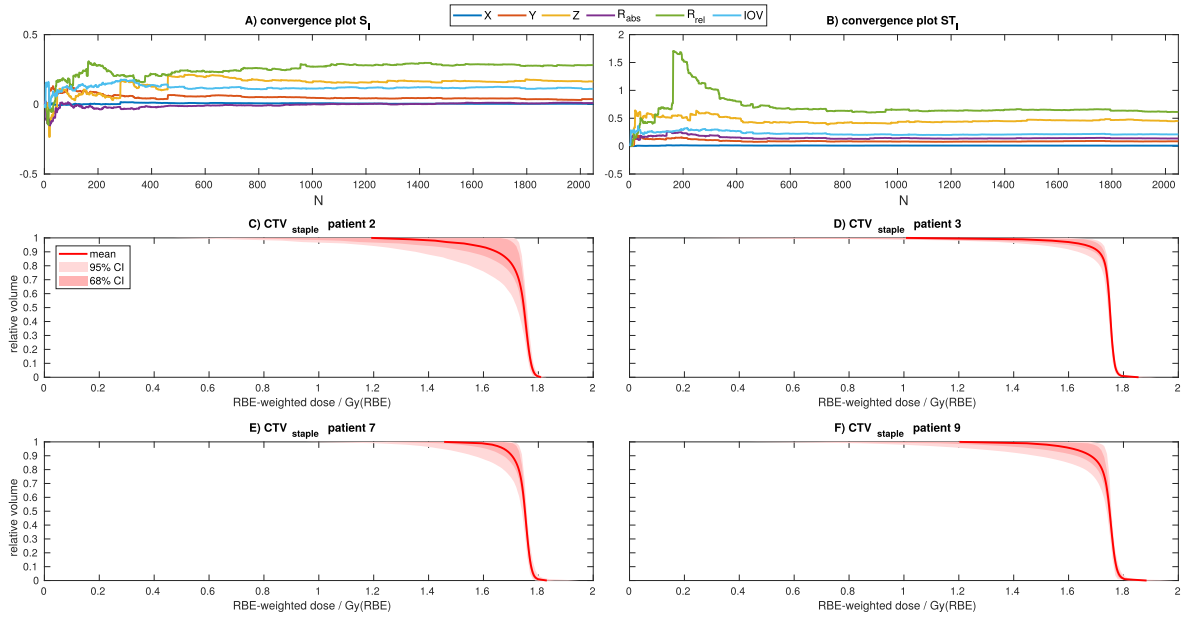

Fig. 1. Convergence plots for S_I and ST_I for one patient (panels A and B) and DVHs for CTV_{STAPLE} for the four patients with the largest overall $D_{95\%}$ uncertainties (panels C to F). The variability of the DVH in presence of setup uncertainty, range uncertainty and IOV is visualized by the shaded areas (68% and 95% CIs). The solid line indicates the mean value over all simulated error scenarios.

Table 1
Uncertainty and sensitivity analysis results for the $D_{95\%}$ for $(CTV)_{STAPLE}$. For each patient, the mean value and 95% and the 68% CIs have been calculated. The relative contribution to the overall uncertainty is broken down to first order indices S_{setup}, S_{range} and S_{IOV}, higher order indices with involvement of IOV (SI_{IOV}) and higher order indices without involvement of IOV (SI_{other}).

pat.	mean [Gy]	$CI_{95\%}$ [Gy]	$CI_{68\%}$ [Gy]	S_{setup}	S_{range}	S_{IOV}	SI_{IOV}	SI_{other}
1	1.71	1.62–1.74	1.69–1.73	0.21	0.29	0.11	0.10	0.29
2	1.56	1.16–1.73	1.35–1.72	0.12	0.35	0.34	0.09	0.10
3	1.66	1.49–1.73	1.59–1.71	0.14	0.11	0.62	0.01	0.12
4	1.70	1.59–1.73	1.68–1.72	0.19	0.14	0.10	0.12	0.45
5	1.73	1.71–1.74	1.72–1.74	0.37	0.31	0.00	0.14	0.18
6	1.73	1.70–1.74	1.72–1.73	0.20	0.29	0.03	0.04	0.44
7	1.67	1.45–1.73	1.61–1.73	0.25	0.53	0.00	0.02	0.20
8	1.69	1.58–1.74	1.65–1.73	0.23	0.49	0.04	0.05	0.19
9	1.62	1.25–1.73	1.48–1.71	0.13	0.70	0.01	0.00	0.16
10	1.73	1.70–1.74	1.72–1.74	0.26	0.24	0.02	0.06	0.42

role for overall uncertainty ($S_{IOV} + SI_{IOV}$ was 0.43 and 0.63 for patients 2 and 3, respectively).

4. Discussion

A framework for the variance-based SA of setup, range and IOV has been presented. To the best of our knowledge, this study is the first to assess the relative dosimetric impact of setup uncertainty, range uncertainty and IOV in a variance-based SA. In a first analysis of ten patients, calculation times were of the order of a few minutes to a few hours. These calculation times are fast enough for offline plan evaluation. Although this was not investigated in this study, it can be assumed that the differences in calculation time were caused by differences in the sizes and depths of the target volumes. The convergence plots in Fig. 1 suggest that actually less than $N = 2048$ would have been sufficient to achieve convergence, therefore the calculation times could be reduced by stopping the calculation after reaching a predefined convergence criterion. While for the majority of patients, the overall uncertainties in CTV coverage were small, in some cases the coverage was deteriorated. The dominating contributions to overall uncertainty were either range uncertainty or IOV. This suggests that IOV might have a relevant effect on target coverage in some patients.

In this work, the analysis was restricted to skull base meningioma, since the framework does not support organ motion at the moment. Furthermore, a pencil beam algorithm was used, whose accuracy is known to decrease in regions of high heterogeneity. The framework would be applicable without modification to other tumour sites for which these limitations are acceptable. The possibility to model motion could be included by extending the framework to use multiple CT geometries (e.g. phases of a 4D-CT to model breathing motion), at the cost of an increased memory usage and longer calculation times. In the previous publication from our group [10], uncertainties in variable RBE models were evaluated in combination with setup and range uncertainty. In this study, since the focus was on IOV, RBE uncertainty was not taken into account and a constant RBE of 1.1 was assumed. However, the combined evaluation of all four types of uncertainty could in principle also be included in the framework. This could be used in future studies to assess the combined impact of range, setup and RBE uncertainty and IOV. The evaluation of the CTV $D_{95\%}$ in presence of IOV required a "ground truth" CTV. Unfortunately, this volume is not known. In this

work, the consensus target volume created with the STAPLE algorithm was used to define a "ground truth" target volume, as has been done previously [14]. Since this algorithm provides a maximum likelyhood estimate for the actual CTV based on the observer CTVs themselves, this approach is well suited to capture the variability within a group of observers. However, it cannot correct systematic deviations from the ground truth CTV within the observer group. Furthermore, in this study only data from four observers was available, which was considered sufficient to show the feasibility of the approach. However, outlier contours could have considerable effect on the evaluation. For this reason, both the number of patients and the number of observers needs to be increased for future systematic evaluations of the impact of IOV in combination with setup and range uncertainties. Another limitation is that in our study simple proton plans with only one beam direction were used. More clinically realistic plans with multiple beam directions are supported by the framework without modifications, but have higher memory requirements and will lead to longer calculation times.

In this technical note, no metrics of contour similarity such as Dice coefficients or Hausdorff distances were evaluated. The presented framework might be used in future studies to investigate the correlation of these metrics with dosimetric parameters. It could also have potential applications in the investigation of the implications of uncertainty reduction. If technical advances such as dual energy computed tomography (DECT), proton CT and improved image guidance reduce range and setup uncertainty, the relative impact of IOV on overall uncertainty becomes larger. The SA framework could complement studies such as [15–17], who have investigated the impact of range and setup margin reduction. By also including IOV into the analysis, questions such as how far the overall uncertainty can be reduced by reduction of setup and range uncertainty before IOV becomes the limiting factor could be comprehensively investigated in future studies. Similarly, the following question could be assessed: Although not explicitly accounted for in the PTV concept, it can be assumed that IOV is compensated by the margins (or, in an analogous manner in the case of robust optimization, the plan robustness settings) to a certain extent. The SA framework could help to investigate whether a CTV-to-PTV margin reduction (or reduction of plan robustness settings) justified by reduced range and setup uncertainties would lead to an unexpected increase in uncertainty of CTV coverage caused by IOV.

In conclusion, a previously presented framework for variance-based sensitivity analysis has been extended to include IOV. The approach is feasible and enables the evaluation of the combined impact of setup and range uncertainty and IOV. In a first analysis of ten patients, IOV had a relevant impact on the CTV $D_{95\%}$ for two of these patients. This suggests that IOV could have a deteriorating effect on CTV coverage in some cases.

Declaration of Competing Interest

The authors declare the following financial interests/personal relationships which may be considered as potential competing interests: CB holds research grants from Elekta, Brainlab, Viewray and C-Rad without any relation to the research described here. The remaining authors declare that they have no competing interest.

Acknowledgements

This project was supported by the DFG grant KA 4346/1-1 and the DFG Cluster of Excellence Munich Center for Advanced Photonics (MAP).

Appendix A. Supplementary data

Supplementary data associated with this article can be found, in the online version, at https://doi.org/10.1016/j.phro.2021.11.005.

References

[1] Unkelbach J, Alber M, Bangert M, Bokrantz R, Chan TCY, Deasy JO, et al. Robust radiotherapy planning. Phys Med Biol 2018;63(22):22TR02. https://doi.org/10.1088/1361-6560/aae659.
[2] Vinod SK, Jameson MG, Min M, Holloway LC. Uncertainties in volume delineation in radiation oncology: A systematic review and recommendations for future studies. Radiother Oncol 2016;121(2):169–79. https://doi.org/10.1016/j.radonc.2016.09.009.
[3] Lobefalo F, Bignardi M, Reggiori G, Tozzi A, Tomatis S, Alongi F, et al. Dosimetric impact of inter-observer variability for 3D conformal radiotherapy and volumetric modulated arc therapy: The rectal tumor target definition case. Radiat Oncol 2013;8(1):176. https://doi.org/10.1186/1748-717X-8-176.
[4] Hellebust TP, Tanderup K, Lervåg C, Fidarova E, Berger D, Malinen E, et al. Dosimetric impact of interobserver variability in MRI-based delineation for cervical cancer brachytherapy. Radiother Oncol 2013;107(1):13–9. https://doi.org/10.1016/j.radonc.2012.12.017.
[5] Eminowicz G, Rompokos V, Stacey C, McCormack M. The dosimetric impact of target volume delineation variation for cervical cancer radiotherapy. Radiother Oncol 2016;120(3):493–9. https://doi.org/10.1016/j.radonc.2016.04.028.
[6] Saltelli A, Annoni P, Azzini I, Campolongo F, Ratto M, Tarantola S. Variance based sensitivity analysis of model output. Design and estimator for the total sensitivity index. Comput Phys Commun 2010;181(2):259–70. https://doi.org/10.1016/j.cpc.2009.09.018.
[7] Kamp F, Brüningk S, Cabal G, Mairani A, Parodi K, Wilkens JJ. Variance-based sensitivity analysis of biological uncertainties in carbon ion therapy. Phys Med 2014;30(5):583–7. https://doi.org/10.1016/j.ejmp.2014.04.008.
[8] Kamp F, Wilkens JJ. Application of variance-based uncertainty and sensitivity analysis to biological modeling in carbon ion treatment plans. Med Phys 2019;46(2):437–47. https://doi.org/10.1002/mp.13306.
[9] Zvereva A, Kamp F, Schlattl H, Zankl M, Parodi K. Impact of interpatient variability on organ dose estimates according to MIRD schema: Uncertainty and variance-based sensitivity analysis. Med Phys 2018;45(7):3391–403. https://doi.org/10.1002/mp.12984.
[10] Hofmaier J, Dedes G, Carlson DJ, Parodi K, Belka C, Kamp F. Variance-based sensitivity analysis for uncertainties in proton therapy: A framework to assess the effect of simultaneous uncertainties in range, positioning and RBE model predictions on RBE-weighted dose distributions. Med Phys 2021;48(2):805–18. https://doi.org/10.1002/mp.14596.
[11] Warfield SK, Zou KH, Wells WM. Simultaneous truth and performance level estimation (STAPLE): An algorithm for the validation of image segmentation. IEEE Trans Med Imaging 2004;23(7):903–21. https://doi.org/10.1109/TMI.2004.828354.
[12] Deasy JO, Blanco AI, Clark VH. CERR: A computational environment for radiotherapy research. Med Phys 2003;30(5):979–85. https://doi.org/10.1118/1.1568978.
[13] Combs SE, Baumert BG, Bendszus M, Bozzao A, Brada M, Fariselli L, et al. ESTRO ACROP guideline for target volume delineation of skull base tumors. Radiother Oncol 2021;156:80–94. https://doi.org/10.1016/j.radonc.2020.11.014.
[14] Kristensen I, Nilsson K, Agrup M, Belfrage K, Embring A, Haugen H, et al. A dose based approach for evaluation of inter-observer variations in target delineation. Tech Innov Patient Support Radiat Oncol 2017;3-4:41–7. https://doi.org/10.1016/j.tipsro.2017.10.002.
[15] van de Water S, van Dam I, Schaart DR, Al-Mamgani A, Heijmen BJM, Hoogeman MS. The price of robustness; impact of worst-case optimization on organ-at-risk dose and complication probability in intensity-modulated proton therapy for oropharyngeal cancer patients. Radiother Oncol 2016;120(1):56–62. https://doi.org/10.1016/j.radonc.2016.04.038.
[16] Tattenberg S, Madden TM, Gorissen BL, Bortfeld T, Parodi K, Verburg J. Proton range uncertainty reduction benefits for skull base tumors in terms of normal tissue complication probability (NTCP) and healthy tissue doses. Med Phys 2021;48(9):5356–66. https://doi.org/10.1002/mp.15097.
[17] Wagenaar D, Kierkels RGJ, van der Schaaf A, Meijers A, Scandurra D, Sijtsema NM, et al. Head and neck IMPT probabilistic dose accumulation: Feasibility of a 2 mm setup uncertainty setting. Radiother Oncol 2021;154:45–52. https://doi.org/10.1016/j.radonc.2020.09.001.

Appendix B

List of Publications

B.1 Peer-reviewed articles as first author

- **Hofmaier J**, Walter F, Hadi I, Rottler M, von Bestenbostel R, Dedes G, Parodi K, Niyazi M, Belka C, Kamp F (2021). Combining inter-observer variability, range and setup uncertainty in a variance-based sensitivity analysis for proton therapy. *Physics and Imaging in Radiation Oncology* 20:117-120. doi:10.1016/j.phro.2021.11.005

- **Hofmaier J**, Dedes G, Carlson DJ, Parodi K, Belka C, Kamp F (2021). Variance-based sensitivity analysis for uncertainties in proton therapy: Effect of simultaneous uncertainties in range, positioning and RBE model predictions on RBE-weighted dose distributions. *Medical Physics* 48(2):805-818. doi:10.1002/mp.14596

- **Hofmaier J**, Bodensohn R, Garny S, Hadi I, Fleischmann DF, Eder M, Dinc Y, Reiner M, Corradini S, Parodi K, Belka C, Niyazi M (2019). Single isocenter stereotactic radiosurgery for patients with multiple brain metastases: dosimetric comparison of VMAT and a dedicated DCAT planning tool. *Radiation Oncology* 14, 103. doi:10.1186/s13014-019-1315-z

- **Hofmaier J**, Haehnle J, Kurz C, Landry G, Maihoefer C, Schüttrumpf L, Süss P, Teichert K, Söhn M, Spahr N, Brachmann C, Weiler F, Thieke C, Küfer KH, Belka C, Parodi K, Kamp F (2017). Multi-criterial patient positioning based on dose recalculation on scatter-corrected CBCT images. *Radiotherapy and Oncology* Dec;125(3):464-469 doi:10.1016/j.radonc.2017.09.020

- **Hofmaier J**, Kantz S, Söhn M, Dohm OS, Bächle S, Alber M, Parodi K, Belka C, Niyazi M (2016). Hippocampal sparing radiotherapy for glioblastoma patients: a planning study using volumetric modulated arc therapy. *Radiation Oncology* 11, 118. doi:10.1186/s13014-016-0695-6

B.2 Peer-reviewed articles as co-author

- Fleischmann DF, Schön R, Corradini S, Bodensohn R, Hadi I, **Hofmaier J**, Forbrig R, Thon N, Dostotkar M, Belka C, Niyazi M (2021). Multifocal high-grade glioma radiotherapy safety and efficacy. *Radiation Oncology* 16, 165. doi:10.1186/s13014-021-01886-3

- Bodensohn R, Kaempfel AL, Fleischmann DF, Hadi I, **Hofmaier J**, Garny S, Reiner M, Forbrig R, Corradini S, Thon N, Belka C, Niyazi M (2021). Simultaneous stereotactic radiosurgery of multiple brain metastases using single-isocenter dynamic conformal arc therapy: a prospective monocentric registry trial. *Strahlentherapie und Onkologie* 197(7):601-613. doi: 10.1007/s00066-021-01773-6

- Meschini G, Kamp F, **Hofmaier J**, Reiner, Sharp GC, Paganetti H, Belka, Wilkens JJ, Carlson DJ, Parodi K, Baroni G, Riboldi M (2020). Modeling RBE-weighted dose variations in irregularly moving abdominal targets treated with carbon ion beams. *Medical Physics*. 47(7):2768-2778. doi:10.1002/mp.14135

- Hadi I, Roengvoraphoj O, Bodensohn R, **Hofmaier J**, Niyazi M, Belka, Nachbichler SB (2020). Stereotactic radiosurgery combined with targeted/ immunotherapy in patients with melanoma brain metastasis. *Radiation Oncology* 15, 37. doi:10.1186/s13014-020-1485-8

- Niepel K, Kamp F, Kurz C, Hansen D, Rit S, Neppl S, **Hofmaier J**, Bondesson D, Thieke C, Dinkel J, Belka C, Parodi K, Landry G (2018). Feasibility of 4DCBCT-based proton dose calculation: An ex vivo porcine lung phantom study. *Zeitschrift für Medizinische Physik* 29(3):249-261. doi:10.1016/j.zemedi.2018.10.005

- Kurz C, Süss P, Arnsmeyer C, Haehnle J, Teichert K, Landry G, **Hofmaier J**, Exner F, Hille L, Kamp F, Thieke C, Ganswindt U, Valentini C, Hölscher T, Troost E, Krause M, Belka C, Küfer KH, Parodi K, Richter C (2018). Dose-guided patient positioning in proton radiotherapy using multicriteria-optimization. *Zeitschrift für Medizinische Physik* 29(3):216-228. doi:10.1016/j.zemedi.2018.10.003

- Haehnle J, Süss P, Landry G, Teichert K, Hille L, **Hofmaier J**, Nowak D, Kamp F, Reiner M, Thieke C, Ganswindt U, Belka C, Parodi K, Küfer KH, Kurz C (2017). A novel method for interactive multi-objective dose-guided patient positioning. *Physics in Medicine & Biology* 62(1):165-185. doi:10.1088/1361-6560/62/1/165

- Kurz C, Kamp F, Park YK, Zöllner C, Rit S, Hansen D, Podesta M, Sharp GC, Li M, Reiner M, **Hofmaier J**, Neppl S, Thieke C, Nijhuis R, Ganswindt U, Belka C, Winey BA, Parodi K, Landry G (2016). Investigating deformable image registration and scatter correction for CBCT-based dose calculation in adaptive IMPT. *Medical Physics* 43(10):5635-5646. doi:10.1118/1.4962933

- Bodensohn R, Corradini S, Ganswindt U, **Hofmaier J**, Schnell O, Belka C, Niyazi M (2016). A prospective study on neurocognitive effects after primary radiotherapy in high-grade glioma patients. *International Journal of Clinical Oncology* 21(4):642-650. doi:10.1007/s10147-015-0941-1

B.3 Conference contributions as first author

- **Hofmaier J**, Walter F, Hadi I, Rottler M, von Bestenbostel R, Dedes G, Parodi K, Niyazi M, Kamp F. Variance-based sensitivity analysis of inter-observer variability, range and setup uncertainties in proton therapy. *ESTRO 2021, poster highlight.*

- **Hofmaier J**, Walter F, Hadi I, Rottler M, Steffens R, Dedes G, Parodi K, Belka C, Kamp F. Variance-based sensitivity analysis of inter-observer variability, setup and range uncertainties in proton therapy. *DGMP 2020, oral presentation.*

- **Hofmaier J**, Dedes G, Carlson DJ, Parodi K, Belka C, Kamp F. Variance-based sensitivity analysis for uncertainties in proton therapy: Effect of simultaneous uncertainties in range, positioning and RBE model predictions on RBE-weighted dose distributions. *BiGART 2019, poster.*

- **Hofmaier J**, Bodensohn R, Garny S, Reiner M, Eder M, Dinc Y, Corradini S, Belka C, Niyazi M. Mono-isozentrische Radiochirurgie für Patienten mit multiplen Hirnmetastasen: dosimetrischer Vergleich von DCAT und VMAT. *DEGRO 2019, oral presentation.*

- **Hofmaier J**, Dedes G, Carlson DJ, Parodi K, Belka C, Kamp F. A framework for variance-based sensitivity analysis of uncertainties in proton therapy. *ESTRO 2019, oral presentation.*

- **Hofmaier J**, Bodensohn R, Garny S, Reiner M, Eder M, Dinc Y, Corradini S, Belka C, Niyazi M. Single isocenter SRS for multiple brain metastases: dosimetric comparison of DCAT and VMAT. *ESTRO 2019, poster.*

- **Hofmaier J**, Dedes G, Carlson DJ, Parodi K, Belka C, Kamp F. Variance-based sensitivity analysis of uncertainties in proton therapy. *DGMP 2018, oral presentation.*

- **Hofmaier J**, Haehnle J, Kurz C, Landry G, Maihoefer C, Süss P, Teichert K, Traulsen N, Brachmann C, Weiler F, Thieke C, Küfer KH, Belka C, Parodi K, Kamp F. Multi-criterial patient positioning based on dose recalculation on scatter-corrected CBCT images. *ESTRO 2017, oral presentation.*

- **Hofmaier J**, Kantz S, Söhn M, Alber M, Parodi K, Belka C, Niyazi M. Hippocampal-sparing radiotherapy for glioblastoma patients using the VMAT technique. *ESTRO 2016, e-poster.*

B.4 Conference contributions as co-author

- Fleischmann DF, Buettner M, Unterrainer M, Corradini S, Zollner B, **Hofmaier J**, Bodensohn R, Thon N, Belka C, Bartenstein P, Albert N, Niyazi M. ^{18}F-GE-180 TSPO PET in high-grade glioma RT planning. *ASTRO 2021, poster.*

- Rabe M, Paganelli C, Schmitz H, Meschini G, Riboldi M, **Hofmaier J**, Dinkel J, Reiner M, Parodi K, Belka C, Landry G, Kamp F, Kurz C. Time-resolved estimated synthetic CTs based on orthogonal cine MRI for MR-guided proton therapy. *4D treatment workshop on particle therapy 2021, poster*

- Rabe M, Paganelli C, Schmitz H, Meschini G, Riboldi M, **Hofmaier J**, Dinkel J, Reiner M, Parodi K, Belka C, Landry G, Kurz C, Kamp F. Experimental validation of time-resolved estimated synthetic CTs at 3.65 Hz for MR-guided lung tumor treatments. *Joint Conference of the ÖGMP, DGMP and SGSMP 2021, oral presentation.*

- Rabe M, Paganelli C, Schmitz H, Meschini G, Riboldi M, **Hofmaier J**, Dinkel J, Reiner M, Parodi K, Belka C, Landry G, Kurz C, Kamp F. Time-resolved estimated synthetic CTs based on orthogonal cine MRI for low-field MR-LINAC treatments. *AAPM 2021, oral presentation.*

- Nierer L, **Hofmaier J**, Belka C, Corradini S, Landry G, Reiner M. Use of treatment plan complexity analysis as a QA tool in MR-guided online adaptive radiotherapy. *MR in RT symposium 2021, oral presentation.*

- Walter F, **Hofmaier J**, Hadi I, Rottler M, Steffens R, Zollner B, Vettermann F, Belka C, Niyazi M. Einfluss von [68Ga]-DOTATATE-PET/CT auf die Zielvolumendefinition bei low-grade Meningeomen der Schädelbasis. *DEGRO 2020, poster.*

- Bodensohn R, Kaempfel A, Fleischmann DF, **Hofmaier J**, Hadi I, Garny S, Reiner M, Corradini S, Forbrig R, Thon N, Belka C, Niyazi M. Simultane stereotaktische Radiochirurgie von multiplen Metastasen mit "single isocenter dynamic conformal arc" Therapie. *DEGRO 2020, poster.*

- Bodensohn R, Kaempfel A, Fleischmann DF, **Hofmaier J**, Hadi I, Garny S, Reiner M, Corradini S, Forbrig R, Thon N, Belka C, Niyazi M. Stereotactic radiosurgery with single-isocenter dynamic arc therapy of multiple brain metastases. *ESTRO 2020, poster.*

- Kamp A, **Hofmaier J**, Söhn M, Alber M, Belka C, Landry G, Kamp F. Varianzbasierte Sensitivitätsanalyse von Monte-Carlo Dosisberechnungseinstellungen und Patientenpositionierung in der intensitätsmodulierten Strahlentherapie. *DGMP 2019, poster.*

- Meschini G, Kamp F, **Hofmaier J**, Reiner M, Sharp G, Paganetti H, Belka C, Parodi K, Baroni G, Riboldi M. A model for RBE-weighted dose estimation in irregularly moving targets. *PTCOG 2019, oral presentation.*

- von Münchow A, Straub K, Losert C, Shpani R, **Hofmaier J**, Freislederer P, Heinz C, Thieke C, Söhn M, Alber M, Floca R, Belka C, Parodi K, Reiner M, Kamp F. Random breathing states sampling in a 4D MC dose calculation framework to quantify interplay effects. *ESTRO 2018, oral presentation.*

- Niepel K, Kurz C, Kamp F, Hansen D, Rit S, Neppl S, **Hofmaier J**, Bondesson D, Thieke C, Dinkel J, Belka C, Parodi K, Landry G. Porcine-lung-phantom based evaluation of proton dose calculations on 4DCBCT. *ESTRO 2018, poster.*

- von Münchow A, Straub K, **Hofmaier J**, Freislederer P, Heinz C, Reiner M, Thieke C, Söhn M, Alber M, Floca R, Belka C, Parodi K, Kamp F. Monte Carlo framework for the evaluation of interplay effects between dose application and respiratory motion. *DGMP 2017, oral presentation.*

- Dinkel K, **Hofmaier J**, Kurz C, Reiner M, Parodi K, Belka C, Kamp F. Dose calculation based on Hounsfield Unit calibrated cone beam CT images. *DGMP 2017, poster.*

- von Münchow A, Straub K, **Hofmaier J**, Freislederer P, Reiner M, Thieke C, Söhn M, Alber M, Floca R, Belka C, Parodi K, Kamp F. Framework for the evaluation of interplay effects between respiratory motion and dose application. *ESTRO 2017, e-poster.*

- Bodensohn R, Söhn M, **Hofmaier J**, Ganswindt U, Schnell O. Belka C, Niyazi M. Neurokognitive Auswirkungen nach Radiotherapie von Patienten mit malignem Gliom unter Berücksichtigung der Hippocampus-Dosisbelastung. *DEGRO 2015, oral presentation.*

Bibliography

Adamson, J. and Q. Wu (2009). "Inferences About Prostate Intrafraction Motion From Pre- and Posttreatment Volumetric Imaging". In: *International Journal of Radiation Oncology Biology Physics* 75.1, pp. 260–267.

Agostinelli, S. et al. (2003). "GEANT4 - A simulation toolkit". In: *Nuclear Instruments and Methods in Physics Research, Section A: Accelerators, Spectrometers, Detectors and Associated Equipment* 506.3, pp. 250–303.

Ahnesjö, A. (1989). "Collapsed cone convolution of radiant energy for photon dose calculation in heterogeneous media". In: *Medical Physics* 16, pp. 577–592.

Amaldi, U. et al. (2010). "Accelerators for hadrontherapy: From Lawrence cyclotrons to linacs". In: *Nuclear Instruments and Methods in Physics Research, Section A: Accelerators, Spectrometers, Detectors and Associated Equipment* 620.2-3, pp. 563–577.

Bai, X. et al. (2019). "Robust optimization to reduce the impact of biological effect variation from physical uncertainties in intensity-modulated proton therapy". In: *Physics in Medicine and Biology* 64.2.

Barker, J. L. et al. (2004). "Quantification of volumetric and geometric changes occurring during fractionated radiotherapy for head-and-neck cancer using an integrated CT/linear accelerator system". In: *International Journal of Radiation Oncology Biology Physics* 59.4, pp. 960–970.

Baumann, M. et al. (2016). "Radiation oncology in the era of precision medicine". In: *Nature Reviews Cancer* 16.4, pp. 234–249.

Borras, J. M. et al. (2015). "The optimal utilization proportion of external beam radiotherapy in European countries: An ESTRO-HERO analysis". In: *Radiotherapy and Oncology* 116.1, pp. 38–44.

Bortfeld, T. (2006). "IMRT: A review and preview". In: *Physics in Medicine and Biology* 51.13, R363–R379.

Brock, K. K. et al. (2017). "Use of image registration and fusion algorithms and techniques in radiotherapy: Report of the AAPM Radiation Therapy Committee Task Group No. 132: Report". In: *Medical Physics* 44.7, e43–e76.

Carlson, D. J. et al. (2008). "Combined Use of Monte Carlo DNA Damage Simulations and Deterministic Repair Models to Examine Putative Mechanisms of Cell Killing". In: *Radiation Research* 169.4, pp. 447–459.

Chin, S. et al. (2020). "Magnetic resonance-guided radiation therapy: A review". In: *Journal of Medical Imaging and Radiation Oncology* 64.1, pp. 163–177.

Contreras, J. et al. (2017). "The world's first single-room proton therapy facility: Two-year experience". In: *Practical Radiation Oncology* 7.1, e71–e76.

Dedes, G. et al. (2019). "Experimental comparison of proton CT and dual energy x-ray CT for relative stopping power estimation in proton therapy". In: *Physics in Medicine and Biology* 64.16.

Edmund, J. M. and T. Nyholm (2017). "A review of substitute CT generation for MRI-only radiation therapy". In: *Radiation Oncology* 12.1.

Ferrari, A. et al. (2005). "FLUKA: A Multi-Particle Transport Code". In: *CERN-2005-10*, INFN/TC_05/11, SLAC–R–773.

Fippel, M. (1999). "Fast Monte Carlo dose calculation for photon beams based on the VMC electron algorithm." In: *Medical physics* 26.8, pp. 1466–1475.

Forsthoefel, M. K. et al. (2020). "Early Experience of the First Single-Room Gantry Mounted Active Scanning Proton Therapy System at an Integrated Cancer Center". In: *Frontiers in Oncology* 10, p. 861.

Frese, M. C. et al. (2012). "A mechanism-based approach to predict the relative biological effectiveness of protons and carbon ions in radiation therapy". In: *International Journal of Radiation Oncology Biology Physics* 83.1, pp. 442–450.

Hansen, D. C. et al. (2018). "ScatterNet: A convolutional neural network for cone-beam CT intensity correction". In: *Medical Physics* 45.11, pp. 4916–4926.

Hinterberger, F. (2008). *Physik der Teilchenbeschleuniger und Ionenoptik*. 2nd ed. Berlin Heidelberg: Springer-Verlag.

Hoffmann, A. et al. (2020). "MR-guided proton therapy: A review and a preview". In: *Radiation Oncology* 15.1.

Hofmaier, J. et al. (2021). "Variance-based sensitivity analysis for uncertainties in proton therapy: A framework to assess the effect of simultaneous uncertainties in range, positioning and RBE model predictions on RBE-weighted dose distributions". In: *Medical Physics* 48.2, pp. 805–818.

Hsiao, Y. and R. D. Stewart (2008). "Monte Carlo simulation of DNA damage induction by x-rays and selected radioisotopes". In: *Physics in Medicine and Biology* 53.1, pp. 233–244.

Hubbell, J. H. (1999). "Review of photon interaction cross section data in the medical and biological context". In: *Physics in Medicine and Biology* 44.1.

Jaffray, D. A. (2012). "Image-guided radiotherapy: From current concept to future perspectives". In: *Nature Reviews Clinical Oncology* 9.12, pp. 688–699.

Jaffray, D. A. et al. (2002). "Flat-panel cone-beam computed tomography for image-guided radiation therapy". In: *International Journal of Radiation Oncology Biology Physics* 53.5, pp. 1337–1349.

Jiang, Y. et al. (2019). "Scatter correction of cone-beam CT using a deep residual convolution neural network (DRCNN)". In: *Physics in Medicine and Biology* 64.14, p. 145003.

Kahn, F. M. and J. P. Gibbons (2014). *Khan's The Physics of Radiation Therapy*. 5th ed. Philadelphia: Wolters Kluwer.

Kamp, F., D. J. Carlson, and J. J. Wilkens (2017). "Rapid implementation of the repair-misrepair-fixation (RMF) model facilitating online adaption of radiosensitivity parameters in ion therapy". In: *Physics in Medicine and Biology* 62.13, N285–N296.

Karger, C. P. and P. Peschke (2018). "RBE and related modeling in carbon-ion therapy". In: *Physics in Medicine and Biology* 63.1, 01TR02.

Keall, P., P. Poulsen, and J. T. Booth (2019). "See, Think, and Act: Real-Time Adaptive Radiotherapy". In: *Seminars in Radiation Oncology* 29.3, pp. 228–235.

Krieger, H. (2012). *Grundlagen der Strahlungsphysik und des Strahlenschutzes*. 4th ed. Wiesbaden: Vieweg+Teubner.

— (2013). *Strahlungsquellen für Technik und Medizin*. 2nd ed. Wiesbaden: Springer Fachmedien.

Kurz, C. et al. (2019). "CBCT correction using a cycle-consistent generative adversarial network and unpaired training to enable photon and proton dose calculation". In: *Physics in Medicine and Biology* 64.22, p. 225004.

Landry, G. and C. ho Hua (2018). "Current state and future applications of radiological image guidance for particle therapy". In: *Medical Physics* 45.11, e1086–e1095.

Lühr, A. et al. (2018). ""Radiobiology of Proton Therapy": Results of an international expert workshop". In: *Radiotherapy and Oncology* 128.1, pp. 56–67.

Mackie, T. R. et al. (1988). "Generation of photon energy deposition kernels using the EGS Monte Carlo code". In: *Physics in Medicine and Biology* 33, pp. 1–20.

Maspero, M. et al. (2020). "Deep learning-based synthetic CT generation for paediatric brain MR-only photon and proton radiotherapy". In: *Radiotherapy and Oncology*.

McGowan, S. E., N. G. Burnet, and A. J. Lomax (2013). "Treatment planning optimisation in proton therapy". In: *British Journal of Radiology* 86.1021.

McMahon, S. J. (2019). "The linear quadratic model: Usage, interpretation and challenges". In: *Physics in Medicine and Biology* 64.1.

Mohan, R., C. Chui, and L. Lidofsky (1986). "Differential pencil beam dose computation model for photons". In: *Medical Physics* 13.1, pp. 64–73.

Mohan, R. and D. Grosshans (2017). "Proton therapy – Present and future". In: *Advanced Drug Delivery Reviews* 109, pp. 26–44.

Mohan, R. et al. (2017). "Radiobiological issues in proton therapy". In: *Acta Oncologica* 56.11, pp. 1367–1373.

Neppl, S. et al. (2019). "Evaluation of proton and photon dose distributions recalculated on 2D and 3D Unet-generated pseudoCTs from T1-weighted MR head scans". In: *Acta Oncologica* 58.10, pp. 1429–1434.

Newhauser, W. D. and R. Zhang (2015). "The physics of proton therapy". In: *Physics in Medicine and Biology* 60.8, R155–R209.

Njeh, C. F. (2008). "Tumor delineation: The weakest link in the search for accuracy in radiotherapy". In: *Journal of Medical Physics* 33.4, pp. 136–140.

Oldham, M. et al. (2005). "Cone-beam-CT guided radiation therapy: A model for on-line application". In: *Radiotherapy and Oncology* 75.3, 271.E1–271.E8.

Paganetti, H. (2012a). *Proton Therapy Physics*. 1st ed. Boca Raton: CRC Press, Taylor & Francis Group.

Paganetti, H. (2012b). "Range uncertainties in proton therapy and the role of Monte Carlo simulations". In: *Physics in Medicine and Biology* 57.11, R99–R117.

— (2014). "Relative biological effectiveness (RBE) values for proton beam therapy. Variations as a function of biological endpoint, dose, and linear energy transfer". In: *Physics in Medicine and Biology* 59.22, R419–R472.

— (2018). "Proton relative biological effectiveness-uncertainties and opportunities". In: *International Journal of Particle Therapy* 5.1, pp. 2–14.

Paganetti, H. et al. (2019). "Report of the AAPM TG-256 on the relative biological effectiveness of proton beams in radiation therapy". In: *Medical Physics* 46.3, e53–e78.

Podgorsak, E. B. et al. (2005). *Radiation Oncology Physics: A Handbook for Teachers and Students*. Ed. by E. B. Podgorsak. 1st ed. Vienna: IAEA.

Rossi, H. H. and M. Zaider (1996). *Microdosimetry and its applications*. Heidelberg: Springer-Verlag.

Rusanov, B. et al. (2021). "A convolutional neural network for estimating cone-beam CT intensity deviations from virtual CT projections". In: *Physics in Medicine and Biology* 66.21.

Saltelli, A. (2002). "Making best use of model evaluations to compute sensitivity indices". In: *Computer Physics Communications* 145.2, pp. 280–297.

Saltelli, A. et al. (2004). *Sensitivity Analysis in Practice: A Guide to Assessing Scientific Models*. Chichester: John Wiley & Sons, Ltd.

Saltelli, A. et al. (2008). *Global Sensitivity Analysis. The Primer*. Chichester: John Wiley & Sons, Ltd, pp. 1–292.

Saltelli, A. et al. (2010). "Variance based sensitivity analysis of model output. Design and estimator for the total sensitivity index". In: *Computer Physics Communications* 181.2, pp. 259–270.

Schlegel, W., C. P. Karger, and O. Jäkel (2018). *Medizinische Physik*. 1st ed. Berlin: Springer Spektrum.

Semenenko, V. A. and R. D. Stewart (2004). "A Fast Monte Carlo Algorithm to Simulate the Spectrum of DNA Damages Formed by Ionizing Radiation". In: *Radiation Research* 161.4, pp. 451–457.

— (2006). "Fast Monte Carlo simulation of DNA damage formed by electrons and light ions". In: *Physics in Medicine and Biology* 51.7, pp. 1693–1706.

Shusharina, N. et al. (2019). "Impact of aeration change and beam arrangement on the robustness of proton plans". In: *Journal of Applied Clinical Medical Physics* 20.3, pp. 14–21.

Sobol, I. M. (1967). "On the distribution of points in a cube and the approximate evaluation of integrals". In: *USSR Computational Mathematics and Mathematical Physics* 7.4, pp. 86–112.

— (2001). "Global sensitivity indices for nonlinear mathematical models and their Monte Carlo estimates". In: *Mathematics and Computers in Simulation* 55, pp. 271–280.

Sobol, I. M. et al. (1992). "Quasi-random sequence generators". In: *Ipm zak* 30.

Sonke, J. J., M. Aznar, and C. Rasch (2019). "Adaptive Radiotherapy for Anatomical Changes". In: *Seminars in Radiation Oncology* 29.3, pp. 245–257.

Stewart, R. D. et al. (2011). "Effects of radiation quality and oxygen on clustered DNA lesionsand cell death". In: *Radiation Research* 176.5, pp. 587–602.

Stroom, J. C. et al. (1999). "Inclusion of geometrical uncertainties in radiotherapy treatment planning by means of coverage probability". In: *International Journal of Radiation Oncology Biology Physics* 43.4, pp. 905–919.

Sung, H. et al. (2021). "Global Cancer Statistics 2020: GLOBOCAN Estimates of Incidence and Mortality Worldwide for 36 Cancers in 185 Countries". In: *CA: A Cancer Journal for Clinicians* 71.3, pp. 209–249.

Taylor, J. R. (1997). *An Introduction to Error Analysis*. 2nd ed. Sausalito, California: University Science Books.

Teoh, M. et al. (2011). "Volumetric modulated arc therapy: A review of current literature and clinical use in practice". In: *British Journal of Radiology* 84.1007, pp. 967–996.

Tobias, C. A. et al. (1958). "Pituitary Irradiation with High-Energy Proton Beams A Preliminary Report". In: *Cancer Research* 18.2, pp. 121–134.

Tobler, M., G. Watson, and D. D. Leavitt (2002). "The application of dynamic field shaping and dynamic dose rate control in conformal rotational treatment of the prostate". In: *Medical Dosimetry* 27.4, pp. 251–254.

Unkelbach, J. et al. (2016). "Reoptimization of Intensity Modulated Proton Therapy Plans Based on Linear Energy Transfer". In: *International Journal of Radiation Oncology Biology Physics* 96.5, pp. 1097–1106.

Unkelbach, J. et al. (2018). "Robust radiotherapy planning". In: *Physics in Medicine and Biology* 63.22, 22TR02.

Van Herk, M. (2004). "Errors and Margins in Radiotherapy". In: *Seminars in Radiation Oncology* 14.1, pp. 52–64.

Van Herk, M. (2007). "Different Styles of Image-Guided Radiotherapy". In: *Seminars in Radiation Oncology* 17.4, pp. 258–267.

Van Herk, M. et al. (2000). "The probability of correct target dosage: Dose-population histograms for deriving treatment margins in radiotherapy". In: *International Journal of Radiation Oncology Biology Physics* 47.4, pp. 1121–1135.

Verhaegen, F. and J. Seuntjens (2003). "Monte Carlo modelling of external radiotherapy photon beams". In: *Physics in Medicine and Biology* 48.21, R107–R164.

Vinod, S. K. et al. (2016). "Uncertainties in volume delineation in radiation oncology: A systematic review and recommendations for future studies". In: *Radiotherapy and Oncology* 121.2, pp. 169–179.

Wannenmacher, M., J. Debus, and D. Schulz-Ertner (2013). *Strahlentherapie*. 2nd ed. Heidelberg: SpringerMedizin.

Wedenberg, M., B. K. Lind, and B. Hårdemark (2013). "A model for the relative biological effectiveness of protons: The tissue specific parameter α/β of photons is a predictor for the sensitivity to LET changes". In: *Acta Oncologica* 52.3, pp. 580–588.

Weiss, E. and C. F. Hess (2003). "The impact of gross tumor volume (GTV) and clinical target volume (CTV) definition on the total accuracy in radiotherapy: Theoretical aspects and practical experiences". In: *Strahlentherapie und Onkologie* 179.1, pp. 21–30.

Wilkens, J. J. and U. Oelfke (2004). "A phenomenological model for the relative biological effectiveness in therapeutic proton beams". In: *Physics in Medicine and Biology* 49.13, pp. 2811–2825.

— (2006). "Fast multifield optimization of the biological effect in ion therapy". In: *Physics in Medicine and Biology* 51.12, pp. 3127–3140.

Wohlfahrt, P. et al. (2017). "Dual-energy CT based proton range prediction in head and pelvic tumor patients". In: *Radiotherapy and Oncology* 125.3, pp. 526–533.

Zaider, M. and H. H. Rossi (1980). "The Synergistic Effects of Different Radiations". In: *Radiation Research* 83.3, pp. 732–739.